Summer 8-2018

Fault-Adjacent Damage at the Base of the Seismogenic Zone and Seismic Anisotropy of Fold Structures

Won Joon Song
University of Maine, wonjoon.song@maine.edu

FAULT-ADJACENT DAMAGE AT THE BASE OF THE SEISMOGENIC ZONE AND SEISMIC ANISOTROPY OF FOLD STRUCTURES

By

Won Joon Song

B.S. Korea University South Korea, 2004

M.S. Korea University South Korea, 2008

A DISSERTATION

Submitted in Partial Fulfillment of the

Requirements for the Degree of

Doctor of Philosophy

(in Earth and Climate Sciences)

The Graduate School

The University of Maine

August 2018

Advisory Committee:

Scott E. Johnson, Professor and Director of Earth and Climate Sciences, Co-Advisor

Christopher C. Gerbi, Associate Professor of Earth and Climate Sciences, Co-Advisor

Peter O. Koons, Professor of Earth and Climate Sciences

Senthil S. Vel, Arthur O. Willey Professor of Mechanical Engineering

David Okaya, Associate Professor (Research) of Earth Sciences, University of Southern California

FAULT-ADJACENT DAMAGE AT THE BASE OF THE SEISMOGENIC ZONE AND SEISMIC ANISOTROPY OF FOLD STRUCTURES

By Won Joon Song

Dissertation Advisors: Dr. Scott E. Johnson and Dr. Christopher C. Gerbi

An Abstract of the Dissertation Presented
in Partial Fulfillment of the Requirements for the
Degree of Doctor of Philosophy
(in Earth and Climate Sciences)

August 2018

While earthquakes represent a major hazard to life and property, there are a number of open questions about how earthquake faults operate at depth, and how the energy released by earthquakes travels as elastic waves through Earth's complexly deformed crustal rocks. The aims of my dissertation are to explore (a) the extent of co-seismic damage in an ancient earthquake fault exhumed from great depths, (b) the deformation processes and mechanics of the fault at depth during earthquake cycles, and (c) the role of different rock structures in determining the velocities of seismic waves.

When tectonic plates collide, deformation tends to localize into narrow zones: frictional faults in the upper crust and high-temperature viscous shear zones in the lower crust. The transition in material behavior from the upper to lower crust is known as the frictional-to-viscous transition (FVT; ~10–20 km deep). During earthquake cycles, the FVT experiences transient brittle deformation followed by long-term viscous processes. Owing to this complex behavior over the earthquake cycle, the FVT is the most important horizon for understanding earthquake mechanics. Rareness of exposures of ancient earthquake faults at FVT depths has hindered studying of their brittle co-seismic damage structures and rheology of their deep portions during earthquake cycles. From the Sandhill Corner shear zone, a strand of the Norumbega fault system (an ancient seismogenic strike-slip fault at the FVT), I analyze fluid inclusion abundance in quartz as a proxy for transient co-seismic damage using secondary electron image and optical observation, and collect quantitative data of quartz across the shear zone such as grain-size, grain-

shape, crystallographic orientation, misorientation, and fabric intensity through electron backscatter diffraction. The results indicate that brittle co-seismic damage occurs up to at least ~90 m in width at the FVT, and the inner shear zone (~40 m wide) experienced cycles of co-seismic microfracture-assisted grain-size reduction followed by post-seismic viscous deformation dominated by grain-size-sensitive processes, whereas the outer shear zone was deformed dominantly by grain-size-insensitive processes during earthquake cycles. My findings have important implications for the strength, or mechanics, of the fault/shear zone system, and may help determine 3-D volume of brittle damage zone. Measuring the extent of damage zone is critical for estimating the potential energy that an earthquake releases because the co-seismic damage zone acts as a dissipative energy sink by creating fracture surface areas.

Earthquakes not only represent hazards but radiate energy as seismic waves. Since the direction-dependent nature of wave propagation velocities (called "seismic anisotropy") changes in response to rock flow due to preferred orientation of elastically anisotropic minerals, the seismic anisotropy has been used to investigate Earth's interior structure and deformation processes in tectonically active regions. However, this is a challenge for waves passing through the crust because their anisotropies are profoundly modified by macroscale folds, which are very common structures in ancient and current orogenic belts and shear zones. To evaluate the modification of seismic anisotropy by the deformation structures, I develop a new mathematical methodology for calculating bulk elastic tensors and seismic anisotropy of macroscale folds, assuming the seismic waves are much larger than the fold heterogeneity. The results show that the velocities of seismic waves propagating through macroscale folds in three dimensions are systematically related to fold shape and orientation. Because fold orientations are related to flow directions, it is now possible for real seismic observables to provide information on the directions of flow for actively deforming rocks at depth.

DEDICATION

In memory of my beloved grandmother
Jung-ok Ko (1928-2011)
the strongest, most beautiful woman I know

ACKNOWLEDGEMENTS

I am grateful to the National Science Foundation for funding the majority of this work, through research grants to my advisor Scott Johnson, and to the University of Maine Graduate Student Government for funding some of the analysis. Travel costs to present at conferences were largely covered through several University of Maine Graduate Student Travel Grants and the Geological Society of America travel grant. Additional supports were provided by the Chase Distinguished Research Fellowship and the Correll Doctoral Fellowship. I was also supported by a University of Maine Teaching Assistantship.

Many people have made this research possible and have shaped my graduate experience at the University of Maine. I am hugely indebted to the members of my advisory committee (Scott Johnson, Christopher Gerbi, Peter Koons, Senthil Vel, and David Okaya) for your countless hours of guidance and for the huge role each has played in my constant learning and future. I would like to express my special thanks to my advisor, Scott Johnson, for his guidance, motivation, and patience through this entire process. Scott opened my eyes to the outstanding problems of earthquake fault, has supported to pursue my growing interest in those problems, and has involved me in world-class research. He has helped me to build my confidence and independence, keeping saying you can change the world. His careful readings and editing of my manuscripts have also made me a much better scientific writer. Thank you, Scott, for your mentorship and friendship over these past years. I could not have asked for a better advisor. I would also like to thank my co-advisor, Chris Gerbi, for his ability to motivate and inspire me with a lot of very pertinent questions. You have taught me the valuable lessons that 'better is the enemy of good enough'. Thank you, Peter, for keeping my research relevant to the larger world rich with unknown. You are my best role model for a scientist, mentor, and teacher. Thank you Senthil and David for your expertise and continued input over the years that have helped to keep me and my ideas grounded in the realistic and practical.

Special thanks to Edward Grew, Martin Yates, and Alicia (Cici) Cruz-Uribe for the discussions, the research advice, and all the unwavering support over the years. Thank you to Daniel Belknap for helping me to learn strategies for communicating my research to a general audience. Thank you to Dan Lux for all your help, feedback, support, and encouragement with ERS 101 teaching. Dave West (Middlebury College) is thanked for enthusiastically introducing me to all the good Sandhill Corner shear zone outcrops and helpful discussions at conferences. Other members of the School of Earth and Climate Sciences who deserve thanks are Diane Perro and Linda Cappuccio for helping me sort out numerous administrative details. The School of Earth and Climate Sciences have fostered the collaborative research and young scientist community. My scientific thinking has developed through a lot of communication with fellow UMaine students and alumni. In no particular order I would like to acknowledge Erik Anderson, Steven Bernsen, Anne Boucher, Alden Cook, Maura Foley, Ben Frieman, Brett Gerard, Laura Hartman, James Hodge, Lynn Kaluzienski, Stephanie Mills, Felice Naus-Thijssen, Nancy Price, Nicholas Richmond, Charles Rodda, Sam Roy, Deborah Shulman, Bora Song, Steven Spreitzer, Jesse Walters, Lauren Wheeler for their suggestions and feedback.

Finally, but in many ways most importantly, I want to express my gratitude to my family, mentors, and friends who always support and believe in me. Without the support and love of my family, mentors, and friends back in South Korea, I would not be where I am today. Being so far away from you was hard at times, missing many holidays, birthdays, and special occasions, and I am really looking forward spending more time with you again once we return to Korea. Thank you, thank you, thank you to Church family for your prayers and love. I heartily thank to and love my parents in heaven, who gave me a world full of possibilities. Most of all I would like to thank my wife Bora for providing emotional support throughout the course of this thesis and for always being there for me!

TABLE OF CONTENTS

LIST OF FIGURES

CHAPTER 1

INTRODUCTION

Fault zones in plate boundaries accommodate displacements within the lithosphere and act as a plumbing system for fluid flow as well as heat and mass transfer, and also generate natural hazards such as earthquakes and tsunamis that can destroy human life and infrastructure. To mitigate the impacts of such devastating natural disasters, we need to better understand how fault structures and deformation processes evolve at plate boundaries from Earth's surface to deep interior, so that we can predict the tectonic processes more accurately and precisely. This is a major challenge and ultimate goal that geoscientists have and can be achieved by multidisciplinary studies of fault behavior and rock rheology (mechanical properties of rocks) during earthquake cycles throughout the lithosphere in different tectonic settings, exploring how deformation processes operating at different lithospheric depths are linked vertically (Huntington and Klepeis, 2018). The studies include, as in this dissertation, quantitative measures of the rock record of fault behaviors in ancient plate margins exhumed from various depths, which can be integrated with geological and geophysical observations in modern plate margins for better understanding of fault mechanics across the lithosphere.

When an earthquake occurs, the stored potential energy, such as elastic strain energy and gravitational energy, is partitioned into radiated energy, frictional heat energy, and fracture energy (Kanamori and Rivera, 2006). While the radiated energy by elastic waves is a small fraction (5% to 20%) of the total energy budget, the other 80–95% energy is consumed by inelastic physical and chemical processes in the fault core and the surrounding damage zone (Shipton et al., 2006). The frictional heat energy is dissipated by sliding on the rupture surface, and the fracture energy refers to all other dissipative energy sinks active on the rupture surface and within the 3-D fault volume, which include plastic yielding at rupture tips, off-fault cracking, and various thermal processes (e.g., fluid pressurization and melting) (Kanamori and Rivera, 2006; Shipton et al., 2006). The frictional heat, often occupying a large component of the total energy, does not directly affect earthquake rupture dynamics such as rupture speed,

whereas the fracture energy, more precisely the relative magnitude of the radiated energy to the fracture energy, plays a significant role (Husseini and Randall, 1976; Venkataraman and Kanamori, 2004).

Off-fault damage is caused by dynamic stress changes near the propagating rupture front (Poliakov et al., 2002; Andrews, 2005; Rice et al., 2005). In addition to its role as a dissipative energy sink by making new surfaces of fractures, the off-fault damage zone created by previous seismic slip events can have effects on state of stress, near-fault ground motion, earthquake rupture, and crustal fluid flow. Damage zones may rotate the stress field surrounding faults, allowing high pore fluid pressure and thus weakening of unfavorably oriented faults (Faulkner et al., 2006). Inside damage zones, earthquakes produce reflected waves and head waves, which can amplify ground motion near the fault (Spudich and Olsen, 2001), but also cause slip pulses and oscillations of rupture speed (e.g., Huang et al., 2014) possibly promoting supershear earthquakes (e.g., Huang et al., 2016; Perrin et al., 2016). Damage zones also affect crustal fluid flow by change in permeability, which in turn contributes to the fault strength and the triggering of aftershocks by change in pore fluid pressure (Miller et al., 2004). Therefore, it is important to determine how deep and wide the damage zone extends.

Studies of exhumed faults from the upper crust report that the width of the damage zones around continental strike-slip faults can be hundreds of meters depending on fault displacement (e.g., Mitchell and Faulkner, 2009; Faulkner et al., 2011; Savage and Brodsky, 2011). Seismological studies of low-velocity, fault zone-guided waves in active strike-slip faults show that damage zones extend down to only 3–5 km (e.g., Ben-Zion et al., 2003; Lewis and Ben-Zion, 2010) or more than 7 km (e.g., Li and Malin, 2008; Cochran et al., 2009; Ellsworth and Malin, 2011; Li et al., 2014). However, there have been no geological studies in deeply exhumed strike-slip faults/shear zones to assess the width of off-fault damage. In Chapter 2, I provide a new method to estimate how wide off-fault damage is distributed by measuring fluid inclusion abundance in quartz aggregates across the pseudotachylyte-bearing Sandhill Corner shear zone (a strand of the Paleozoic Norumbega fault system, Maine, USA) exhumed from the base of the seismogenic zone, where quartz experiences brittle co-seismic damage and post-/inter-seismic viscous deformation.

The base of the seismogenic zone is also called the frictional-to-viscous transition (FVT; ~10–20 km deep) since it deforms in both brittle and viscous fashions by changes in stress and strain rate during an earthquake cycle. The FVT is the strongest part of the continental crust and thus controls the strength of tectonic plates and the mechanical decoupling between the upper and lower crust (Brace and Kohlstedt, 1980; Kohlstedt et al., 1995; Handy et al., 2007). Therefore, a more complete study of deformation processes at the FVT during seismic cycles is required to understand strain localization and rheological changes at plate boundaries. Chapter 3 reports quantitative microfabrics of quartz from the shear zone core to the host rocks in the same field area as Chapter 2 using electron backscatter diffraction, and investigates how transient co-seismic damage affects localization mechanism in quartz.

Seismic waves radiated from an earthquake can be utilized to observe in situ tectonic deformation and convective flow in the deep crust and mantle through seismic anisotropy, or the dependence of seismic velocity on the direction of wave propagation and polarization. However, fold structures can modify seismic properties of the deformed rocks by rotating rock fabrics such as foliation and lineation (Okaya et al., 2018). Since folds are very common tectonic structures found in ancient and current orogenic belts and shear zones, they should be considered when interpreting seismic anisotropy as a proxy for tectonic deformation or kinematics. In Chapter 4, I develop a new mathematical method to calculate bulk elastic tensors of idealized cylindrical folds, assuming the incident seismic waves are much larger than the fold heterogeneity. This allows me to investigate how the morphological change of fold affects the wave velocity with varying propagation direction and the magnitude and symmetry of seismic anisotropy.

CHAPTER 2

QUARTZ FLUID INCLUSION ABUNDANCE AND OFF-FAULT DAMAGE IN A DEEPLY EXHUMED SEISMOGENIC FAULT

2.1. Chapter Abstract

Off-fault damage zones comprise highly fractured rocks surrounding the dynamic slip surface of an earthquake fault. These damage zones modify fault-zone rheology and rupture dynamics by changing the bulk elastic properties and modulating fluid flow. Damage zones in the brittle upper crust, reaching widths >100 m, are commonly characterized by measuring fracture density, but there have been no geological studies in deeply exhumed strike-slip faults to assess the extent of off-fault damage at depth. This is primarily because co-seismic fractures at depth are generally healed and, in some minerals like quartz, eliminated by neo- and recrystallization during post-seismic deformation. In this study, we report on a novel study of fluid inclusion abundance in quartz deformed at 400–500 ℃ from an ancient seismogenic strike-slip fault/shear zone to evaluate whether it can be a proxy for the width of a damage zone even after experiencing post- and inter-seismic viscous deformation. Based on secondary electron image analysis and optical observation, the shear zone has a low-high-low trend of fluid inclusion abundance from the shear zone core toward the host rock. Taking into account the addition of fluid inclusions by co-seismic deformation and their removal by recrystallization, off-fault damage occurs up to at least ~90 m from the shear zone core. These findings indicate that extensive co-seismic damage zones may extend from Earth's surface to the base of the seismogenic zone, with important implications for fault strength, rupture dynamics, and transient fluid flow.

2.2. Chapter Introduction

Large displacement strike-slip faults display impressive off-fault damage zones with fracture density increasing toward the fault core, and pulverization of specific rock types (e.g., Chester et al., 1993; Ben-Zion and Sammis, 2003; Rempe et al., 2013). Fractured damage zones affect: (a) local stress distribution (Faulkner et al., 2006); (b) near-fault ground motion (Spudich and Olsen, 2001); (c) rupture

dynamics (e.g., Thomas et al., 2017) possibly promoting supershear earthquake (e.g., Huang et al., 2016); and (d) crustal fluid flow by transient changes in permeability, which in turn contributes to the fault strength and the triggering of aftershocks by changes in pore fluid pressure (Miller et al., 2004). In addition, determining 3-D volume of damage zone (i.e., the depth and width) is important for estimating the potential energy that an earthquake releases because the off-fault damage zone along with the fault core acts as significant energy sinks dissipating fracture and thermal energy, which occupy 80–95% of the total energy budget (e.g., Poliakov et al., 2002; Andrews, 2005; Rice et al., 2005; Kanamori and Rivera, 2006; Shipton et al., 2006). Studies of exhumed faults from the upper 10 km of the crust report that the damage zones can be hundreds of meters wide (e.g., Mitchell and Faulkner, 2009; Faulkner et al., 2011; Savage and Brodsky, 2011). Although seismological studies of low-velocity, fault zone-guided waves show possible depth limits of damage zones (e.g., Ben-Zion et al., 2003; Li and Malin, 2008; Cochran et al., 2009; Lewis and Ben-Zion, 2010; Ellsworth and Malin, 2011; Li et al., 2014), there have been no geological studies in deeply exhumed strike-slip faults with large displacement to assess the extent of off-fault damage. Characterizing the extent of brittle damage in rocks exhumed from the deeper reaches of the seismogenic zone, equivalent to frictional-to-viscous transition depths (e.g., Handy et al., 2007), is complicated owing to the fact that evidence of co-seismic damage (e.g., healed intragranular microcracks) in minerals like quartz is typically erased or altered by post-seismic viscous deformation (e.g., dynamic recrystallization). Minerals such as feldspar that undergo brittle deformation at these conditions are also altered by processes such as granular flow of fragments during the inter-seismic phase, making it difficult to parse out the co-seismic contribution to the microstructure.

Several studies attempted to find quartz microfabrics diagnostic of transient co-seismic damage under conditions near the base of the seismogenic zone (10–20 km), where quartz deforms viscously during inter-seismic periods. Novel experiments of non-steady state behavior in quartz to simulate the co- and post-seismic deformation in the middle crust (Trepmann et al., 2007) and natural rock studies compared to it (e.g., Trepmann et al., 2017) provided narrow zones of fine recrystallized grains cutting through parent quartz grains, large misorientation angle between the parent and recrystallized grains,

and/or random crystallographic orientation of the recrystallized grains as possible evidence for transient co-seismic damage owing to neocrystallization (nucleation and growth) and ongoing recrystallization of fractured quartz. However, given that such evidence could also result from shear band formation and grain size-sensitive creep (e.g., combination of dynamic recrystallization and grain boundary sliding; Halfpenny et al., 2012), the recrystallized quartz that experienced co-seismic damage is difficult to distinguish from quartz deformed solely be viscous processes at non-steady state conditions. In addition, if the quartz is fully recrystallized during post- and inter-seismic periods or over multiple earthquake cycles, the evidence involving parent grains is no longer applicable to identifying transient brittle deformation.

Microcracks generated in quartz by co-seismic rupture near the base of the seismogenic zone are expected to heal rapidly (Brantley et al., 1990), but are typically decorated with fluid inclusions (e.g., Anders et al., 2014). If these fluid inclusion planes were preserved, then microfracture densities could be measured as is done in near-surface faults (e.g., Mitchell and Faulkner, 2009), providing a measure of damage-zone width. However, quartz at these depths undergoes viscous deformation by processes such as dislocation creep, which disrupts the fluid inclusion planes. During recrystallization, trapped fluid inclusions can be dragged by migrating subgrain and grain boundaries, disrupting their planar structure (Kerrich, 1976; Drury and Urai, 1990; Schmatz and Urai, 2011). However, unless the fluid inclusions are destroyed, number and/or volume fraction of fluid inclusions may be related to the abundance of transient fractures and fracture events despite destruction of the fluid inclusion planes by viscous recovery and recrystallization processes. To evaluate whether fluid inclusion concentration can provide clear evidence for brittle co-seismic deformation of quartz at depth, we focus on fluid inclusion abundance in monomineralic quartz aggregates from a deeply exhumed seismogenic strike-slip fault zone (Sandhill Corner shear zone in the Norumbega fault system, Maine, USA; Johnson et al., 2009; Price et al., 2012, 2016). For clarity, this study considers only distribution and abundance of fluid inclusions; their compositions and closure temperatures will be analyzed separately. Here we present the number density (count per unit area) and volume fraction of fluid inclusion measured in quartz aggregates by secondary

electron image analysis (Schmatz and Urai, 2011) and optical observation as proxy for evaluating the width of co-seismic damage adjacent to the Sandhill Corner shear zone where brittle and viscous deformation alternated during seismic cycles.

2.3. Sandhill Corner Shear Zone near the Base of the Seismogenic Zone

The Norumbega fault system is a Paleozoic, subvertical, crustal-scale strike-slip fault system in the northeastern Appalachians (Fig. 2.1; Ludman and West, 1999) with estimated right-lateral slip of 25–300 km over a period of ~100 million years (e.g., Hubbard, 1999; West, 1999). Different erosion levels along the Norumbega expose rocks of upper amphibolite facies in the southwest to sub-greenschist facies in the northeast (Ludman and West, 1999). The Sandhill Corner shear zone (SCSZ; ~230 m wide in the study area) located in the central part of the Norumbega fault system contains mutually overprinting pseudotachylyte and mylonite (Price et al., 2012), indicating alternating brittle and viscous deformation during seismic cycles. The shear zone core occurs at the contact between quartzo-feldspathic (QF) and schist units (Figs. 2.1 and 2.2a; Price et al., 2016).

The quartz domains we analyze are deformed or folded quartz veins and ribbons from the QF rocks (Fig. 2.2a) and embedded in mica-rich matrix. All domains are thinner than 2 mm except one sample (NFS2) with a 4.5 cm-thick vein (Fig. 2.3). In the SCSZ, quartz recrystallization is dominantly by subgrain rotation with subsidiary grain boundary migration (Price et al., 2016). From the host rock toward the core, the degrees of mylonitization and recrystallization increase, and the average grain size of quartz decreases (Figs. 2.2b and 2.2c; see Chapter 3). The mylonitic deformation that accompanied co-seismic rupture occurred at temperatures of 400–500 ℃, overprinting previous higher-temperature microstructures preserved in the host rocks outside the shear zone (Price et al., 2016). The particularly thick quartz vein in sample NFS2 preserves both unaltered and recrystallized fluid inclusion planes (Fig. 2.2d). Fluid inclusions are rare in the unrecrystallized parent vein outside of fluid-inclusion-decorated microcracks, but are abundant where the vein has recrystallized (Fig. 2.2d).

Figure 2.1. Geologic setting of Sandhill Corner shear zone.

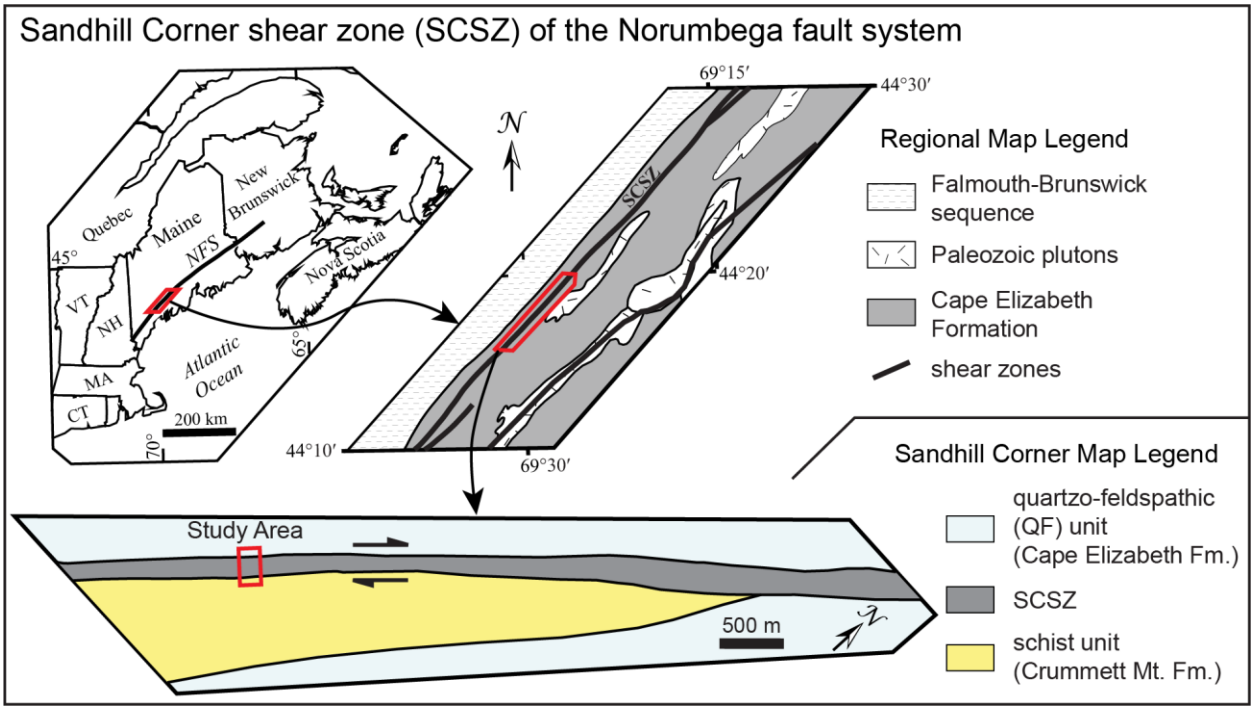

Figure 2.2. Sample locations and quartz microstructures. (a) Sample locations of current study and previous studies (Price et al., 2012, 2016). The samples used in the current study are labeled next to each location (white circle) (b) Area percentage of clast and pseudotachylyte (PST) and average (root-mean-square) grain size of quartz domains with respect to distance from the shear zone core. The modal percentage of clast is calculated except quartz domains. The modal clast and quartz grain size generally decrease toward the core. Note much higher occurrence of PST in the QF unit than the schist. The clast and PST data include the previous studies. For details of the grain size data, see Chapter 3. The boundaries and core of the shear zone are marked by dashed lines, connected to (a). (c) Quartz photomicrographs (cross-polarized) showing an increase in recrystallization and a decrease in grain size toward the core. (d) Quartz photomicrographs of sample NSF2 displaying correlation of fluid inclusion (FI) abundance with recrystallized (rxd) grains. The parent and recrystallized (rxd) quartz has little and abundant fluid inclusions, respectively. Note a string of recrystallized grains along a fluid inclusion plane (FIP) inside the parent grain. PPL, plane-polarized light; XPL, cross-polarized light.

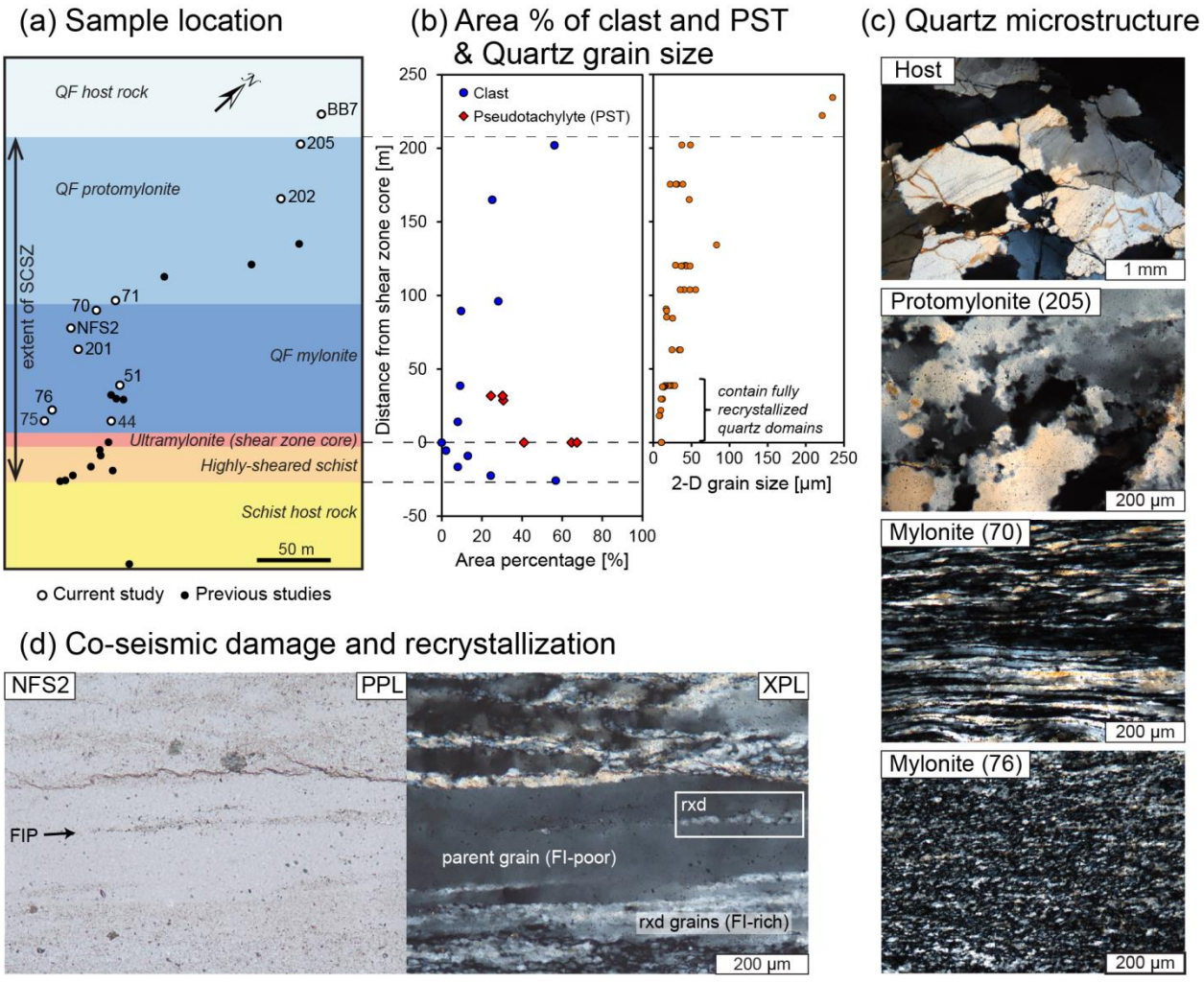

Figure 2.3. Thickness of quartz domains (veins or ribbons) analyzed in the current study. Various quartz domains were selected within a sample where available, showing variable degrees of recrystallization. Sample numbers are also displayed in the graph. The thickness is calculated by dividing the area of a quartz domain by the length of a median line. A logarithmic scale is used in the thickness axis.

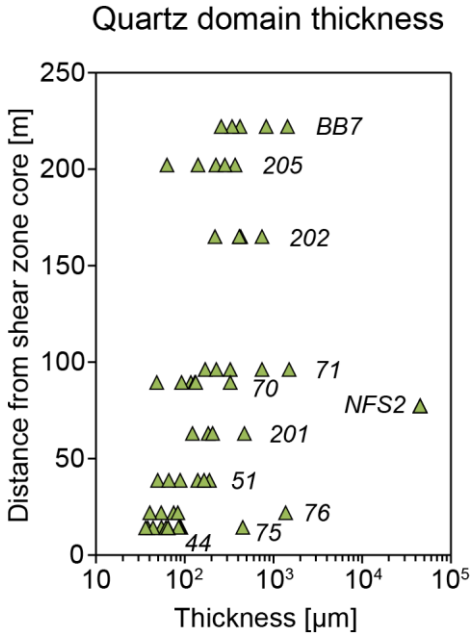

2.4. Methods

Samples were cut perpendicular to local foliations and parallel to local lineations, which are sub-parallel to the strike of the shear zone core. Doubly polished thin sections of 30–35 μm thickness were prepared to observe the microstructure and fluid inclusions in polarized light microscopy (mechanically polished with a 0.3 um alumina suspension and chemically in a 0.02 um colloidal silica suspension for several minutes). The number density and volume fraction of fluid inclusions were estimated from 2-D pores on carbon-coated polished surfaces of the thin sections using semi-automated analysis of secondary electron images (×4000 magnification) using a scanning electron microscope (SEM-SE images) similar to the techniques described in Schmatz and Urai (2011). The images were manually modified in *ImageJ* (https://imagej.nih.gov/ij/) during post-processing to eliminate uneven brightness (Fig. 2.4). Schmatz and Urai (2011) demonstrated that hand-polishing can provide information on real 2-D porosity within standard errors in comparison with measurements on broad ion beam-polished surfaces. I also optically

measured the number of fluid inclusions in the same analysis areas by manually counting them in a single focal plane to compare with the SEM-SE image analysis (Fig. 2.5). Five or six quartz domains including the lowest and highest degree of recrystallization in each thin section were taken for analysis. Since fluid inclusions are mostly located near and along grain boundaries owing to dynamic recrystallization, I measured enough number of whole grains (more than ten) to prevent biased results and determine representative fluid inclusion abundance for each domain (Fig. 2.6). Exceptions were made for recrystallized domains, parent grains, and quartz ribbons of the host rock with one large parent grain, in which only parts of grain boundaries were covered. All the analyses were carried out away from the phase boundaries between quartz domains and the mica-rich matrix due to substantial polishing defects at these boundaries. I note that only areas with fluid inclusions related to recrystallization were analyzed; I avoided late healed but unrecrystallized cracks at a high angle to local foliation, which presumably formed at shallow depths during exhumation.

Figure 2.4. Methodology for fluid inclusion abundance using secondary electron (SE) images. (a) Take a stitched SE image consisting of multiple high-resolution images (×4000 magnification) to cover enough number of grains. Using *ImageJ*, (b) set a threshold range to select pores, or fluid inclusions (darker than quartz in the SE images) and (c) modify manually the selected pores by comparing to the original SE images. From the processed images, (d) measure the number and area of fluid inclusions. The number density (count divided by background area), area fraction, and size of fluid inclusions are calculated from the measured results. The volume fraction and its error are estimated based on the area fraction, the count, and the mean and standard deviation of the pore areas (Underwood, 1970).

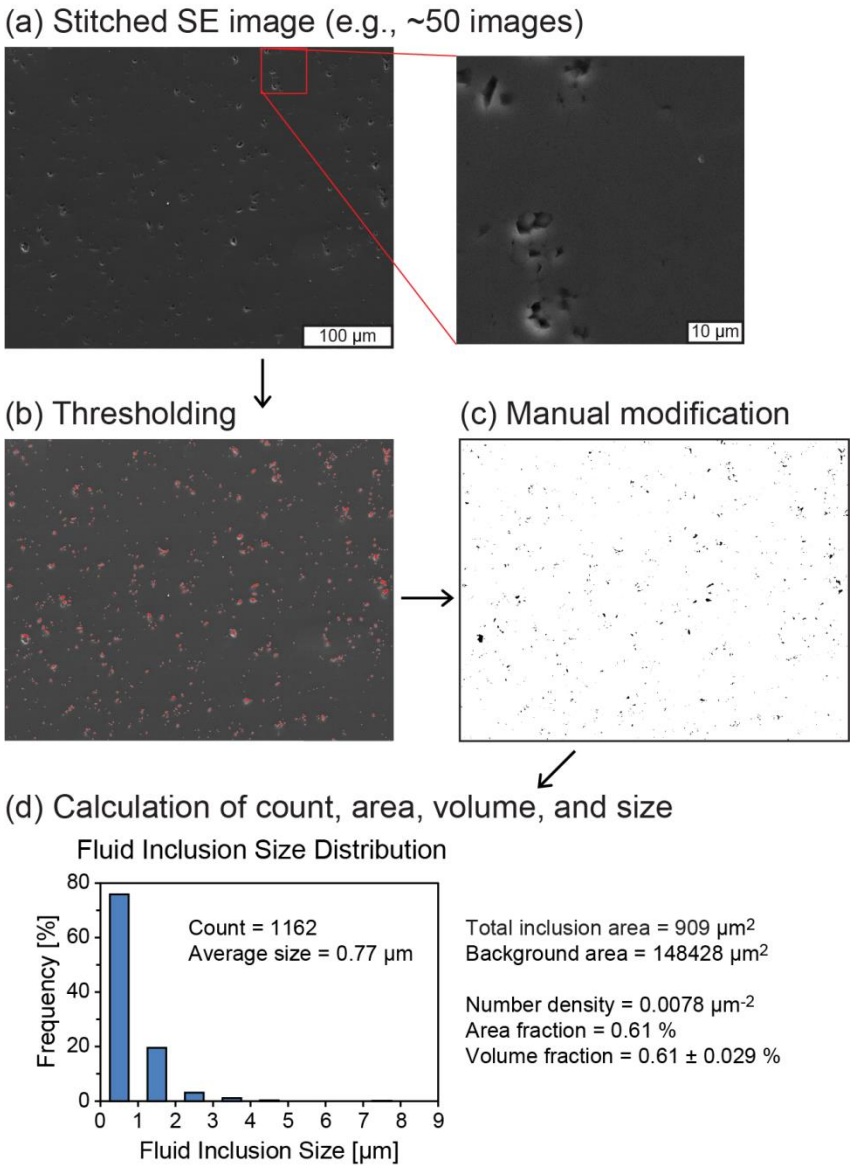

Figure 2.5. Optical image sequence of a single fluid inclusion (FI) with different focus levels. This helps to count manually fluid inclusions that are only intersected by a focal plane (in-focus) in a photomicrograph, being intended to get the same number density results as the SEM-SE images.

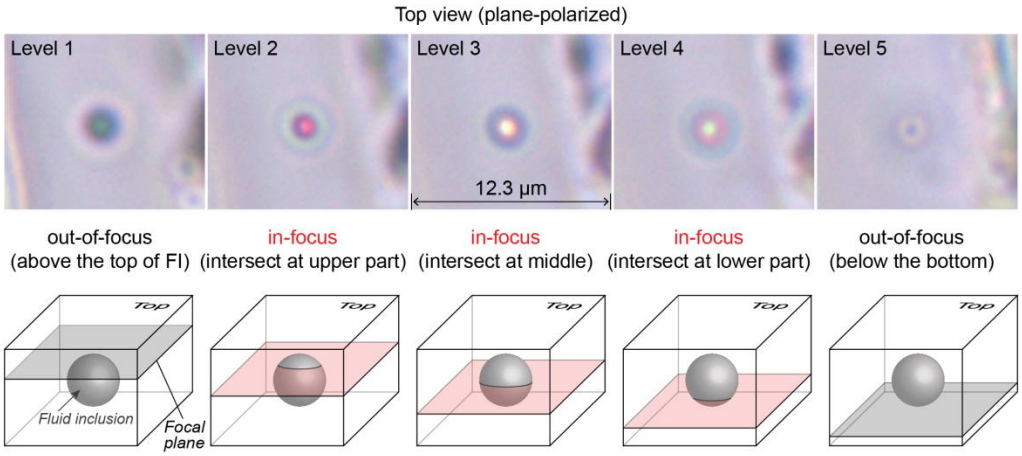

Figure 2.6. Sensitivity analysis to find an appropriate number of quartz grains, where the fluid inclusion abundance converges, by increasing the analysis area. (a) Protomylonite sample (202-QD-5) with relatively large grains, showing increases in optical number density and SEM volume fraction up to three panels. (b) Mylonite sample (201-QD-1) with relatively fine grains, displaying the same fluid inclusion abundance irrespective of the number of panels. Based on this sensitivity analysis, more than ~10 grains are required for the representative fluid inclusion abundance of each quartz domain.

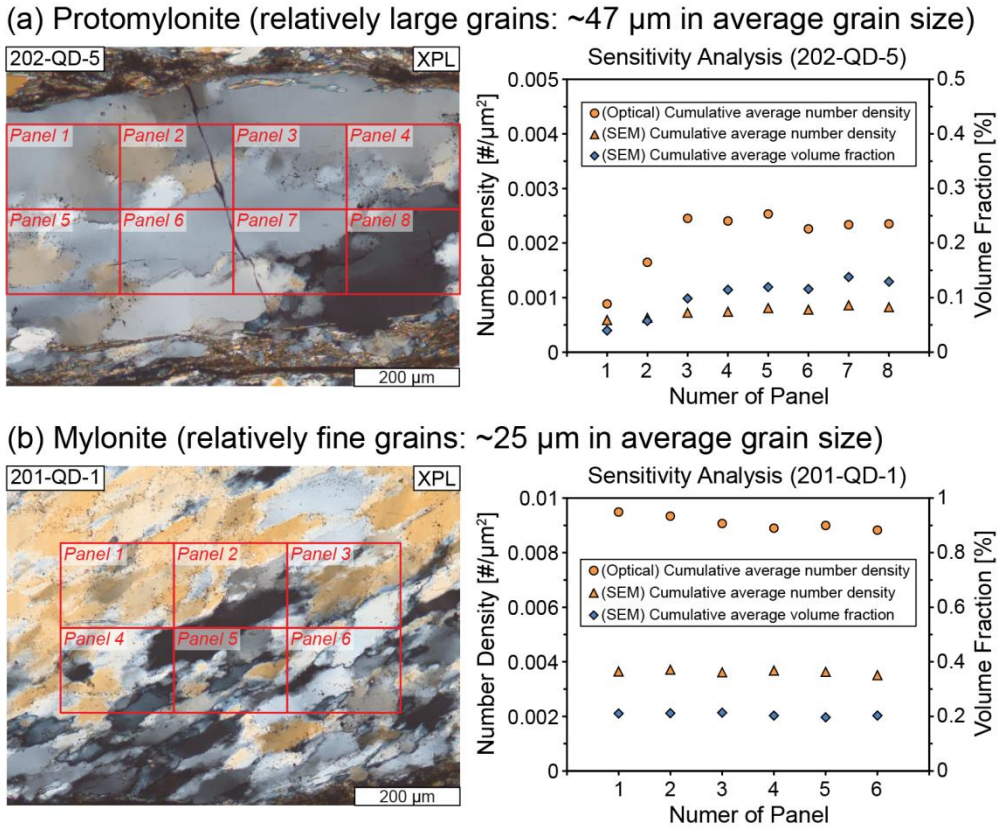

2.5. Fluid Inclusion Abundance across the Seismogenic Shear Zone

The number density and volume fraction of fluid inclusion from all the samples are plotted with respect to distance from the shear zone core to the host rock (Figs. 2.7 and 2.8). Each data point in the graphs (Figs. 2.7 and 2.8) represents the fluid inclusion abundance of each quartz domain. Because I investigate brittle damage in quartz accumulated during numerous seismic cycles with different seismic energy, and because post-seismic recrystallization can remove fluid inclusions from quartz domains (see the following sections), I consider only the maximum abundance of all the selected domains in each sample rather than using an average of measured abundances in each sample. The number density plot via SEM-SE image analysis (Fig. 2.7b) has higher values near the outer edge of the mylonite zone (~90 m from the core) than the other areas, which makes a low-high-low abundance trend from the shear zone core toward the host rock. The optical measurement of number density (Figs. 2.7a and 2.7c) reveals the low-high-low trend more clearly with a progressive increase toward the outer edge of the mylonite zone, producing a maximum value in sample NSF2. On the other hand, the volume fraction of fluid inclusion does not exhibit a clear relationship in the mylonite with distance from the core despite the same low value pattern in the protomylonite and the host rock as in the number density plots (Figs 2.7d and 2.8).

Figure 2.7. The abundance and average size of fluid inclusions with respect to distance from the shear zone core. (a) Photomicrographs to show different number densities of fluid inclusion (FI). PPL, plane-polarized light; XPL, cross-polarized light. (b) Number density graph using the SEM-SE images. (c) Number density graph using the optical measurement. (d) Volume fraction of fluid inclusion and its error only for the quartz domains with SEM maximum number densities in (b). Some data points have error bars smaller than the symbol size. (e) Average size of fluid inclusions and its standard deviation (σ) only for the quartz domains with SEM maximum number densities in (b).

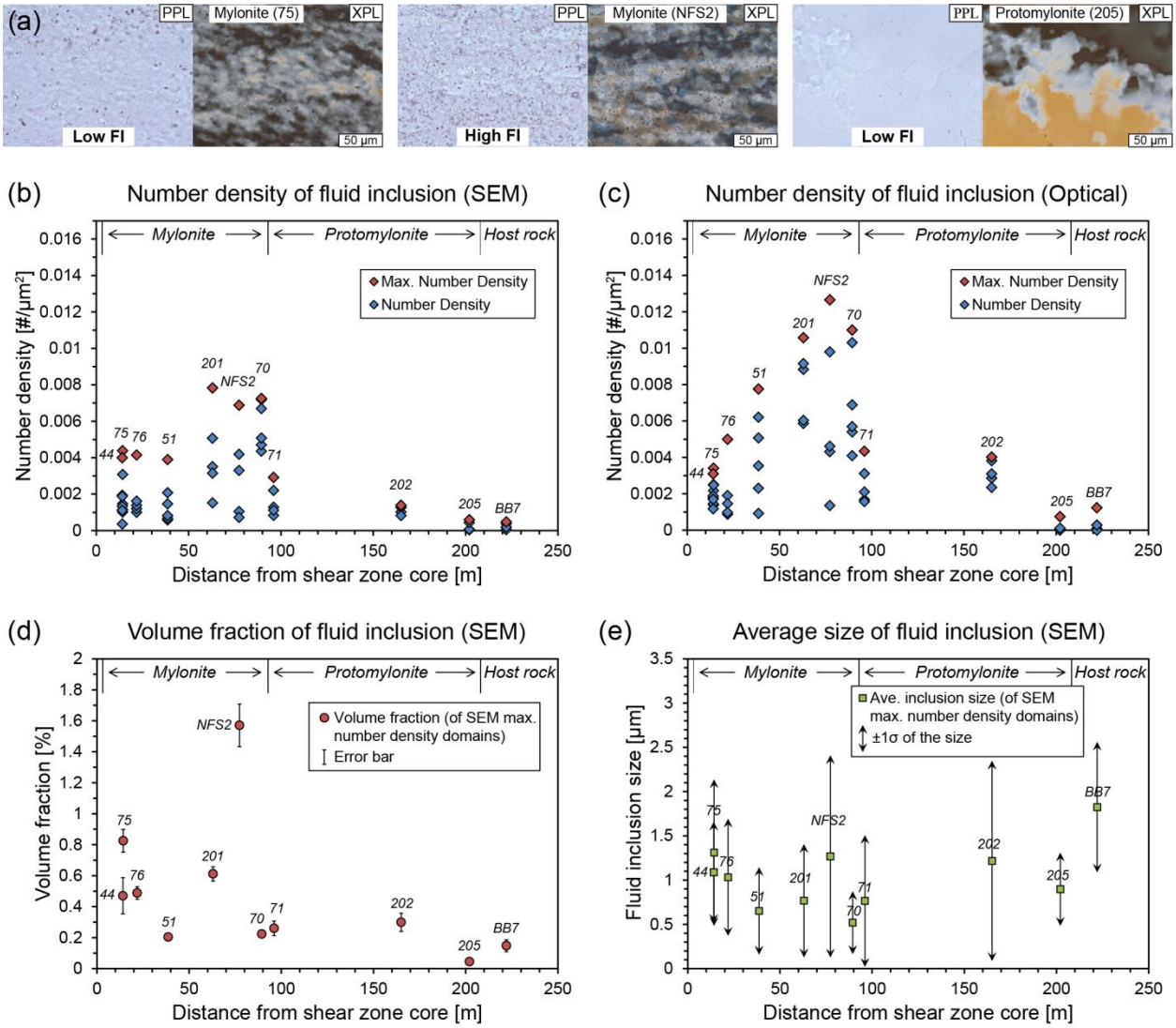

Figure 2.8. Volume fraction of fluid inclusion and its error for all the samples with respect to distance from the shear zone core. The results of the quartz domains with SEM maximum number densities in Fig. 2.7b are marked by red circle. Some data points have error bars smaller than the symbol size.

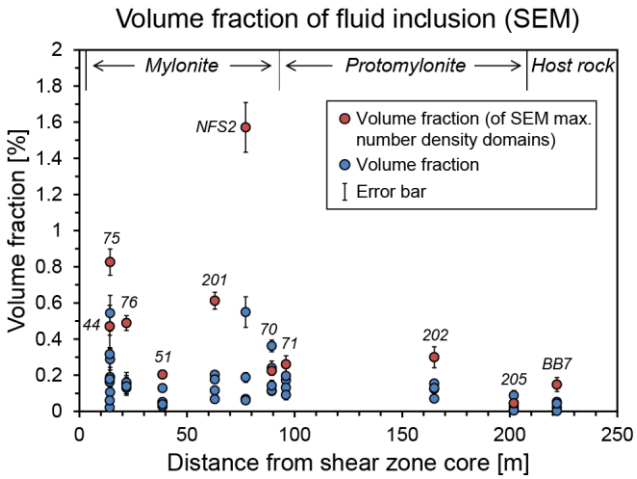

2.6. Discussion and Conclusions

2.6.1. Co-Seismic Origin of the Fluid Inclusions

I consider that the fluid inclusions observed especially in the proximity of the shear zone core originated from co-seismic damage for the following reasons, although the low-high-low trend that we document in this study is different from modern seismogenic faults showing a monotonic gradient in fracture density with proximity to the fault core (e.g., Mitchell and Faulkner, 2009). First, partially-recrystallized healed cracks decorated with fluid inclusions are found only in the mylonite (e.g., samples NFS2 and 51; Fig. 2.2d), or away from the host rock. In Fig. 2.2d, the strong correlation between fluid inclusion-rich domains and recrystallized quartz, especially within fluid inclusion-poor parent grains can be explained by neocrystallization (nucleation and growth) and ongoing recrystallization assisted by co-seismic fracturing, similar to an experimental study (Trepmann et al., 2007) which simulates deformation during co-seismic loading and post-seismic stress relaxation. Second, the low number density region in the proximity of the shear zone core (Figs. 2.7b and 2.7c) is correlated with occurrence of deformed pseudotachylyte (Fig. 2.2b). Since rupture surfaces, characterized by the deformed pseudotachylyte here, generate a higher number of healed cracks in their vicinity (e.g., Mitchell and Faulkner, 2009) due to

dynamic stress changes near the propagating rupture fronts (e.g., Poliakov et al., 2002; Andrews, 2005; Rice et al., 2005), the fluid inclusions in and near the pseudotachylyte-bearing rocks (within ~40 m from the core) are considered to originate from brittle co-seismic damage.

2.6.2. Reliable Measure of Co-Seismic Fluid Inclusion Abundance

The discrepancy in the number density results between the SEM-SE image analysis and the optical measurement (Figs. 2.7b and 2.7c) can be attributed to polishing defects and/or heterogeneous 3-D distributions of fluid inclusions. Polishing processes can create new cavities and/or erase preexisting pits (pores that had contained fluid inclusions) on thin-section surfaces, and the concentration of fluid inclusion along recrystallized grain boundaries may give rise to a heterogeneous distribution in 3-D within the thin-section. To examine these possibilities, I counted in-focus fluid inclusions from photomicrographs taken at different focal-plane depths. This sensitivity analysis shows fairly consistent values (difference of < 27 % of minimum number density in each sample) regardless of analysis areas from low to high number density (Fig. 2.9). Thus, the discrepancy between the SEM and optical results (difference of up to ~152 % of SEM data in the sensitivity analysis samples) comes mostly from polishing defects. The lower number densities for most samples in the SEM graph than in the optical results (Figs. 2.7b and 2.7c) indicate that polishing eliminated pores on thin-section surfaces. However, both SEM and optical measurements provide an outer boundary of the high number density region at a similar location (~90 m from the core) and the same trend of low-high-low number density from the core outward. Therefore, the more efficient SEM analysis of fluid inclusion number density can be used to identify an outer damage-zone boundary (between high and low number density regions; see the next section) although the more laborious optical measurements appear to be more accurate.

The lack of a low-high-low trend in the volume fraction data compared to the number density data (Figs. 2.7b, 2.7d and 2.8) implies that other mechanisms affected fluid inclusion during recrystallization after brittle co-seismic damage. Based on a similar trend of average fluid inclusion size to volume fraction with distance from the core in the mylonite (Figs. 2.7d and 2.7e), the observed trend in the volume fraction may be ascribed to fluid inclusion size rather than number density. Hollister (1990)

suggested that during dislocation creep, preferential leakage of H_2O from fluid inclusions into the crystal lattice or grain boundaries can reduce the inclusion volume (and size). Assuming this is valid, then fluid inclusion volume fraction would be more sensitive than number density to viscous deformation, and thus the number density analysis would be the more reliable measure of fluid inclusion abundance.

Figure 2.9. Sensitivity analysis of number density optically measured from photomicrographs taken at different focal-plane depths.

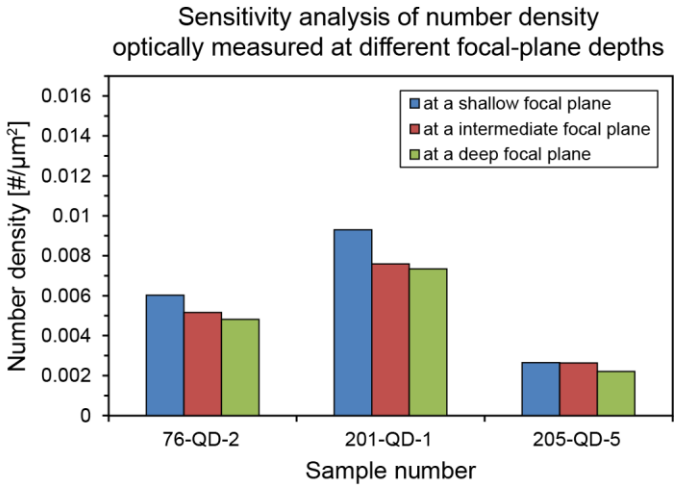

2.6.3. Estimating Width of Off-Fault Damage in the Sandhill Corner Shear Zone

Given that the shear zone core has the largest amount of deformed pseudotachylyate in the SCSZ (Figs. 2.2a and 2.2b; Price et al., 2012), co-seismic energy would likely have generated the highest abundance in fluid inclusion there, with continuous decrease away from the core. This pattern is similar to off-fault damage characteristics in the upper crust showing a logarithmic, exponential, or power decay in fracture density with distance from the fault core (e.g., Chester et al., 2005; Mitchell and Faulkner, 2009; Savage and Brodsky, 2011). However, in this case, the lower number density in the inner mylonite compared to the outer mylonite (Figs. 2.7b and 2.7c) can be explained by removal of fluid inclusions from grains through grain boundary migration during neo- and recrystallization (Kerrich, 1976; Drury and Urai, 1990; Schmatz and Urai, 2011). Multiple stages of recrystallization during post- and inter-seismic periods can progressively remove fluid inclusions contributing to the drop in abundance near the core. Another

potential mechanism for removing fluid inclusion is for migrating grain boundaries to drag inclusions to the mica-rich phase boundaries adjacent to the quartz aggregates. Once the grain boundaries carrying fluid inclusions touch phase boundaries, the fluid inclusions are lost and no longer able to be reintroduced to the recrystallizing quartz aggregate. This process may partially explain the variations of number density in the five or six quartz domains of each sample (Figs. 2.7b and 2.7c). If quartz domain thickness is considered as a proxy for its strain and age (acknowledging the possibility that quartz domains initially formed with varying thickness), the positive correlation between number density and domain thickness (Fig. 2.10) may indicate that the domain thinning by strain effectively removes brittle damage-induced fluid inclusions from quartz domains.

In summary, post- and inter-seismic recrystallization probably decreased the number of fluid inclusions more effectively in the almost fully recrystallized inner shear zone than the outer part of the mylonite, and thus the trend of low-high-low fluid inclusion number density with distance from the core may be characteristic of strike-slip faults near the base of the seismogenic zone (Fig. 2.11). Based on my data and interpretation, the minimum width of off-fault damage in the SCSZ can be taken as the boundary between high and low number density regions (~90 m from the core). A conceptual model of time-dependent fluid inclusion abundance in quartz during an earthquake cycle is proposed in Fig. 2.11.

Figure 2.10. Plot between quartz domain thickness and optical number density of fluid inclusion (FI). Samples 51 and 201 have low and high abundance, respectively.

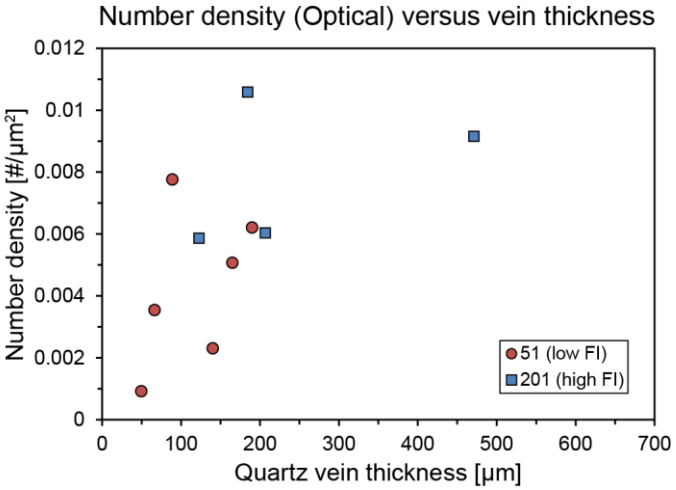

Figure 2.11. Proposed evolution model of fluid inclusion abundance during an earthquake cycle near the base of the seismogenic zone. Before an earthquake (t_0) in the shear zone core, uniform fluid inclusion abundance is assumed across the fault/shear zone. A co-seismic event (t_1) produces a highest abundance of fluid inclusion in the core and its continuous decrease away from the core, due to a gradient in fracture density. During post- and inter-seismic periods (t_2 and t_3), more strain and recrystallization in the inner part of damage zone near the core remove more effectively fluid inclusions from quartz domains than in the outer damage zone. Consequently, a relatively large quantity of fluid inclusions is survived in the outer damage zone with time. From this, a minimum (min.) width of off-fault damage zone can be estimated (from the core to the region with the highest fluid inclusion abundance).

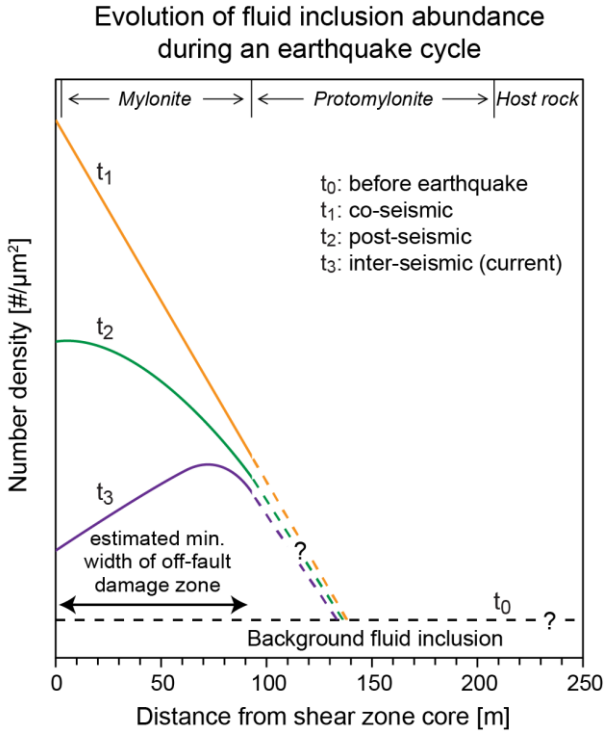

2.6.4. Implications of Off-fault Damage near the Base of the Seismogenic Zone

This geological study to assess the width of off-fault damage in deeply exhumed strike-slip faults with large-displacement demonstrates that a ~90 m wide co-seismic damage zone extends to the base of the seismogenic zone (where quartz deforms viscously at 400–500 ℃ during the inter-seismic period). Such deep penetration of damage in mature strike-slip faults would facilitate transient fluid flow and rheological changes by modifying grain size (e.g., Chester et al., 2005), permeability (e.g., Mitchell and Faulkner, 2008), and thermal structure (e.g., Morton et al., 2012; Ben-Zion and Sammis, 2013) within and surrounding the fault/shear zone core. The estimated width of off-fault damage corresponds to the outer edge of the mylonite (Fig. 2.11), and this correlation between co-seismic damage and mylonitization suggests that the inner mylonite, containing fully recrystallized quartz domains, in the immediate vicinity of the shear zone core (Fig. 2.2b) results from intensive co-seismic fracturing (possibly pulverization). This implies that off-fault damage facilitates grain size reduction of quartz by dynamic recrystallization and thus acts as a significant factor contributing to strain localization near the base of the seismogenic zone, along with deformed pseudotachylyte promoting grain-size-sensitive creep (Price et al., 2012).

CHAPTER 3

SEISMOGENIC CYCLES, QUARTZ MICROSTRUCTURES, AND LOCALIZATION AT THE FRICTIONAL-TO-VISCOUS TRANSITION IN AN EXHUMED, SEISMOGENIC, STRIKE-SLIP FAULT, MAINE, USA

3.1. Chapter Abstract

The frictional-to-viscous transition (FVT) in the vicinity of seismogenic faults experiences co-seismic fracturing/frictional sliding followed by post- and inter-seismic viscous creep. A more complete understanding of deformation processes at the FVT is important since the FVT as the strongest part in the crust controls the strength of tectonic plates and the mechanical decoupling between the upper and lower crust. Microstructural analysis of monomineralic quartz aggregates is performed on the Sandhill Corner shear zone in an ancient, seismogenic, strike-slip fault system in the northeastern Appalachians that was active at FVT depths (400–500 ℃). The shear zone core with abundant pseudotachylyte occurs at the contact between quartzo-feldspathic (QF) and schist units, and a previous study reported a brittle co-seismic damage zone (~90 m wide) in the QF unit, which corresponds to mylonites. Trends in 2-D grain size, crystallographic preferred orientation (CPO), bulk aspect ratio, and misorientation data of the QF unit from electron backscatter diffraction and image analysis show that quartz in the proximity of the core has a fine grain size (down to 8 μm), a weak CPO pattern, equant shape, and randomization in the misorientation of randomly selected pixel pairs ("random-pair"), which are indicative of grain-size-sensitive creep. The calculation of fabric intensity index (M-Index) shows a progressive weakening of the CPO toward the core in the mylonites. Within the inner shear zone (~40 m wide) containing fully recrystallized quartz domains, the microstructural parameters are unusual, with near-random random-pair misorientations but a CPO pattern clearly indicative of basal <a> slip. The data confirm and build new evidence for the model that during the seismic cycle, quartz grains within the inner shear zone experienced cycles of (a) extensive fracturing (possibly pulverization) by co-seismic energy, (b) grain-size reduction by neocrystallization followed by post-seismic viscous creep dominantly through grain-

size-sensitive processes, and (c) further recrystallization with progressive grain growth, transitioning to basal <a> slip. This suggests that such micromechanical cycle facilitates long-term localization and stabilization of the shear zone at FVT depths. On the other hand, the schist unit neither has fully recrystallized quartz nor the microstructural characteristics of the inner shear zone except the shear zone core (~5 m wide). The asymmetrical spatial extent of the quartz microstructures indicative of transient extensive damage around the core may indicate a strongly preferred rupture propagation direction, commonly observed in strike-slip faults with bimaterial interfaces.

3.2. Chapter Introduction

Mature fault zones are strongly localized by strain weakening (e.g., Ben-Zion and Sammis, 2003). Processes of strain localization at various depths are a key factor for understanding crustal-scale fault evolution and rheology of the continental crust associated with earthquake cycles. The frictional-to-viscous transition (FVT; ~10–20 km deep) between the brittle upper crust and the viscous lower crust is the strongest part of the continental lithosphere along with the upper-most part of the mantle (Brace and Kohlstedt, 1980; Kohlstedt et al., 1995; Handy et al., 2007). Thus, a more complete understanding of deformation processes at the FVT is important owing to its control over the strength of tectonic plates and the mechanical decoupling between the upper and lower crust. However, well-preserved microstructural records from this depth are rarely preserved in exhumed faults because of progressive deformation and metamorphism during exhumation.

Quartz is among the most important constituents of the Earth's continental crust because of not only its high volume proportion but also its significant role in controlling the crustal rheology (e.g., Lowry and Pérez-Gussinyé, 2011). The mechanisms by which quartz deforms at depth are dependent on transient fluctuations in stress and strain-rate associated with seismic cycles (e.g., Handy et al., 2007). At the FVT, where temperatures exceed the onset of quartz plasticity, quartz deforms viscously by, for example, dislocation creep in long, inter-seismic periods, but can also be fractured during co-seismic rupture owing to transiently high stress and strain-rate. After the rupture ceases, or during post-seismic stress relaxation, the fractured quartz can experience neocrystallization (nucleation and growth; Trepmann

et al., 2007) and recrystallization and, as a result, exhibit smaller grain size than the parent quartz. This grain-size reduction acts as a strain weakening process contributing to localization in mid-crustal fault zones.

We investigate deformation microstructures in monomineralic quartz aggregates from the Sandhill Corner shear zone (SCSZ), a strand of the Norumbega fault system (an ancient large-displacement, subvertical strike-slip fault system in the northeastern Appalachians) that has been exhumed from FVT depths (400–500 ℃) to characterize in greater detail the previously proposed architecture that divides the shear zone into an outer and inner shear zone (Johnson et al., 2009; Price et al., 2012, 2016). The SCSZ has mutually overprinting pseudotachylite and mylonite (Price et al., 2012), which is clear geologic evidence for earthquake cycles at the FVT (e.g., Hobbs et al., 1986; Handy et al., 2007). Chapter 2 also demonstrated that a brittle co-seismic damage zone with at least ~90 m width exists in the SCSZ. Although Price et al. (2016) showed some quantitative data of quartz such as crystallographic preferred orientations (CPO) and misorientations from the SCSZ, there has been no systematic study on deformation mechanism of each characteristic zone (e.g., extensively damaged zone, less damaged zone, and undamaged zone) in FVT shear zones. I provide quartz data of grain size, fabric intensity index (M-Index), shape preferred orientation (SPO) as well as CPO and misorientations from the SCSZ core to the host rocks, including additional analyses with finer sample spacing than reported in Price et al. (2016). Using the quantitative data, I discuss deformation processes of quartz in the SCSZ associated with the earthquake cycle.

3.3. Geologic Setting

The SCSZ is the longest continuous strand in the Norumbega fault system (Fig. 3.1; Johnson et al., 2009; Price et al., 2012, 2016). The Norumbega fault system is a long-lived, Paleozoic, large-displacement, right-lateral strike-slip fault system in the northeastern Appalachians (Ludman and West, 1999), and seismic reflection data reveal its penetration down to the Moho (Doll et al., 1996). Currently exposed rocks in the Norumbega are upper amphibolite facies in the southwest to sub-greenschist facies in the northeast because of different erosion levels (Ludman and West, 1999). Thus, the Norumbega is an

ancient analogue to active tectonic-scale strike-slip fault systems at mid-crustal depths such as the San Andreas fault. The SCSZ (~230 m wide in the study area) located in the central part of the Norumbega fault system contains mutually overprinting pseudotachylyte and mylonite (Price et al., 2012), indicating a seismically active zone at FVT depths (Handy et al., 2007). The shear zone inside the quartzo-feldspathic Cape Elizabeth Formation has its core at the contact with the schistose Crummett Mountain Formation in the study area (Figs. 3.1 and 3.2a; Grover and Fernandes, 2003; West and Peterman, 2004; Price et al., 2016). The Cape Elizabeth Formation as a parent rock of the quartzo-feldspathic (QF) unit in the SCSZ is a quartz-plagioclase-biotite±garnet±sillimanite metasedimentary rock that underwent partial migmatization and upper amphibolite-facies metamorphism (Grover and Fernandes, 2003; West and Peterman, 2004). The Crummett Mountain Formation (West and Peterman, 2004; equivalent to Scarboro Formation of Grover and Fernandes, 2003) as a parent rock of the schist unit in the other side of the SCSZ is a quartz-plagioclase-garnet-staurolite-andalusite mica schist with discontinuous, complexly-folded quartz veins. The SCSZ is characterized by a ~200 m wide protomylonite to mylonite in the QF unit, a ~5 m wide ultramlonite in the shear zone core, and a ~25 m wide highly-sheared schist in the schist unit (Fig. 3.2a; Price et al., 2016). The lineations of previously and newly collected samples in the study area that have subvertical foliations are parallel to the strike of the SCSZ (Fig. 3.1). The mylonitization generally increases toward the shear zone core, which is demonstrated by the abundance of porphyroclasts of feldspars, garnet, and muscovite with respect to distance from the core (Fig. 3.2b). Chapter 2 reported a brittle co-seismic damage zone (~90 m wide) in the QF unit, which corresponds to mylonites (Fig. 3.2b).

Monomineralic aggregates of quartz embedded in mica-rich matrix that we analyzed from the SCSZ are deformed or folded quartz veins or ribbons. However, it is unclear that the quartz domains originally came from felsic layers of the QF host rock in the QF unit or quartz veins formed under higher-temperature conditions and/or during lower-temperature deformation directly related to seismic cycles in both units (Price et al., 2016; Chapter 2). Quartz in the host rocks shows grain boundary migration (GBM) recrystallization, but SCSZ quartz was recrystallized dominantly by subgrain rotation (SGR) (Fig. 3.2c; Price et al., 2016). The degree of SGR recrystallization increases toward the core (Fig. 3.2c). The

mylonitic deformation under seismic conditions at FVT depths occurred at temperatures of 400–500 ℃, overprinting previous higher-temperature microstructures preserved in the host rocks outside the shear zone (Price et al., 2016).

Figure 3.1. Geologic setting of Sandhill Corner shear zone.

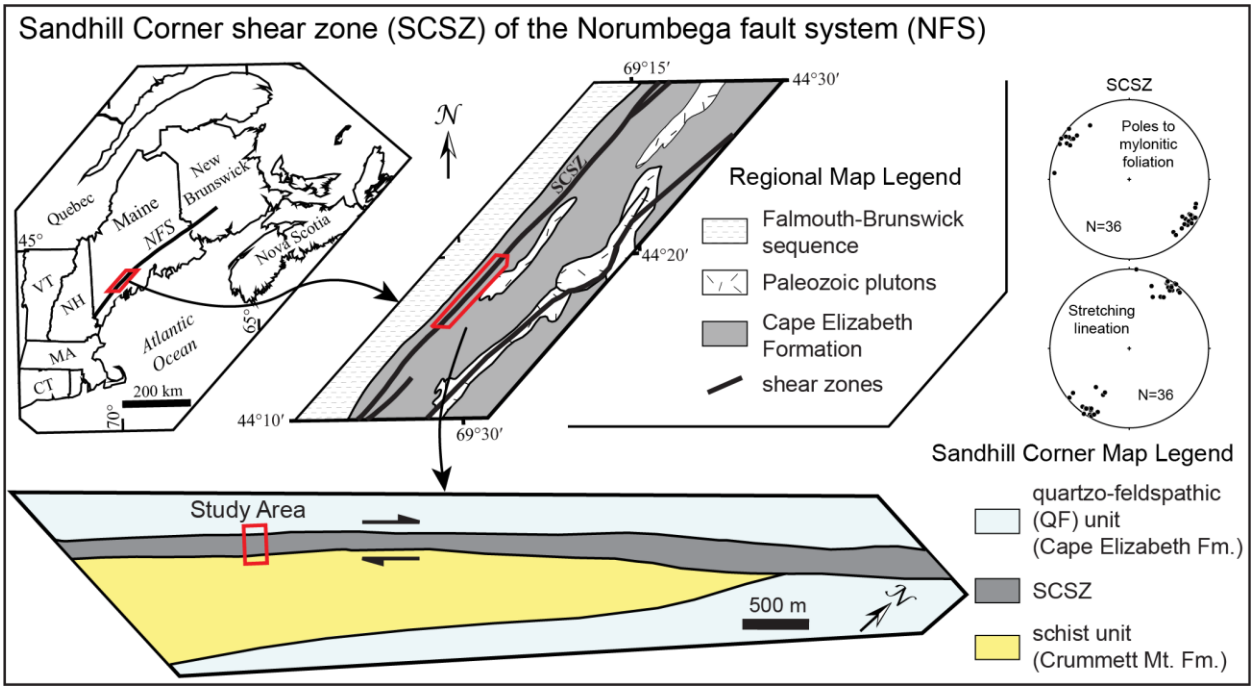

Figure 3.2. Sample locations and quartz microstructures. (a) Sample locations and rock types. (b) Area percentage of clast and pseudotachylyte (PST) with respect to distance from the shear zone core. The modal percentage of clast is calculated except quartz domains. The modal clast generally decreases from each host rock toward the core. Note much higher occurrence of PST in the QF unit than the schist. The clast and PST data include the previous studies (Price et al., 2012, 2016). The boundaries and core of the shear zone are marked by dashed lines, connected to (a). A ~90 m wide transient co-seismic damage zone exists in the QF unit (Chapter 2). (c) Quartz photomicrographs (cross-polarized) showing an increase in recrystallization toward the core.

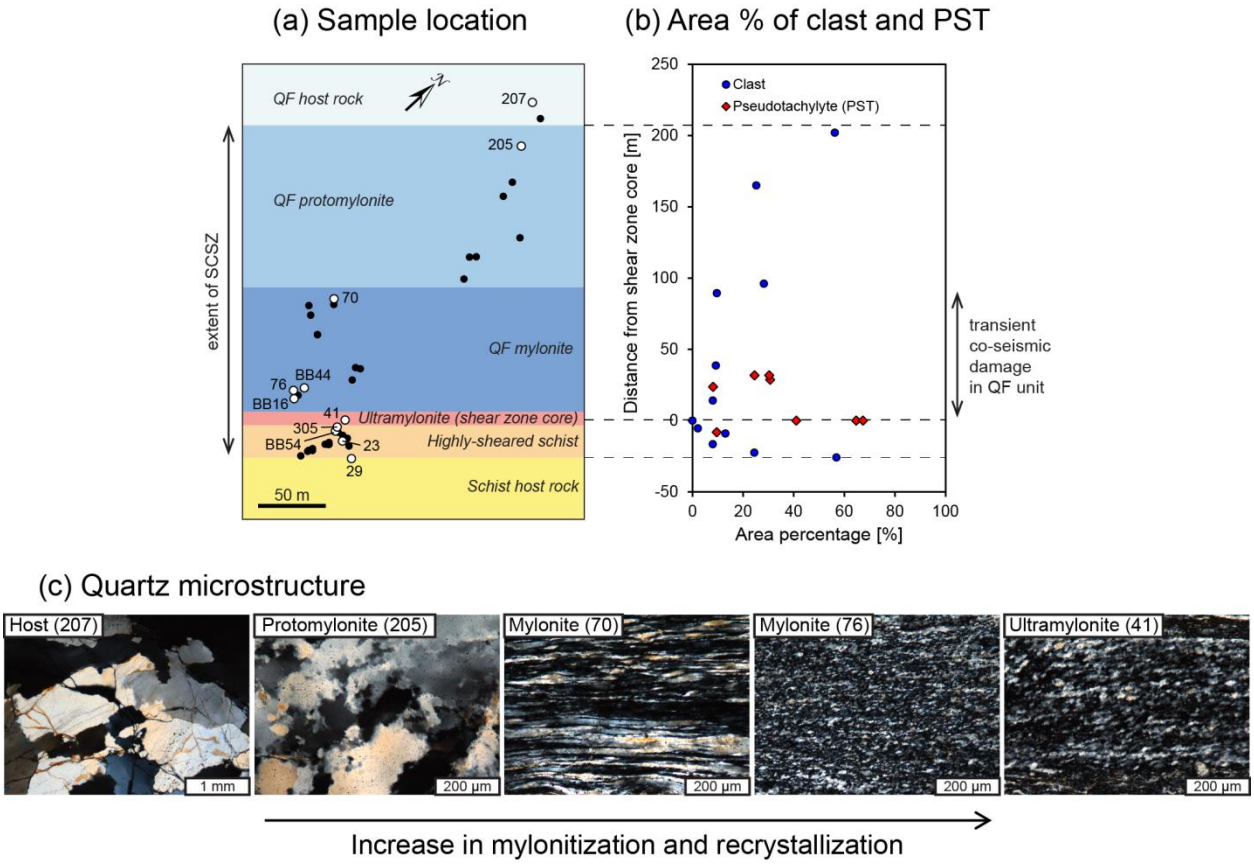

3.4. Possible Evidence for Co-Seismic Damage

Quartz in the FVT does not record direct evidence of co-seismic brittle damage such as microfracturing due to post- and inter-seismic viscous deformation and dynamic recrystallization. However, the SCSZ abounds with well-preserved microstructural evidence for what I interpret as co-seismic damage such as deformed pseudotachylyte and shattered grains of brittle minerals. These microstructures are commonly interpreted to reflect cycles of co-seismic stress loading and post- or inter-seismic stress relaxation.

3.4.1. Deformed Pseudotachylyte

Pseudotachylyte is a glassy or very fine-grained rock, interpreted as quenched frictional melt, and most widely accepted as evidence for earthquake slip in ancient faults (Sibson, 1975; Kirkpatrick and Rowe, 2013). Almost pristine pseudotachylyte and pseudotachylyte-derived ultramylonite are found in the SCSZ (Price et al., 2012). New samples collected from the inner shear zone in the study area also have deformed (Fig. 3.3a) and less-deformed pseudotachylyte (Fig. 3.3b); each cuts porphyroclast of plagioclase and fragmented garnet, respectively. The less-deformed pseudotachylyte contains wall-rock fragments with a wide range of size (Fig. 3.3b). The ~5 m wide shear zone core with ultramylonite derived from pseudotachlyte (Fig. 3.2a) is considered as evidence for a long history of repeated co-seismic brittle and inter-seismic viscous deformation at the FVT (e.g., Sibson, 1980; Passchier, 1982; Hobbs et al., 1986; Price et al., 2012). The abundance of deformed pseudotachylyte in the SCSZ generally increases toward the core (Price et al., 2012), but being asymmetrically distributed between the QF and schist units (Fig. 3.2b).

Figure 3.3. Possible evidence for co-seismic damage. (a) Pseudotachylyte (PST) from the QF mylonite (sample BB44). (b) PST from the highly sheared schist (sample BB54) (c) Shattered garnet porphyroclast from the shear zone core (sample 41). (d) Shattered plagioclase porphyroclast from the QF mylonite (sample BB16). pl, plagioclase; grt, garnet; qtz, quartz; PPL, plane-polarized light, XPL, cross-polarized light, Reflect, reflected light; BSE, backscattered electron; CL, cathodoluminescence.

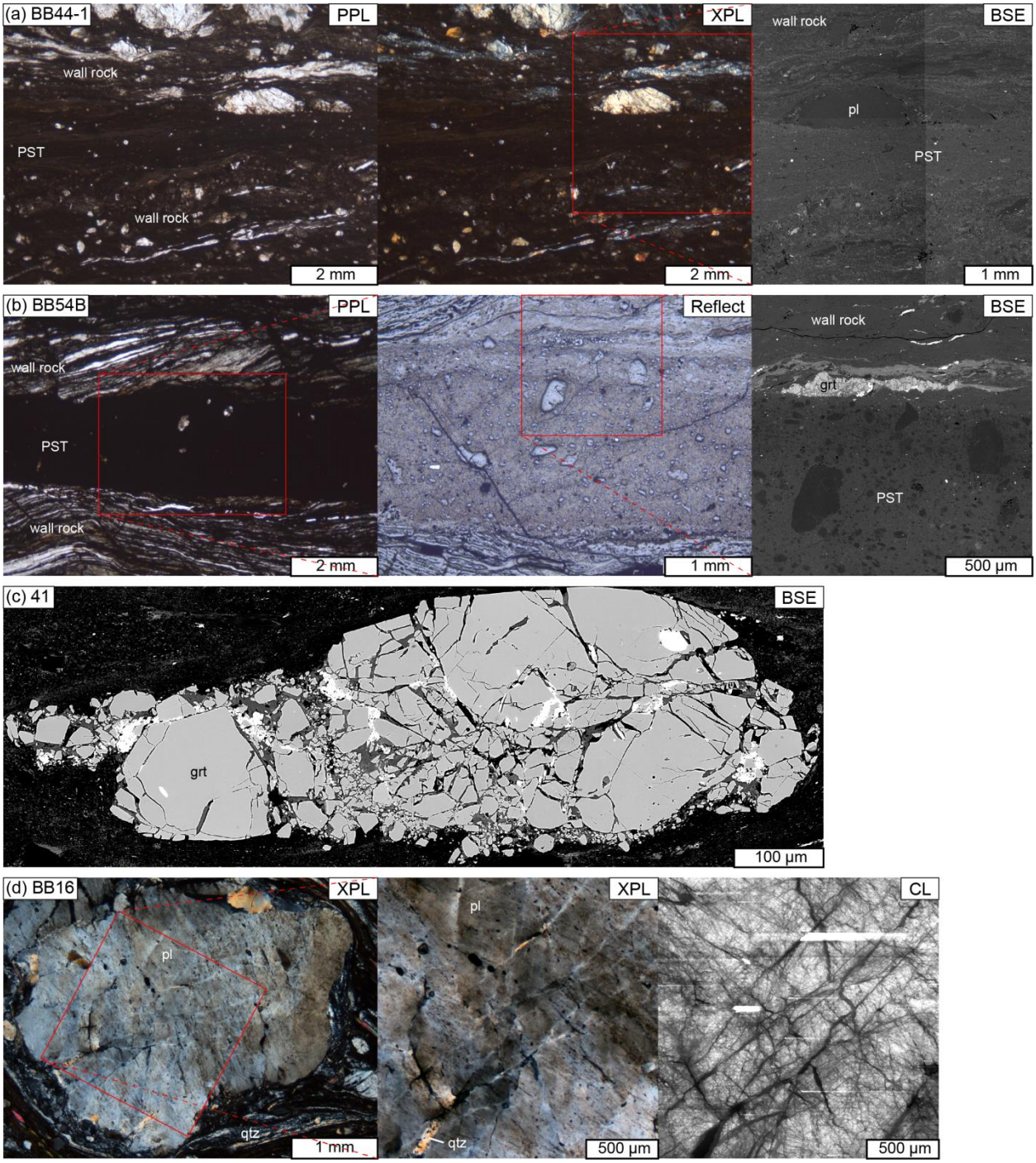

3.4.2. Shattered Mineral Grains

Co-seismic loading can shatter mineral grains such as garnet and feldspar porphyroclasts (e.g., Trepmann and Stöckhert, 2002; Austrheim et al., 2017; Sullivan and Peterman, 2017). The SCSZ core and inner shear zone have fragmented garnet and shattered feldspars (Figs 3.3c and 3.3d). Figure 2c is backscattered electron (BSE) image of a shattered garnet grain with fragments down to the sub-micron scale from the core, showing shear displacement. Figure 3.3d shows optical and cathodoluminescence (CL) images of a shattered plagioclase grain from the inner shear zone. Optically, the grain shows two or three generations of cross-cutting quartz-filled cracks, and in the CL image, thin line networks are extensive tensile microcracks in plagioclase, which are overprinted by quartz-filled cracks (Fig. 3.3d).

3.5. Analytical Methods

Samples collected from the QF host rock, the SCSZ, and the schist host rock (Fig. 3.2a) were cut perpendicular to local foliations and parallel to local lineations, which are sub-parallel to the contact between both units. Thin sections were polished mechanically with a 0.3 μm alumina suspension and chemically in a 0.02 μm colloidal silica suspension for at least an hour to remove surface damage. To investigate 'unbiased' deformation records in quartz accumulated during many seismic cycles, we analyzed a number of quartz veins and ribbons, if present, in a thin section, which have differently accumulated strains in a sample depending on their ages. Due to heterogeneous deformation on thin-section scale (folding or different strain around porphyroclasts), analysis areas in quartz domains were determined avoiding fold hinges and proximity of porphyroclasts. Electron backscatter diffraction (EBSD) data were obtained on thin carbon coated samples to prevent electron charging, using the Tescan Vega II Scanning Electron Microscope equipped with an EDAX-TSL EBSD system at the University of Maine, USA. Simultaneous chemical analysis was performed via EDAX Genesis Energy Dispersive Spectroscopy to identify and filter other phases in and around quartz domains. Diffraction patterns were acquired using EDAX-TSL OIM Data Collection 5.31 software at an acceleration voltage of 20 kV, a beam current of ~6 nA, a 70° sample tilt, and high-vacuum conditions. EBSD data were collected with a

square grid at step size between 2 and 8 μm depending on average grain size. Raw indexing rates of quartz were >98 %.

Post-processing of quartz EBSD data were conducted by EDAX-TSL OIM Analysis 5.31 software based on confidence index (CI) and neighboring orientations to produce clean EBSD maps. Non- and poor-indexed pixels (CI < 0.1) were replaced with well-indexed neighboring pixels of CI > 0.1. The well-indexed pixels ranged between 62% and 96% of analyzed pixels. Grains in post-processing are defined by an internal misorientation <10° and a minimum grain size of 4 pixels. The cleaned EBSD data are used to present CPO and misorientation distribution, and calculate grain size, recrystallization fraction, and fabric strength (M-index; Skemer et al., 2005). Misorientation-angle distributions are derived from all neighboring pixels ("neighbor-pair") and the same amount of randomly selected pixels ("random-pair") as the neighboring pixels. For grain size calculation and CPO presentation, Dauphiné twins in quartz are removed, and they are applied to whole and recrystallized quartz. To determine recrystallized small grains, grain size distributions by area fraction are used, in which maximum size of recrystallized grain is selected before the second peak when showing bimodal distribution. Such separation between small recrystallized and large parent grains is confirmed in the EBSD maps based on their sizes and shapes. Grain size in grain size distributions is defined by equivalent circular diameter of measured grain area, but 2-D average grain size of each quartz domain is calculated by the root mean square for use of paleopiezometer of Stipp and Tullis (2003). For pole figures, single average orientation per grain is plotted in equal area, upper-hemisphere projection, and their contouring is also presented by multiples of uniform distribution. In each pole figure, the local lineation (X) and the pole to the local foliation (Z) are oriented east-west and north-south, respectively. For SPO analysis, PAROR (Panozzo, 1983) and SURFOR (Panozzo, 1984) are used in calculating a bulk aspect ratio (long/short) of all grains in each quartz domain, and displaying their shape fabrics on a rose diagram, respectively. Before using PAROR and SURFOR programs, 'pixelated' grain boundary images from the EBSD maps are smoothed by a macro program (Jazy XY export header) in *ImageJ* (https://imagej.nih.gov/ij/). The programs PAROR, SURFOR, and the macro program are available at https://earth.unibas.ch/micro/.

3.6. Quartz Microfabrics across Sandhill Corner Shear Zone (SCSZ)

This section focuses on the quantification of microstructure parameters (e.g., size and shape) and crystallographic orientation. The optical observation of quartz microstructure in the SCSZ is well described in Price et al. (2016).

3.6.1. Grain Size and Recrystallization Fraction

Host rocks of both QF and schist units have large quartz grains up to mm-scale, and the range of quartz grain size decreases to a few tens of micrometers toward the shear zone core (Fig. 3.4). Grain size distributions of recrystallized quartz in each sample follow a log-normal distribution (Fig. 3.4), which is typical for dynamically recrystallized tectonites (Ranalli, 1984). Average grain size of whole quartz (parent and recrystallized grains) in each quartz domain (Fig. 3.5a) reveals that the pattern of variation in grain size correlates to recrystallization fraction (Fig. 3.5c). With increasing recrystallization fraction toward the shear zone core, the average grain size of whole quartz also decreases. However, the average grain size of recrystallized quartz shows fairly uniform ranges of 13–38 μm and 18–51 μm, respectively, for the QF and schist units in the outer parts of the shear zone, but drops to 8–21 μm in the inner part of the shear zone within ~40 m of the core (Fig. 3.5b). Here I call the inner part of the SCSZ (~40 m wide around the core) an “inner shear zone”, containing fully recrystallized quartz domains, and the other parts of the SCSZ a “QF or schist outer shear zone”. Different data points at a same distance from the core in Fig. 3.5 represent different quartz domains in a thin section. The variations in recrystallized grain size and fraction from each sample reflect heterogeneous deformation or differently accumulated strain at the thin-section scale.

Figure 3.4. Grain size distributions of whole and recrystallized quartz. Equivalent circular diameter of measured grain area is used as 2-D grain size here.

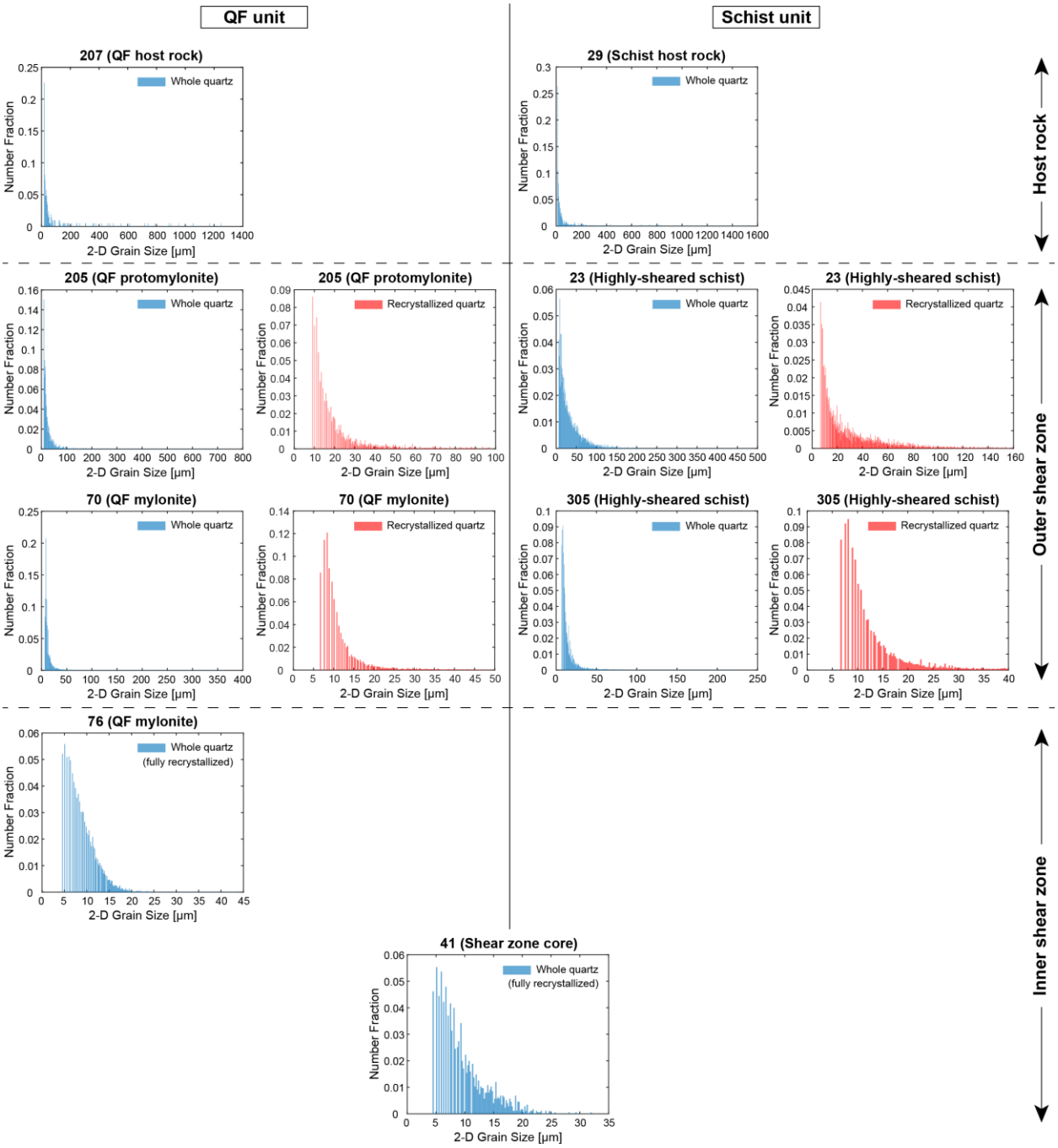

Figure 3.5. 2-D average grain size and recrystallized area fraction. The average grain size is calculated by the root mean square. (a) Average grain size of whole quartz. (b) Average grain size of recrystallized quartz. (c) Area fraction of recrystallized quartz. The inner shear zone (SZ) contains fully recrystallized quartz domains.

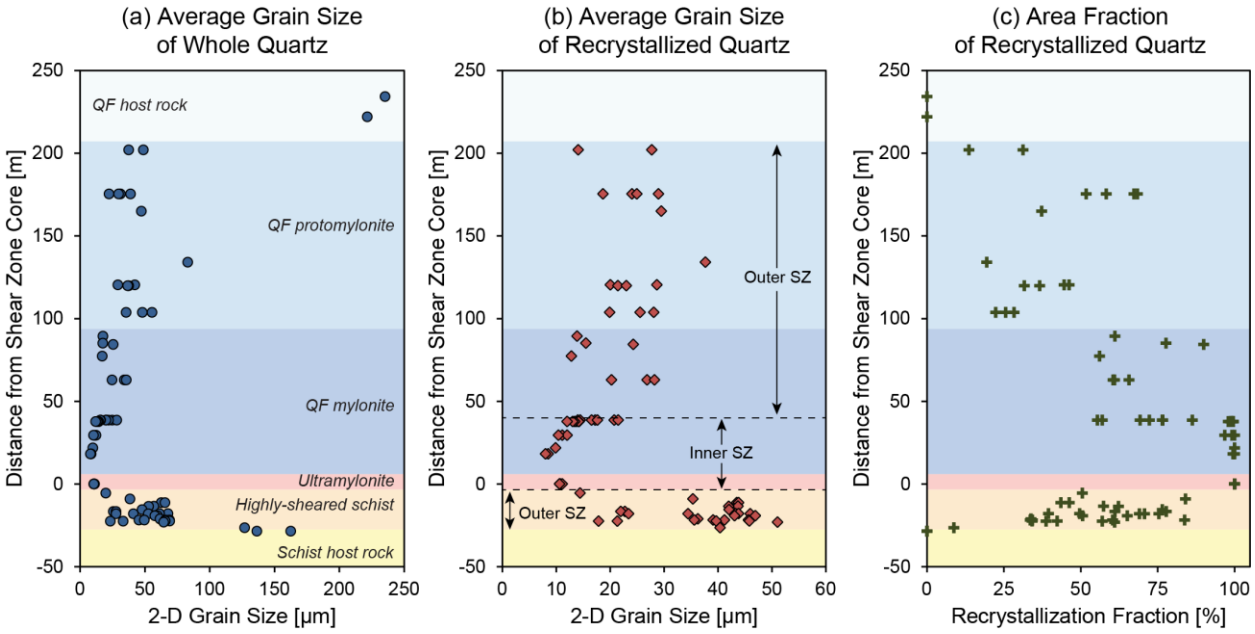

3.6.2. Shape Preferred Orientation (SPO)

The degree of SPO can be estimated by calculating a bulk aspect ratio of polycrystalline quartz aggregates. Fig. 3.6 shows preferred orientation of particles (PAROR) and of grain surfaces (SURFOR) presented as orientation distribution functions (i.e., length weighted rose diagrams) of long axes (defined by the projection normal to the shortest) and surface elements, respectively. The bulk aspect ratio is determined by the ratio of the maximum to the minimum of a projection curve in PAROR program (i.e., 1 is equant shape, infinite is line) and is shown in Fig. 3.7 for all the samples. The QF host rock shows a relatively weak SPO (bulk aspect ratio of 1.2–1.4), but the mylonite in the outer shear zone displays high bulk aspect ratios up to ~2.5 for whole quartz due to very highly elongated parent grains (aspect ratio > 20) parallel to the foliation. The inner shear zone that contains fully recrystallized quartz has very weak SPO or equant grains (minimum bulk aspect ratio of ~1.1). The schist unit reveals similar trend to the QF rock for whole quartz; highest bulk aspect ratio of ~2.1 in the center of the highly-sheared schist decreases

toward the core and the schist host rock (bulk aspect ratio of ~1.4) (Fig. 3.7a). Recrystallized quartz in the outer shear zones has fairly uniform SPO around aspect ratio of ~1.8 with some variations (Fig. 3.7b).

Figure 3.6. Surface (SURFOR) and particle (PAROR) orientation distribution functions. Bulk aspect ratio (long/short) is indicated for the particle fabric.

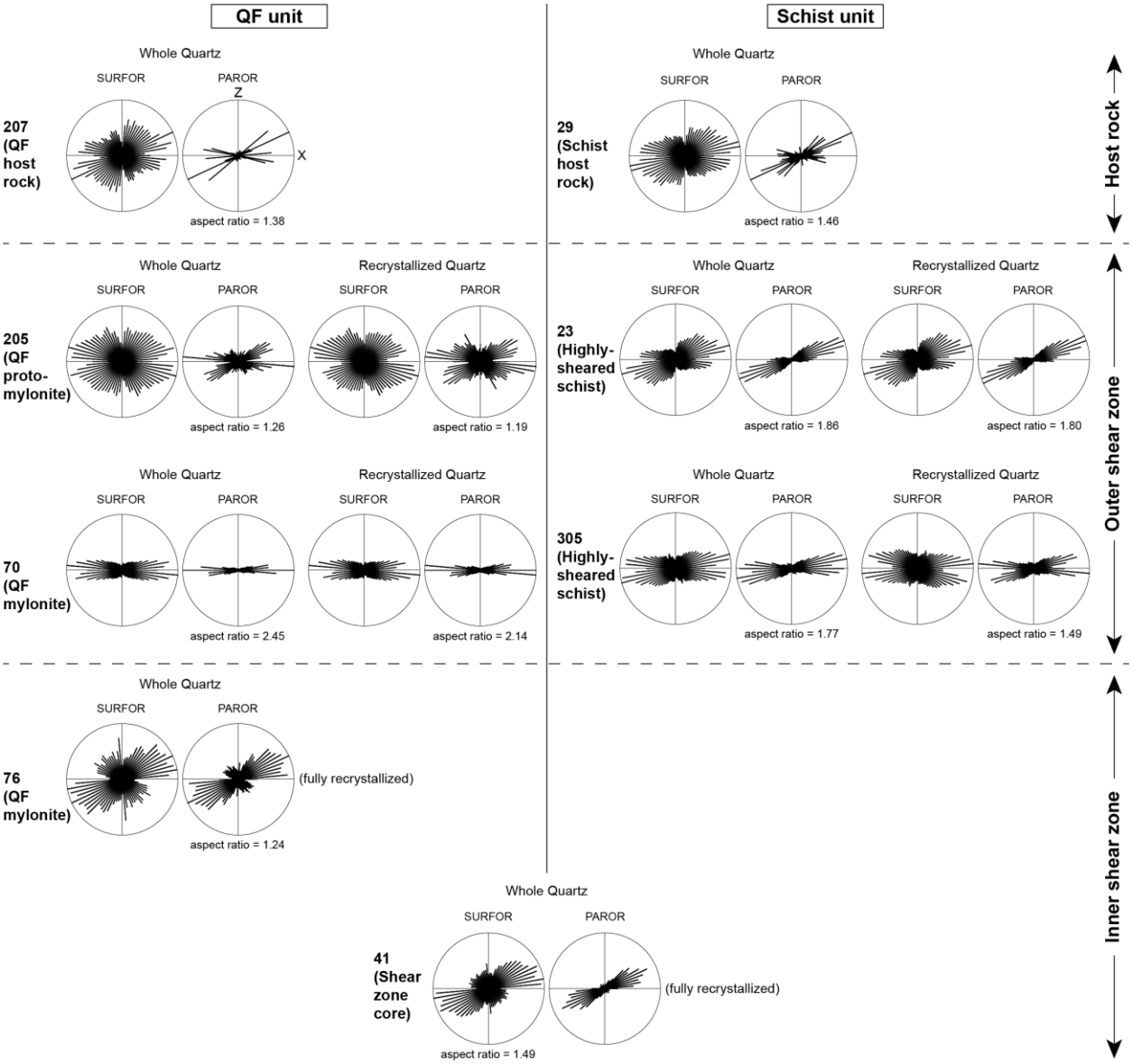

Figure 3.7. Bulk aspect ratio (long/short) from PAROR program. (a) Bulk aspect ratio of whole quartz. (b) Bulk aspect ratio of recrystallized quartz.

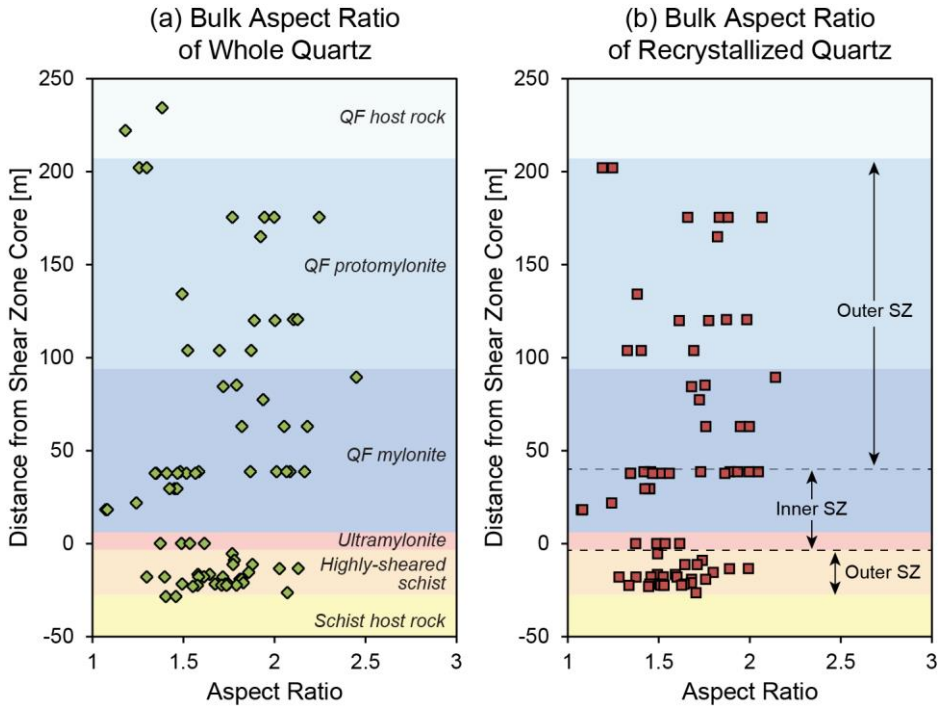

3.6.3. Crystallographic Preferred Orientation (CPO)

Host rock quartz and parent quartz in the SCSZ show a strong CPO with a c-axis maximum in the center or between the center and the peripheral of the pole figures (Fig. 3.8). The c-axis pole figures of recrystallized quartz in the outer shear zone display single or Type I crossed girdle fabrics (Schmid and Casey, 1986) (see the discrete pole figure plots in Fig. 3.8), but still have the same maximum orientations as the parent quartz (see the contoured pole figures). Fully recrystallized quartz domains in the inner shear zone have a c-axis maximum close to the foliation pole (Z) in the pole figures. I note that sample 76 in the inner shear zone exhibits wide scattering of crystallographic orientation in the discrete pole figure (Fig. 3.8).

Figure 3.8. Contoured and discrete pole figures of quartz c-axis (0001) and a-axis (11-21). One point per grain is plotted.

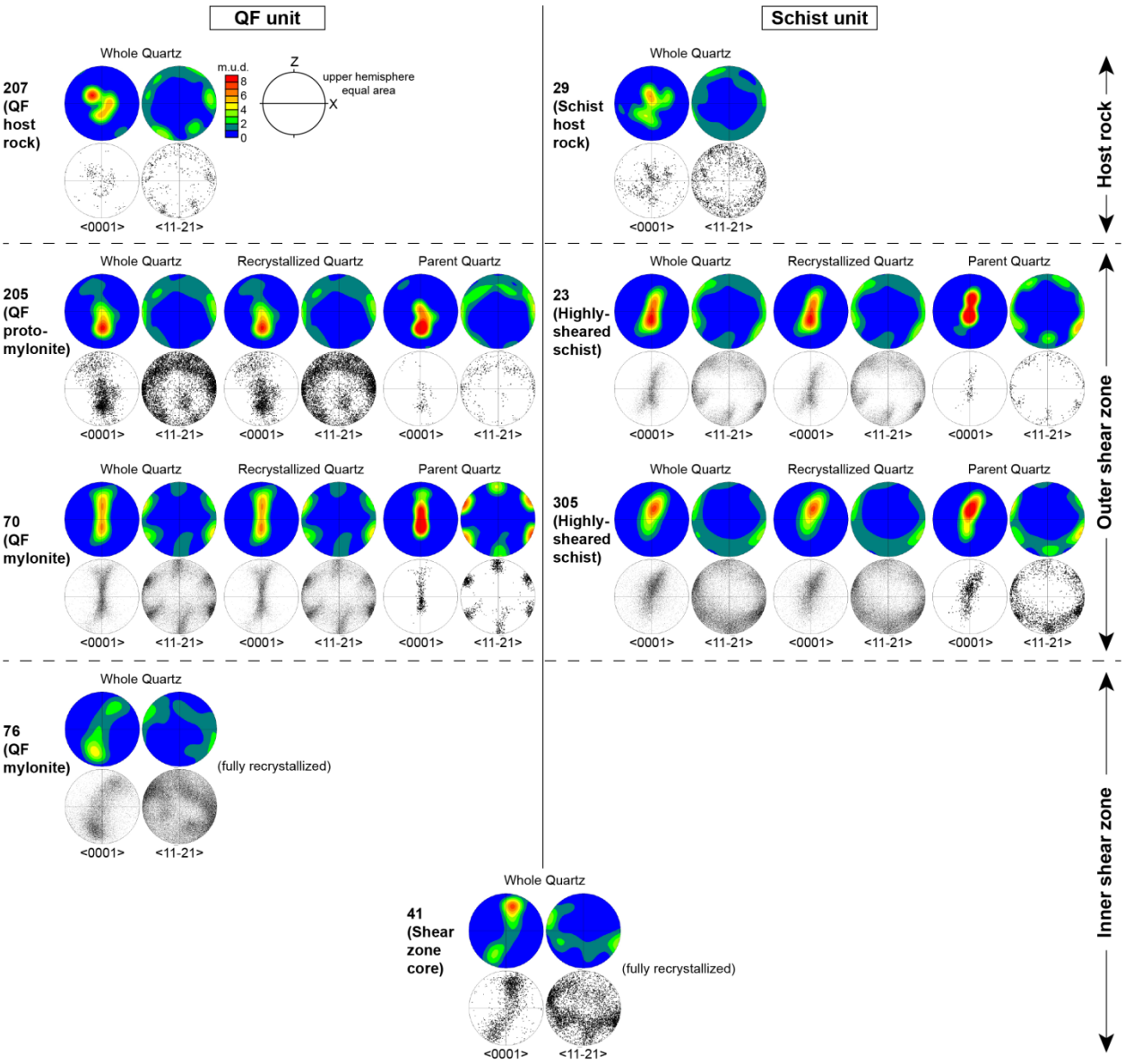

3.6.4. Misorientation Angle

Fig. 3.9 describes histograms of neighbor-pair (correlated) and random-pair (uncorrelated) misorientations overlaid on theoretical random graph of quartz with a bin size of 5°. For recrystallized quartz, only random-pair profile is plotted to calculate fabric strength (see the next section). In neighbor-pair profile of whole quartz, misorientation angles at <10° and the 60° peak indicate subgrain boundaries

and Dauphiné twinning, respectively (Wheeler et al., 2001). In the host rocks, both neighbor-pair and random-pair profiles have low fraction at 10°–40° and >70°. In the outer shear zones, with increasing strain and recrystallization toward the inner shear zone, the fraction at low angles (10°–40°) for both neighbor-pair and random-pair profiles increases but remains low at high angles (>70°), making an increased deviation of random-pair profile from the theoretical random (Fig. 3.9). The fully recrystallized quartz in the inner shear zone shows random-pair profile close to the theoretical random and neighbor-pair misorientation with high fraction at high angles (>70°) (Fig. 3.9).

Figure 3.9. Misorientation angle histogram plots. They show the neighbor-pair (red dotted line), random-pair (blue solid line), and theoretical random (green dashed line) profiles.

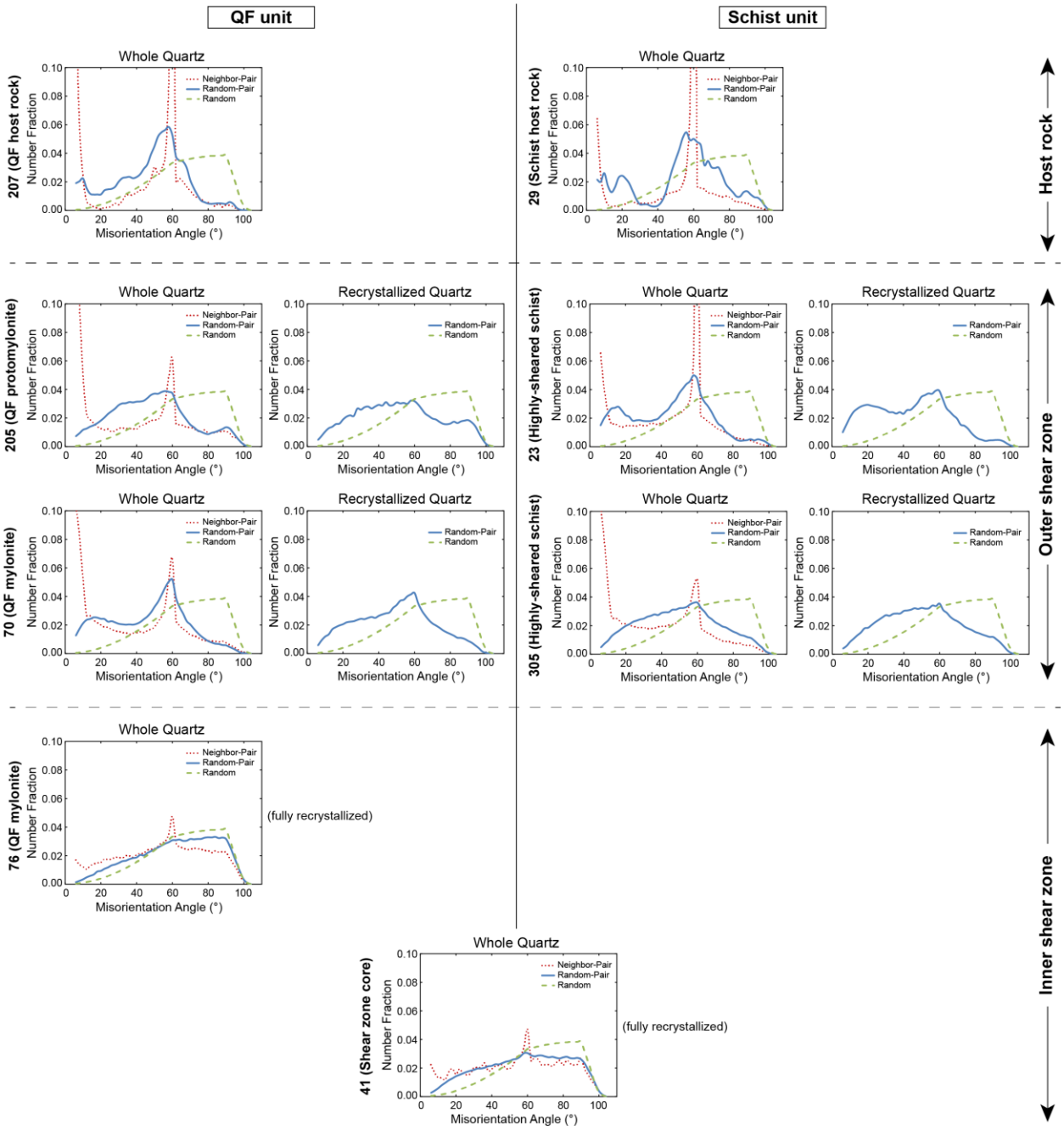

3.6.5. Fabric Strength

Fabric strength is measured by the M-index (Skemer et al., 2005), which is defined as the difference between the observed random-pair misorientation and the theoretical random misorientation, and thus indicates the degree of randomness in the crystallographic orientation fabric (0 is random and 1 is single orientation). The plots of M-index values with distance from the shear zone core exhibits a trend (Fig. 3.10) although there are variations at same distances, resulting from different rock samples or different quartz domains in the same thin section. The M-index values in both the whole and recrystallized quartz plots (Fig. 3.10) maintain intermediate values in the protomylonite, and then progressively decrease through the mylonite toward the core. The inner shear zone has low M-index values of <0.1, indicating nearly random crystallographic orientations. For the whole quartz graph (Fig. 10a), the fabric strength near the boundary between the protomylonite and the mylonite shows higher values than the host rock. In the schist unit, there is a wide range of M-index values.

Figure 3.10. Fabric strength M-index. In M-index, 0 and 1 mean random and single orientation, respectively. (a) M-index of whole quartz. (b) M-index of recrystallized quartz.

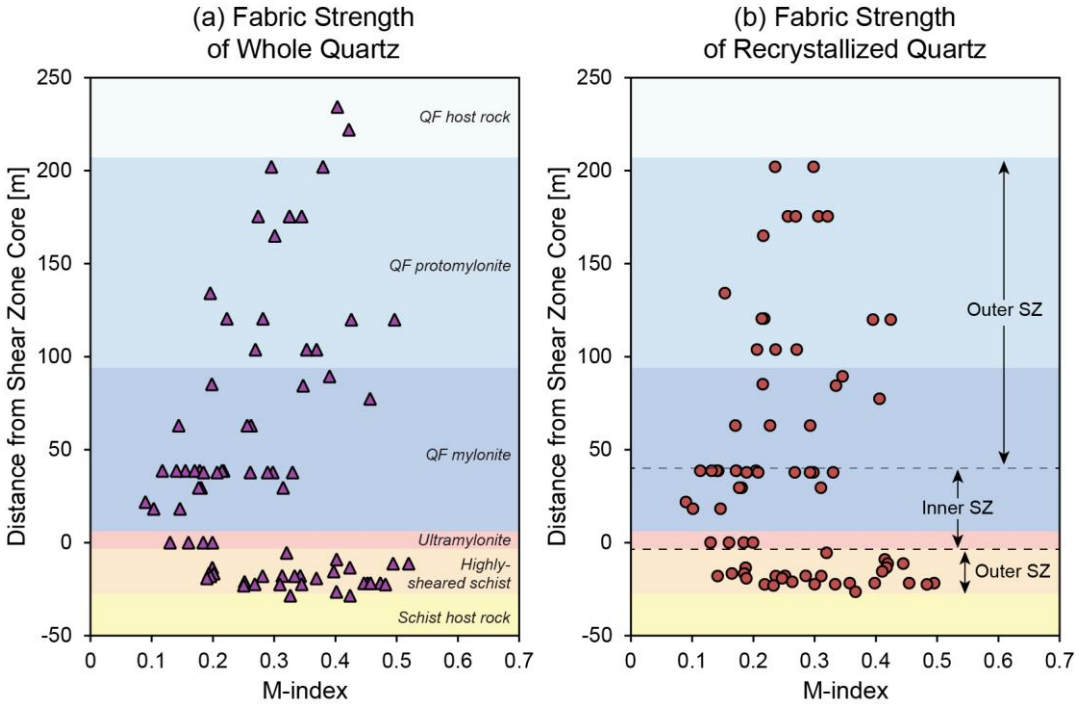

3.7. Discussion

3.7.1. Quartz CPO and Misorientation Evolution and Deformation Mechanisms

The strong clustering of c-axis in the center or between the center and the peripheral of the pole figures for the host rock quartz and parent quartz in the SCSZ (Fig. 3.8) indicates prism <a> or rhomb <a> slip active at high-temperature, predating the SCSZ development (Price et al., 2016). In the host rock misorientation plots (Fig. 3.9), the low fractions of both neighbor-pair and random-pair profiles at 10°–40° and >70° are explained by GBM recrystallization because SGR recrystallization and dislocation creep produce high and low fractions, respectively, at the low (10°–40°) and high (>70°) misorientation angles. In the outer shear zone, the single or Type I crossed girdle fabrics (Fig. 3.8), formed by spreading of recrystallized quartz c-axes from the parent quartz, indicate the activation of different dominant slip system (basal <a> slip) during SGR recrystallization. Basal <a> slip is favored at lower temperature than prism <a> or rhomb <a> slip of the host rock and SCSZ parent quartz owing to its lower critical resolved shear stress than the other two slip systems at the lower temperature (Hobbs, 1985). The SGR recrystallization in the outer shear zone is also demonstrated by the CPO patterns with similar maximum orientations between recrystallized and parent quartz (Fig. 3.8) and the misorientation profiles having higher fraction at low angles (10°–40°) for both neighbor-pair and random-pair profiles than the host rock (Fig. 3.9). Dislocation creep during the SGR recrystallization, as a dominant deformation mechanism, maintains low fraction at high angles (>70°) for both neighbor-pair and random-pair profiles (Fig. 3.9). On the other hand, the inner shear zone shows basal <a> slip with a c-axis maximum close to the foliation pole (Z) in the pole figures (Fig. 3.8) but high fraction at high angles (>70°) for both neighbor-pair and random-pair profiles (Fig. 3.9), which makes flat neighbor-pair profile and near-random random-pair profile. The flat neighbor-pair profile indicates that adjacent grains are not related by a crystallographically controlled processes (dislocation creep), and thus can result from grain-size-sensitive deformation such as grain boundary sliding (Price et al., 2016). This is supported by the near-random random-pair profile and very weak fabric strength (e.g., Fliervoet et al., 1997; Okudaira et al., 2010). Typical microstructural conditions and effect of grain boundary sliding include (1) small grain size (<10

μm), (2) equant, polygonal shapes, (3) smooth grain boundaries, (4) weakening of CPO, and (5) randomization of grain boundary misorientation axes (e.g., White, 1979; Behrmann, 1985; Jiang et al., 2000; Bestmann and Prior, 2003; Halfpenny et al., 2006). The inner shear zone (~40 m wide) with fully recrystallized quartz domains has all of these microstructural features indicative of grain boundary sliding (e.g., minimum grain size of 8 μm, minimum bulk aspect ratio of 1.1, and wide scattering of crystallographic orientation in sample 76).

Another factor to consider in determining deformation mechanism of the SCSZ is the effect of brittle co-seismic damage, which was present throughout the mylonite (Fig. 3.2b; Chapter 2), on post-seismic viscous deformation. The widespread occurrence of deformed pseudotachylyte in the inner shear zone with its highest modal percentage at the core (Fig. 3.2b) suggests different impacts of the transient brittle damage on different parts of the shear zone since co-seismic fracture density decreases away from rupture surface (deformed pseudotachylyte). Based on the division of the inner and outer shear zones and the spatial limit of damage zone, corresponding to the mylonite zone, I divide the QF unit in the SCSZ into three regions (Fig. 3.11): (a) undamaged region (protomylonite), (b) less damaged region (outer mylonite), and (c) extensively damaged region (inner mylonite and ultramylonite). Each region experiences different deformation processes during earthquake cycles. While the undamaged region deforms only viscously along with SGR recrystallization (dislocation creep) during the seismic cycle, the extensively damaged region undergoes extensive fracturing (possibly pulverization) in the co-seismic period followed by neo- and recrystallization during post-seismic stress relaxation (Trepmann et al., 2007), leading to extreme grain-size reduction and thus grain-size-sensitive flow (Fig. 3.11b). The extensive fracturing and then nucleation randomized random-pair misorientation profile in the inner shear zone, which is distinguished from the outer shear zone. The less damaged region is considered to have mixed deformation styles of the undamaged and extensively damaged regions, but exhibits dislocation creep fabrics (e.g., misorientation profile) as a dominant deformation mechanism in the inter-seismic period due to low co-seismic fracture density (Fig. 3.11b).

Figure 3.11. Deformation processes in three subdivisions during the earthquake cycle. (a) Three subdivisions indicated in the SCSZ. (b) Deformation processes of quartz represented by schematic diagrams showing co-seismic fracturing, post-seismic recrystallization and nucleation, and inter-seismic further viscous deformation. Random-pair misorientation profiles are added for indication of deformation mechanisms.

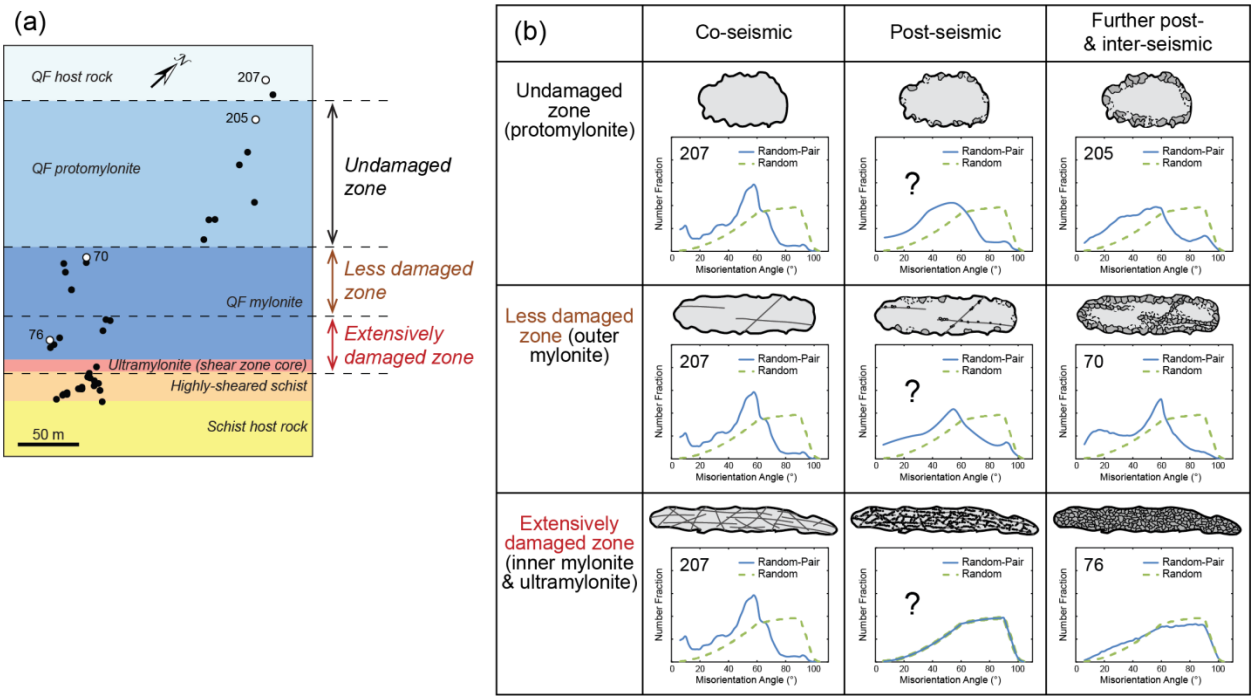

3.7.2. Comparison between Schist and QF units

The SCSZ shows the asymmetrical occurrence of deformed pseudotachylyte and quartz microfabrics (e.g., near-random random-pair profile and very low M-index values) indicative of transient high stresses around the shear zone core (Figs 3.2b and 3.10). In the QF unit, the pseudotachylyte-rich inner shear zone with very low M-index values is ~40 m wide. On the other hand, the schist unit shows only local distribution of pseudotachylyte and has very low M-index values only within the core. Such asymmetry is commonly observed around mature strike-slip faults where different rock types are juxtaposed (e.g., Dor et al., 2006; Mitchell et al., 2011; Rempe et al., 2013) since a preferred rupture propagation direction causes the greatest damage in the tensile quadrant of the rupture tip (e.g., Ben-Zion and Shi, 2005; Xu and Ben-Zion, 2017). If the strong asymmetry in development of pseudotachylyte and quartz microfabrics reflects rupture dynamics, then the right-lateral slip along the northeast-striking of the

SCSZ (Fig. 3.1) would indicate a strongly preferred rupture propagation direction through the study area toward the southwest.

3.7.3. Correlation with Shallow Crustal Levels

The detailed studies across the SCSZ presented in Chapters 2 and 3 provide a cross-sectional view of a mature strike-slip fault near the base of the seismogenic zone, which can be correlated with a fault structure at the near surface. Figure 3.12 compares the SCSZ structure in the QF unit as a strike-slip fault at 10–15 km depth to the San Andreas fault structure at the surface (based on Rempe et al., 2013). The San Andreas fault consists of a 50 cm wide fault core, a 50 m wide pulverized zone, and a 50 m wide fractured zone. Clear correlations can be drawn from the boundary between the intact granite and the San Andreas fault zone to the boundary between the QF host rock and the SCSZ as well as from the fault core to the shear zone core (Fig. 3.12). However, the outer mylonite zone (~50 m wide) of the SCSZ, or the less damaged zone, may also be comparable to the fractured zone at the surface in terms of co-seismic damage based on the fluid inclusion abundance study (Chapter 2). The inner shear zone (~40 m wide) of the SCSZ, or the extensively damaged zone (fully recrystallized mylonite and ultramylonite), can correlate with the fault core and pulverization zone at the surface (Fig. 3.12). This proposed correlation of the SCSZ structure with the modern fault observed at the surface highlights extending of a 40–50 m wide pulverization zone, within a 90–100 m wide damage zone, throughout the entire depth of the seismogenic zone in mature strike-slip faults. This in turn has important implications for transient fluid flow and rheological changes during earthquake cycles due to modification of permeability (e.g., Mitchell and Faulkner, 2008) and thermal structure (e.g., Morton et al., 2012; Ben-Zion and Sammis, 2013) within and surrounding the fault/shear zone core.

Figure 3.12. Proposed correlation between the near surface and FVT faults.

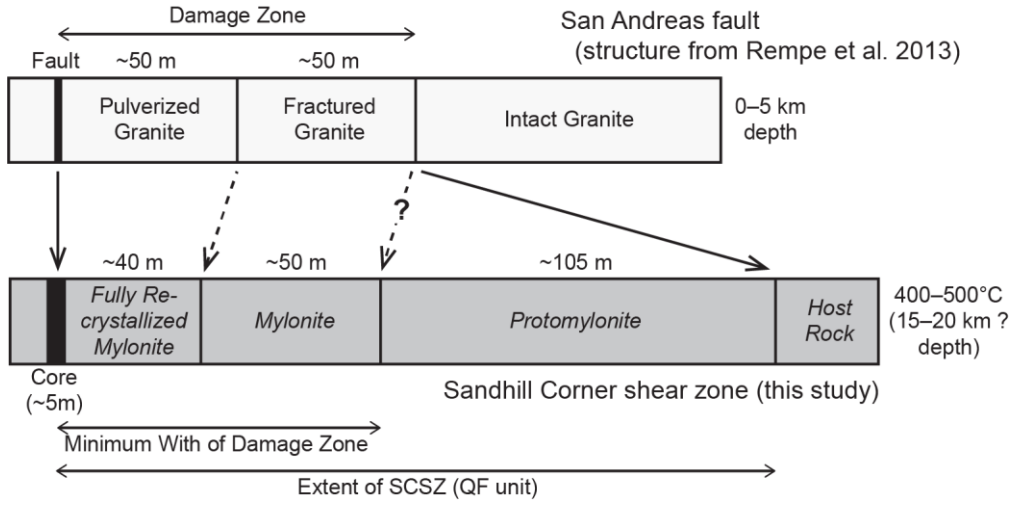

3.8. Conclusions

(1) Quartz misorientation angle distributions and fabric strength (M-index) provide valuable information for deciphering the complex deformation processes during the earthquake cycle at the FVT.

(2) Within the inner SCSZ (~40 m wide), extensive co-seismic damage (pulverization) affects dominant viscous deformation mechanism in post- and inter-seismic periods, unlike the outer shear zone showing dislocation creep fabrics. Cyclic grain-size reduction by extensive damage keeps quartz in the grain-size-sensitive regime. This micromechanical cycle facilitates long-term strain localization (weakening) and stabilization of the shear zone at FVT depths.

(3) The asymmetrical spatial extent of the deformed pseudotachylyte and quartz microfabrics indicative of transient extensive damage around the SCSZ core may suggest a strongly preferred rupture propagation direction.

CHAPTER 4

EFFECT OF CYLINDRICAL FOLDS ON SEISMIC ANISOTROPY IN THE MIDDLE AND LOWER CONTINENTAL CRUST

4.1. Chapter Abstract

Folds are one of the most common tectonic structures developed in deformed rocks, especially of orogenic belts, and should be considered to link observed seismic anisotropy with middle-to-lower crustal deformation since they rotate existing rock fabrics such as foliation, lineation, and crystal lattice-preferred orientation and, as a result, modify intrinsic seismic properties of the rocks. For instance, where the length scale of seismic waves is much larger than the scale of a fold structure, the bulk elastic stiffness of the fold can be obtained by averaging the local stiffness tensors of a representative rock rotated along the structure. New tensor formulations via the Voigt and Reuss averages, separating the bulk fold stiffness into a geometry tensor and the local rock stiffness, allow efficient and direct investigation of how fold geometry affects seismic properties. To validate the methodology, the results are compared to a precise numerical solution such as asymptotic expansion homogenization. We analytically and numerically compute the geometry tensors for different types of cylindrical folds such as sinusoidal, chevron, parabolic, box and cuspate. The bulk fold stiffness can have different symmetry from the local rock stiffness. The seismic velocity is highly sensitive to the fold orientation and morphology, and hence the seismic anisotropy of a fold depends on limb angle and hinge shape. This study contributes to not only understanding the kinematics of in-situ crustal deformation from real seismic observables owing to close relationship between fold orientation and flow kinematics, but also better interpreting mantle dynamics based on teleseismic waves passing through orogenic belts.

4.2. Chapter Introduction

Seismic anisotropy, or the dependence of seismic velocity on the direction of wave propagation and polarization, is observed throughout the earth and has been used to interpret the earth's dynamic processes. In the upper crust, seismic anisotropy due to aligned dry or fluid-filled cracks may be

indicative of principal stress orientations (e.g., O'Connell and Budiansky, 1974; Crampin, 1981; Crampin and Chastin, 2003). Upper mantle seismic anisotropy caused by deformation-induced lattice-preferred orientation (LPO; also known as crystallographic preferred orientation) of anisotropic minerals may be a direct indicator of convective flow and plate tectonics (e.g., Hess, 1964; Silver, 1996; Savage, 1999; Karato et al., 2008). Recently, seismic anisotropy in the middle and lower continental crust has been studied as a tool to assess and interpret tectonic deformation and metamorphism (e.g., Christensen and Mooney, 1995; Weiss et al., 1999; Godfrey et al., 2000; Okaya and Christensen, 2002; Mahan, 2006; Meissner et al., 2006; Tatham et al., 2008; Lloyd et al., 2009, 2011a, 2011b; Dempsey et al., 2011; Ward et al., 2012). Because microcracks are closed below about 6–10 km depth (e.g., Siegesmund et al., 1989; Kern et al., 2008), LPO of constituent minerals is considered the main source of seismic anisotropy in the middle to lower crust (e.g., Mainprice and Nicolas, 1989). LPO is typically produced by dislocation creep and/or rigid body rotation during plastic and viscous deformation (e.g., Hobbs et al., 1976, chapter 2; Nicolas and Poirier, 1976; Wenk, 1985; Mainprice and Nicolas, 1989), but may also be developed by preferential dissolution-precipitation (e.g., Bons and den Brok, 2000; Imon et al., 2004). Thus, seismic anisotropies resulting from LPO can be used to better understand the kinematics and dynamics of crustal deformation and metamorphism.

Existing methodologies for calculating rock anisotropy employ petrophysical or thin-section-based measurements on the scale of rock samples. Rock fabrics such as foliations and lineations are pervasively developed in orogenic belts and profoundly impact anisotropy. Larger-scale structures such as folds, domes and shear zones that reorient existing foliations and lineations can also profoundly affect the bulk macroscale anisotropy, and should therefore be considered when interpreting seismic anisotropy as a proxy for tectonic deformation (Okaya et al., 2018). Of the larger-scale structural geometries, folds are very common in orogenic belts and shear zones, ranging from millimeter to multi-kilometer scales. Okaya and McEvilly (2003) used synthetic seismic experiments to show that material tilt associated with macroscale folding can produce strong effects on seismic wave propagation. Bleibinhaus and Gebrande (2006) interpreted seismic anisotropy observed within the Tauern Window of the Eastern Alps to be

generated by folded foliations. Naus-Thijssen et al. (2011a) used electron backscatter diffraction (EBSD) measurements and a novel new computational method for calculating anisotropy to show that microscale folding (crenulation) of a mica-rich foliation leads to a strongly muted seismic anisotropy. These studies have shed some light on the importance of folding in the development or modification of seismic anisotropy, setting the stage for a more systematic investigation of how macroscale fold geometries influence anisotropy, which is the topic of the current study.

The treatment of a macroscale structure is dependent on its size relative to the seismic wavelength. In instances where the seismic wavelength is much larger than the structure, the analysis is greatly simplified since a single bulk stiffness tensor can be used by treating the structure as a homogeneous anisotropic medium, or "effective medium" that has the same seismic response as a complex earth volume of interest (Fig. 4.1). This treatment allows relatively simple calculation of wave speeds for fold structures with various hinge shapes and limb angles. This study uses the effective medium theory, which is valid only when the seismic wavelength (λ) is much larger than the scale (L) of heterogeneity, or anisotropic structure, $L << \lambda$ (e.g., Backus, 1962; Babuška and Cara, 1991, chapter 2; Mavko et al., 2009; Okaya et al., 2018). If a body wave from an earthquake at regional distance has a 1 km wavelength, for example, the seismic velocities in fold structures at scales up to ~100 m could be predicted by the effective medium theory. In this case, the wave is influenced by the bulk elastic properties of the fold volume containing fold limbs and hinges and its bulk anisotropy can be estimated by averaging methods of local elastic properties such as the Voigt and Reuss bounds (Voigt, 1928; Reuss, 1929). Although modern numerical homogenization methods can compute effective media with complex structures at various scales (e.g., Guedes and Kikuchi, 1990; Capdeville and Marigo, 2007; Capdeville et al., 2010a, 2010b; Guillot et al., 2010; Vel and Goupee, 2010; Naus-Thijssen et al., 2011b; Vel et al., 2016), they requires still considerably higher computational cost (time), compared to the methodology presented in this study. Here the fold volume that behaves as an effective homogeneous medium is called "structural effective medium," or EM_S.

Okaya et al. (2018) presented the concept of EM_S and structural geometries to be considered in the crust. They developed a new tensor formulation of the EM_S stiffness via the Voigt average to incorporate local rock stiffness tensors rotated by larger-scale structures, which has an algebraic separation of the EM_S stiffness into two components – the local rock stiffness and what they call a "structural geometry operator". This separation allows one to directly investigate how geometry has an impact on seismic wave velocities and anisotropies. They used sinusoidal cylindrical folds to demonstrate the effect of the macroscale structures on seismic properties. However, other common fold types such as chevron and parabolic should be considered, and how the shape of fold hinge affects seismic anisotropy need to be investigated to delimit the variations of seismic properties depending on fold morphology. In addition, a comparative examination between homogenization techniques for fold EM_S is required since different homogenization may result in a significant variation of predicted seismic velocity.

In this study, we compute the structural geometry operators of a full family of single-layered cylindrical folds (e.g., Fig. 4.1a), including sinusoidal, chevron, parabolic, box and cuspate, via the Voigt and Reuss averages, and systematically investigate their influence on seismic anisotropy as functions of both limb angle and fold type. The results are also compared to one of the modern numerical homogenization methods, asymptotic expansion homogenization (e.g., Vel and Goupee, 2010; Naus-Thijssen et al., 2011b; Vel et al., 2016). This comparison provides the validation and usefulness of my methodology in studying how the morphological change of fold consisting of a rock affects the magnitude and symmetry of seismic anisotropy with markedly reduced computational cost. The estimation of the rock stiffness at hand-specimen scale has been well studied via an ultrasonic pulse transmission technique (e.g., Godfrey et al., 2000) or homogenization from EBSD-based LPO and single-crystal elastic parameters (e.g., Lloyd and Kendall, 2005). Thus, we focus on how larger-scale fold geometries modify the seismic properties of a given rock that makes up single-layered folds. We then discuss how the EM_S can be expanded to multi-layered folds (e.g., Fig. 4.1c).

Figure 4.1. Schematic diagrams illustrating 3-D cylindrical folds and the concept of effective medium. (a) A single-layer, periodic, cylindrical folds with a scale of L, which is much smaller than the wavelength (λ) of seismic waves. One spatial cycle of the fold structure can be chosen as an effective medium. (b) Effective medium of the fold shown in (a). This can be represented by the bulk stiffness and density of the fold without describing structural details and exhibits the same seismic response as the folds in (a). We call this "structural effective medium," or EM_S. (c) A multi-layer, periodic, cylindrical folds with a scale of L ($<<\lambda$). Representative rock of each layer can have different seismic properties. A single spatial cycle of the multi-layered fold can be selected as EM_S.

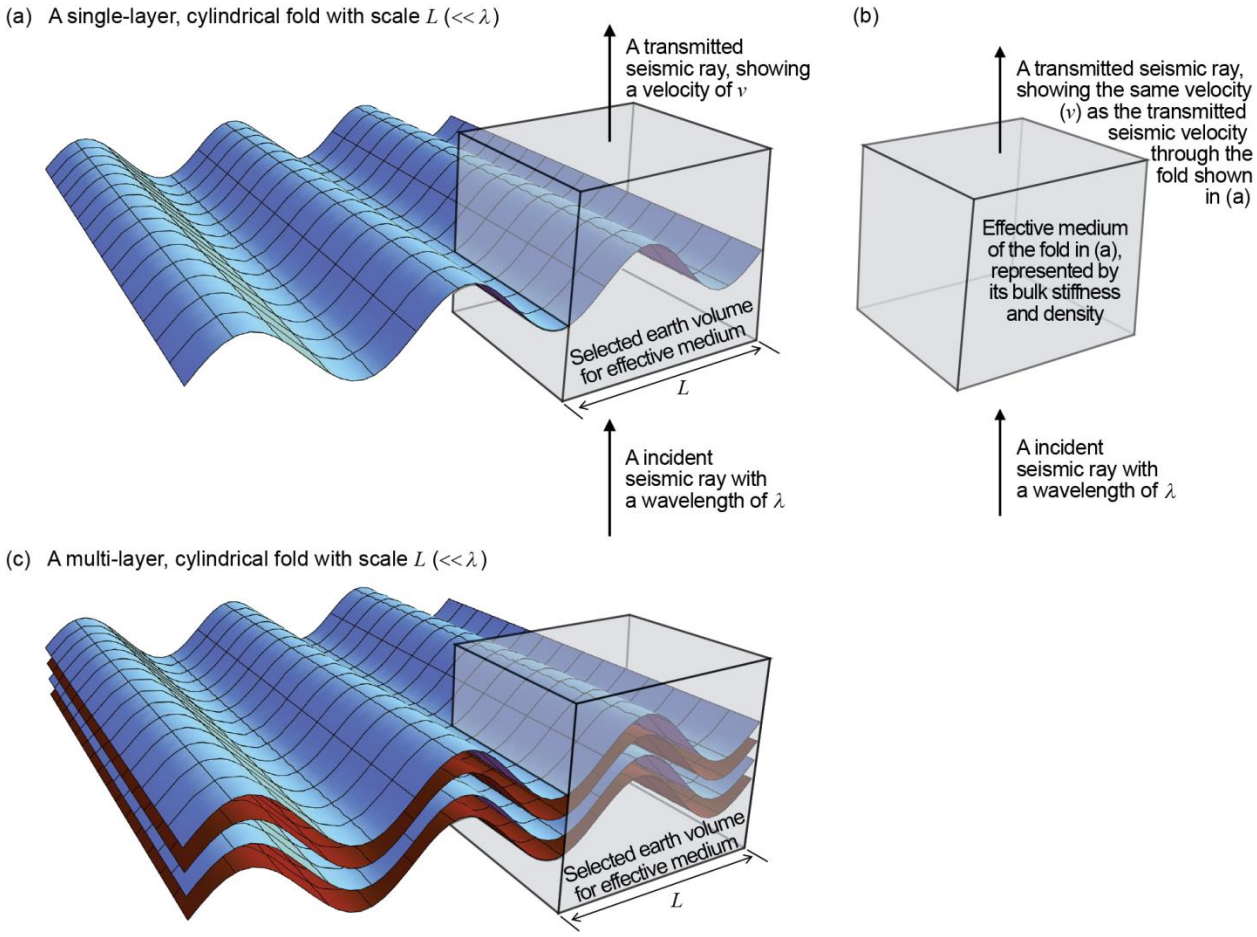

4.3. Methods

We first describe mathematical expressions of cylindrical fold geometries, and then briefly review homogenization techniques of rock elastic symmetry rotated along the folds for the EM_S. After recalling the algebraic separation of geometry from rock stiffness presented by Okaya et al. (2018), we calculate structural geometry operators of all the cylindrical folds to investigate the solely geometrical effect on seismic anisotropy. For simplicity, we employ periodic and symmetric cylindrical folds with

horizontal hinge lines and adopt one full spatial cycle (wavelength) of each fold as the representative volume (Figs 4.2b, 4.2c and 4.2d). In the case of a general cylindrical fold (e.g., Fig. 4.2a), e.g., periodic asymmetric folds, the EM_S can be computed in the same way as this section, which will be discussed in section 4.7.2.

Figure 4.2. Nomenclature of a general cylindrical fold and reference systems used in this study. Mathematical functions describe periodic and symmetric fold geometries. (a) A general cylindrical fold with horizontal hinge line and its geographical frame (*x*-*y*-*z*). Modified from Hobbs et al. (1976, Fig. 4.4.2). (b) Reference system for one spatial cycle of a symmetric sinusoidal fold in the profile plane. (c) Reference system for one spatial cycle of symmetric chevron, parabolic, and box folds in the profile plane. (d) Reference system for one spatial cycle of a symmetric cuspate fold in the profile plane.

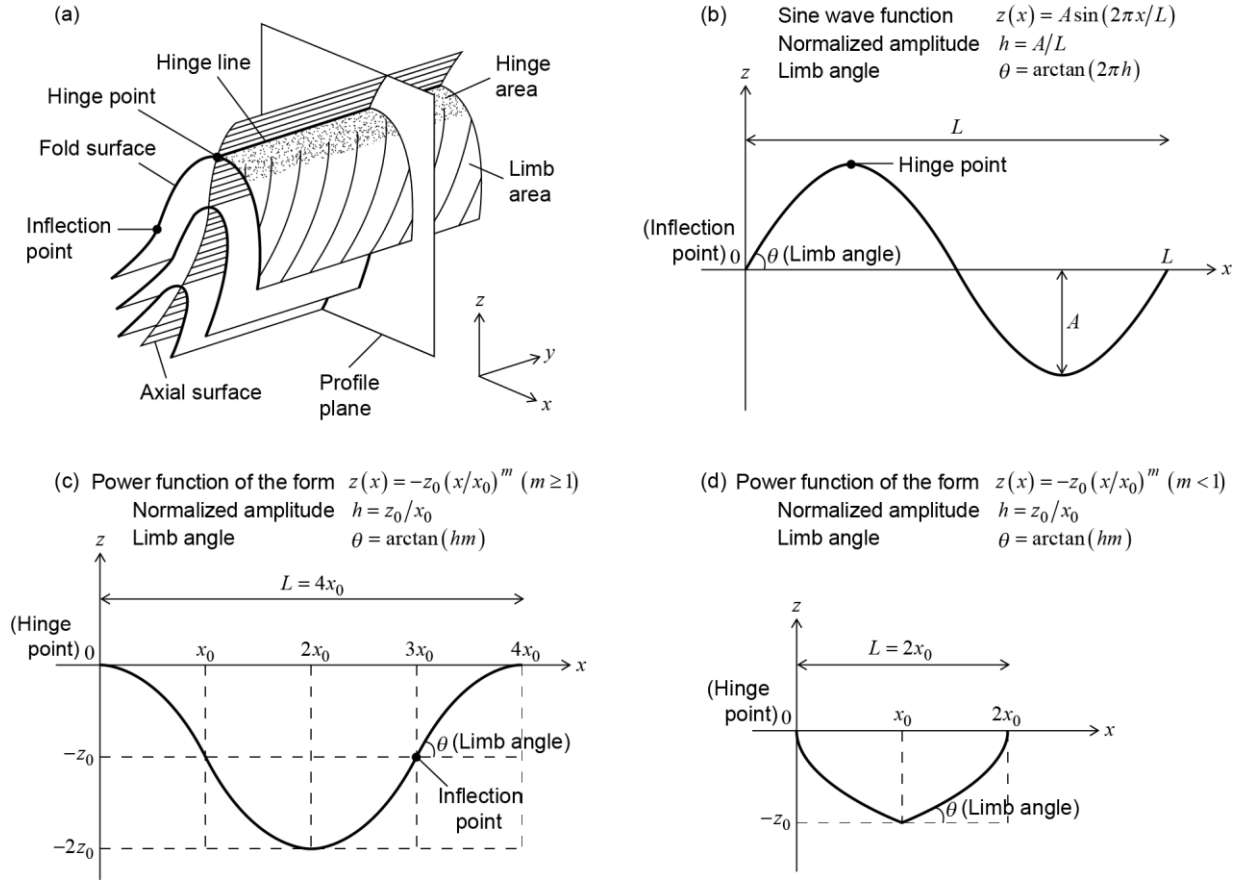

4.3.1. Mathematical Expression of Fold Geometries

Cylindrical fold geometries with a straight hinge line can be mathematically expressed in the fold profile plane perpendicular to the hinge line (Fig. 4.2a). In general, the selected reference system for describing fold geometries has the tangent line to the profile curve of a fold surface at a hinge point as *x* axis and its normal line through the hinge point as *z* axis (Figs 4.2c and 4.2d). In the case of sinusoidal folds, the coordinate origin is assumed to be at an inflection point for mathematical convenience (Fig. 4.2b). The midpoint of the fold surface profile between both hinges is chosen as the coordinate origin in the case of double-hinge folds, or box folds.

For sinusoidal fold geometry, the sine wave function is given by

$$z(x) = A\sin\left(\frac{2\pi x}{L}\right) \tag{1}$$

where A and L are the amplitude and wavelength, respectively, of the sinusoidal fold (Fig. 4.2b). The fold amplitude can be described in terms of the limb angle (θ) defined as the acute angle between the x axis and a tangent line to an inflection point (Fig. 4.2b), and θ is related to the aspect ratio, or normalized amplitude h (= A / L):

$$\theta = \arctan(2\pi h) \tag{2}$$

Fig. 4.3c illustrates two spatial cycles of the sinusoidal fold geometry when θ = 45°.

To depict other fold profile geometries including chevron, parabolic and box folds, a power function is used (Bastida et al., 1999):

$$z(x) = -z_0\left(\frac{x}{x_0}\right)^m; \qquad x \in [0, x_0] \tag{3}$$

where z_0 is the fold amplitude. Equation (3) is defined within the interval [0, x_0]; m, x_0 and z_0 are positive numbers. In order to represent one-complete fold cycle, modifications of equation (3) are used for other intervals:

$$z(x) = z_0\left(\frac{-x + 2x_0}{x_0}\right)^m - 2z_0; \qquad x \in [x_0, 2x_0] \tag{4}$$

$$z(x) = z_0 \left(\frac{x - 2x_0}{x_0} \right)^m - 2z_0; \qquad x \in [2x_0, 3x_0] \tag{5}$$

$$z(x) = -z_0 \left(\frac{-x + 4x_0}{x_0} \right)^m; \qquad x \in [3x_0, 4x_0] \tag{6}$$

The set of equations (3), (4), (5) and (6) describes a full cycle of the cylindrical fold profile within the interval [0, $4x_0$] and its wavelength (L) is $4x_0$ (Fig. 4.2c). Various fold morphologies can be obtained by two parameters: the exponent (m) and the normalized height or amplitude ($h = z_0 / x_0$). Common fold types are characterized by the following values of m: (1) $m = 1$, chevron folds; (2) $m = 2 / (\pi - 2) \approx 1.75$, fit of sinusoidal folds; (3) $m = 2$, parabolic folds; (4) $m > 2$, box folds (or double-hinge folds; here the word 'box' is used to describe double-hinge folds although a perfect box fold requires $m \rightarrow \infty$) (Bastida et al., 1999). The fold limb angle (θ) measured at the inflection point is related to the normalized amplitude (h):

$$\theta = \arctan(hm) \tag{7}$$

Figs 4.3b, 4.3d and 4.3e illustrate the geometry of chevron, parabolic and box folds, respectively, when $\theta = 45°$.

Cuspate folds are expressed using equation (3) within [0, x_0] and the following equation within the interval [x_0, $2x_0$]:

$$z(x) = -z_0 \left(\frac{-x + 2x_0}{x_0} \right)^m; \qquad x \in [x_0, 2x_0] \tag{8}$$

When $m < 1$, equations (3) and (8) describe one spatial cycle of a cuspate-lobate fold and its wavelength (L) is $2x_0$ (Fig. 4.2d). The limb angle (θ) is measured at the lowest point of a lobe and its relationship to the normalized amplitude (h) is the same as equation (7). An example of cuspate (cuspate-lobate) shapes is illustrated in Fig. 4.3a.

Figure 4.3. The five types of fold geometries in the profile plane at the same length scale ($2L$) and limb angle (θ = 45°). They show two cycles and are presented in order of decreasing hinge curvature. Folds with sharper hinges (e.g., cuspate fold) have a larger ratio of height to wavelength. (a) Cuspate fold profile with m = 0.5. (b) Chevron fold profile. (c) Sinusoidal fold profile. The same geometry can be described by power functions with $m = 2 / (\pi - 2) \approx 1.75$. When compared with the parabolic shape, the sinusoidal has slightly larger curvature in the hinge area that can be difficult to visually distinguish. (d) Parabolic fold profile. (e) Box fold profile with m = 3.

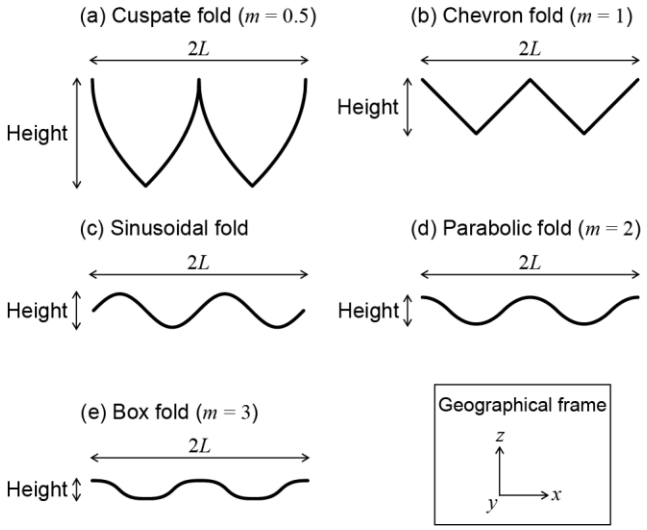

4.3.2. Setup of Tensorial Computation for Fold Structural Effective Medium (EM_S): Rotation of Rock Elastic Symmetry

The phase velocities of monochromatic plane waves in an anisotropic homogeneous elastic medium can be obtained using the Christoffel equation (Christoffel, 1877):

$$\left(C_{ijkl} n_j n_l - \rho v^2 \delta_{ik}\right) p_k = 0 \tag{9}$$

where C_{ijkl} is the fourth-order elastic stiffness tensor, n_j is the unit vector in the propagation direction, ρ is the mass density, v is the phase velocity, δ_{ik} is the Kronecker delta, p_k is the amplitude vector defining the polarization of particle motion (displacement direction), and the indices ($ijkl$) range from one to three. Three body waves, or one quasi-longitudinal (qV_P) and the two quasi-shear wave velocities (qV_{SH} and qV_{SV}) can be identified based on their orthogonal polarization (or displacement) vectors with respect to the external x-y-z coordinate frame. The body waves may also be classified based on their relative velocities as qV_P, qV_{S1} and qV_{S2} with $qV_P > qV_{S1} > qV_{S2}$ irrespective of their polarization. qV_{S1} and qV_{S2} are

used for seismic anisotropy calculation because they are not dependent on the reference frame. If rocks are folded and the fold structure is modeled as an EM_S, then seismic wave velocities depend on the bulk elastic stiffness tensor (**C***) and bulk density (ρ*) of the fold EM_S. Below we describe how to compute the EM_S stiffness of a fold structure from the stiffness tensors of its constituent rocks.

In a cylindrical fold, the elastic symmetry axes (denoted by *a*-*b*-*c*) of the rock are rotated along the fold surface profile relative to the geographical frame (denoted by *x*-*y*-*z*) as shown in Fig. 4.4a. For instance, at point 1, the rock symmetry axes form a positive angle of ϕ with respect to the geographical axes, and at point 2, the *a*-*b*-*c* rock axes are oriented at a negative angle of ϕ with the *x*-*y*-*z* frame (Fig. 4.4b). Thus, the angle (ϕ) between the *a* and *x* axes is a function of position *x* and defines the rotation of the rock symmetry axes from the geographical frame:

$$\phi(x) = \arctan\left(\frac{dz(x)}{dx}\right); \qquad -90° < \phi < 90° \tag{10}$$

where $z(x)$ can be any form of the fold equations in section 4.3.1. The angular relation between the two axis systems is described by the direction cosine matrix (***a***):

$$a_{ij}(x, y, z) = a_{ij}(x) = \begin{bmatrix} \cos\phi(x) & 0 & -\sin\phi(x) \\ 0 & 1 & 0 \\ \sin\phi(x) & 0 & \cos\phi(x) \end{bmatrix} \tag{11}$$

The elastic stiffness tensor **C′** of each rotated rock at each position *x* in the geographical frame can be obtained from its elastic stiffness tensor **C** in the symmetry axes using fourth-order tensor transformation, which employs the direction cosines of equation (11) (e.g., Nye, 1985, chapter 8):

$$C'_{ijkl}(x, y, z) = \{a_{im}a_{jn}a_{ko}a_{lp}\}_{(x,y,z)}C_{mnop}(x, y, z) \tag{12}$$

where $C'_{ijkl}(x, y, z)$ is the rotated stiffness tensor at location (x, y, z) in the geographical frame, $C_{mnop}(x, y, z)$ is the local rock stiffness tensor at location (x, y, z) in the rock symmetry frame, and the Einstein summation convention is used wherein a repeated index implies summation over the range of the index. A single EM_S stiffness tensor of a fold structure (C^*_{ijkl}) can be computed by averaging, or homogenizing, the stiffness tensors of the rotated rocks (C'_{ijkl}) in the structure volume.

Figure 4.4. Schematic representation showing the relationship between the elastic symmetry axes (*a*-*b*-*c*) of local rocks and the geographical frame (*x*-*y*-*z*) of the fold EM_S. (a) The rock symmetry axes rotate on the *b* axis, which is perpendicular to the *a*-*c* and *x*-*z* axes, along the fold surface profile relative to the geographical frame. *A* and *L* are the fold amplitude and wavelength, respectively. θ is the fold limb angle measured at the fold inflection point. (b) The angle (ϕ) between two reference systems is measured between the *a* and *x* axes. Their relationships at points 1 and 2 in (a) are displayed as examples.

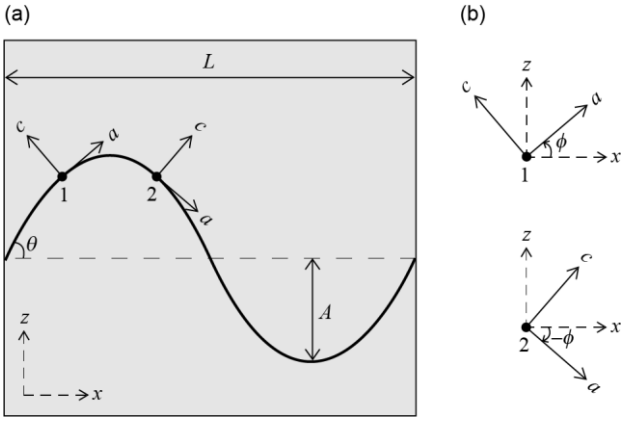

4.3.3. Homogenization Techniques for Fold EM_S

The simplest averaging techniques are the Voigt (1928) and Reuss (1929) estimates, which use only modal volumes and stiffness tensors of the constituent materials. They provide upper and lower bounds for the bulk stiffness by assuming iso-strain and iso-stress throughout the volume, respectively. Due to heterogeneity, however, rocks or structures generally do not have uniform stress and strain fields. Although the arithmetic mean (Hill, 1952) and the geometric mean (Matthies and Humbert, 1993) of the two bounds have been proposed, they lack physical justification by not taking into account elastic interactions between elements. Recently, a precise numerical solution for the bulk elastic properties via asymptotic expansion homogenization has been developed (e.g., Vel and Goupee, 2010; Naus-Thijssen et al., 2011b; Vel et al., 2016). Since the advanced numerical homogenization considers the mechanical interactions between the elastic elements in the volume to provide a full-field solution for the heterogeneous stresses and strains, it allows more precise analysis of bulk stiffness at various scales. Only the Voigt and Reuss methods allow a separation of structural geometry operator from rock stiffness tensor.

The asymptotic expansion homogenization, completely different from the Voigt and Reuss approaches, will be used to validate my methodology by comparing fold EM_S and seismic wave velocities.

4.3.3.1. Voigt Averaging of Elastic Stiffness

The Voigt method averages the rotated stiffness tensors (C'_{ijkl}) at every location (x, y, z) in the effective medium volume (V) to obtain the fold EM_S stiffness tensor (C^{*Voigt}_{ijkl}):

$$\begin{aligned} C^{*Voigt}_{ijkl} &= \frac{1}{V}\int C'_{ijkl}(x,y,z)dV \\ &= \frac{1}{V}\int \{a_{im}a_{jn}a_{ko}a_{lp}\}_{(x,y,z)} C_{mnop}(x,y,z)dV \end{aligned} \tag{13}$$

This Voigt method will be first considered to compute structural geometry operators of folds and their seismic anisotropies owing to its simplicity.

4.3.3.2. Reuss Averaging of Elastic Stiffness

The Reuss bound of the bulk stiffness (C^{*Reuss}_{ijkl}) is given by inverting the Reuss bulk compliance (S^{*Reuss}_{ijkl}) which is calculated by averaging local compliances of a fold structure. A compliance tensor (S'_{ijkl}) rotated into the geographical frame is obtained from a local rock compliance tensor (S_{mnop}) at every location (x, y, z) using fourth-order tensor transformation (e.g., Nye, 1985, chapter 8):

$$S'_{ijkl}(x,y,z) = \{a_{im}a_{jn}a_{ko}a_{lp}\}_{(x,y,z)} S_{mnop}(x,y,z) \tag{14}$$

The Reuss bulk compliance (S^{*Reuss}_{ijkl}) is given by

$$\begin{aligned} S^{*Reuss}_{ijkl} &= \frac{1}{V}\int S'_{ijkl}(x,y,z)dV \\ &= \frac{1}{V}\int \{a_{im}a_{jn}a_{ko}a_{lp}\}_{(x,y,z)} S_{mnop}(x,y,z)dV \end{aligned} \tag{15}$$

The Reuss method to compute fold geometry tensors and its results will be presented and compared to the Voigt bounds in section 4.7.1.

4.3.3.3. Asymptotic Expansion Homogenization

Asymptotic expansion homogenization (AEH), which has a strong mathematical basis (Bensoussan et al., 1978), explicitly accounts for elastic interactions in heterogeneous materials and has been extensively validated and used to numerically homogenize heterogeneous material properties in engineering and geology (e.g., Guedes and Kikuchi, 1990; Fish and Wagiman, 1992; Vel and Goupee, 2010; Naus-Thijssen et al., 2011a, 2011b; Vel et al., 2016).

When a fold is subjected to deformation, the resulting internal stresses and strains will be heterogeneously distributed due to the spatial variation of rotated rock stiffness tensors in the fold. In the AEH method, the heterogeneous distribution of stresses and strains are resolved using 18 location-dependent proportionality constants ($\chi_i^{kl}(x, y, z)$; also known as characteristic functions) that map the 6 average strains to the 3 components of the displacement fluctuations at a point. The 3-D elastic equilibrium equations in conjunction with the constitutive equations for anisotropic materials yield a system of partial differential equations for the characteristic functions that are solved using the finite element method. The AEH EM_S stiffness tensor (C_{ijkl}^{*AEH}) is obtained using the characteristic functions and the rotated elastic stiffness tensors through volume or area (Y) integration as follows (seeVel and Goupee, 2010 and Naus-Thijssen et al. (2011b) for details):

$$C_{ijkl}^{*AEH} = \frac{1}{|Y|}\int_Y \left(C'_{ijkl} + C'_{ijpq}\left(\nabla \boldsymbol{\chi}^{kl}\right)_{pq} \right) dY \tag{16}$$

The expression for the AEH EM_S stiffness tensor contains two terms in the integrand. The first term corresponds to the traditional Voigt average. The second term, involving the 18 characteristic functions, captures the elastic interactions between the heterogeneities. As such, the AEH method provides a precise solution for the 3-D EM_S stiffness tensor (C_{ijkl}^{*AEH}). Since the AEH method uses the finite element method to calculate the characteristic functions, it is computationally more expensive than traditional averaging schemes, such as the Voigt and the Reuss, and it does not yield a closed-form solution for the EM_S stiffness tensor. We use graphical user interface software, named "Elastic and Seismic Properties (ESP)

Toolbox", that has been developed to calculate bulk elastic properties and plot seismic wave speeds using equations (16) and (9). The software package and manual are currently available for download at the following address: http://umaine.edu/mecheng/faculty-and-staff/senthil-vel/software/ESP_Toolbox/. The AEH results for sinusoidal folds will be used to validate the Voigt and Reuss methods by comparing to their EM_S and seismic properties in sections 4.4 and 4.7.1, and below is the detailed design of the AEH method.

To numerically calculate the bulk fold stiffness through the AEH method, we first discretize the analysis domain full of a sinusoidal fold (Fig. 4.5). The spatial increments in the x and z directions (Δx and Δz, respectively) are

$$\Delta x = \frac{L}{Nx}; \qquad \Delta z = \frac{H}{Nz} \tag{17}$$

where L and H are the length (= fold wavelength) and height of the analysis domain, respectively, and Nx and Nz are the number of analysis (or sampling) points in each direction. Using more points will yield more accurate bulk EM_S (here 500 points are adopted for Nx and Nz). The discrete x and z coordinates of the points (x_p and z_p, respectively) are as follows:

$$x_p = (n-1)\Delta x + \frac{\Delta x}{2}; \qquad 1 \le n \le Nx \tag{18}$$

$$z_p = (n-1)\Delta z + \frac{\Delta z}{2}; \qquad 1 \le n \le Nz \tag{19}$$

The next step is to determine the orientation of the rock elastic symmetry axes (a and c in Fig. 4.5a) along the fold surface profile relative to the analysis (or geographical) frame (x and z in Fig. 4.5a) at each sampling point. As shown in section 4.3.2, the rotation angle (ϕ) is a function of x or x_p in the idealized cylindrical fold. In the case of sinusoidal folds, from equations (1), (2) and (10),

$$\phi(x_p) = \arctan\left[\tan\theta \cos\left(\frac{2\pi x_p}{L}\right)\right] \tag{20}$$

In Fig. 4.5a, three rotation angles at their sampling points are illustrates as examples (they have the same ϕ owing to their same x_p). Finally, the AEH stiffness tensor for sinusoidal fold with a specific limb angle

(θ) can be obtained using equation (16) and the rotated Haast schist stiffness (**C′**) at each point that is calculated from the Haast schist stiffness ($\mathbf{C}^{\mathbf{rep}}$) and the rotation angle (ϕ). For the purpose of using the ESP Toolbox, we also define the Euler angles with Bunge convention corresponding to ϕ, which is {-π/2, ϕ, π/2}. Fig. 4.51b shows a finite element mesh used to numerically calculate the AEH stiffness of the sinusoidal folds by the ESP Toolbox, which adopts six-noded triangular elements with quadratic shape functions for accurate results (Cook et al., 2002). To get all the AEH fold stiffness tensors for limb angles ranging from 0° to 90°, the numerical AEH analysis described above is repeated for each limb angle.

Figure 4.5. Design of the asymptotic expansion homogenization (AEH) analysis combined with finite element for the EM_S of a single-layered sinusoidal fold. (a) Discretization of the analysis domain and calculation of the rotation angle (ϕ) of the rock elastic symmetry axes (*a*-*b*-*c*) at each discretized coordinate (x_p, z_p) relative to the analysis frame (*x*-*y*-*z*). The sinusoidal fold trace (dashed curve) is provided for illustrative purposes. (b) Finite element mesh used to calculate the AEH stiffness for the sinusoidal fold domain in (a).

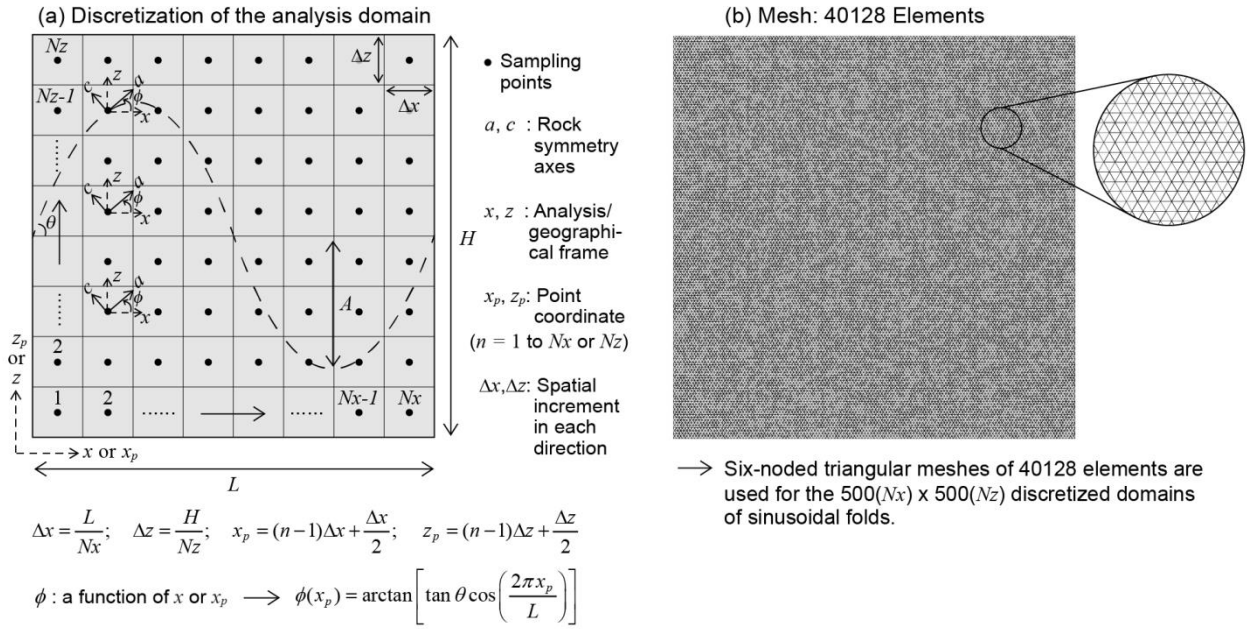

4.3.4. Separation of Fold EM_S into Structural Geometry Operator (SGO) and Rock Stiffness via the Voigt Method

In situations where the rock type within a fold structure is uniform or the variation is at a spatial scale much finer than the wavelength dimensions of seismic waves, the local rock stiffness tensor ($C_{mnop}(x, y, z)$) can be replaced by a representative rock stiffness tensor (C^{rep}_{mnop}) throughout the fold volume (V). In such cases, the C^{rep}_{mnop} can be factored out of the integral in equation (13) since it is assumed to be the same at every location (x, y, z) within the fold:

$$C^{*Voigt}_{ijkl} = \left[\frac{1}{V}\int \{a_{im}a_{jn}a_{ko}a_{lp}\}_{(x,y,z)}\,dV\right] C^{rep}_{mnop} \tag{21}$$

By introducing a structural geometry operator (**SGO**), the Voigt EM_S stiffness tensor ($\mathbf{C*^{Voigt}}$) in equation (21) can be expressed as the product of the **SGO** and the representative rock stiffness tensor ($\mathbf{C^{rep}}$):

$$\mathbf{C*^{Voigt}} = \mathbf{SGO^{Voigt}}\,\mathbf{C^{rep}} \tag{22}$$

where the superscript **Voigt** in $\mathbf{SGO^{Voigt}}$ denotes the structural geometry operator for stiffness in the Voigt calculation, which will be distinguished from $\mathbf{SGO^{Reuss}}$ for compliance in the Reuss method (see section 4.7.1). The **SGO** in equation (22) can be viewed as an operator that replaces the need to reorient $\mathbf{C^{rep}}$ at each location of the fold and carry out the volume averaging of the reoriented stiffness tensors. The **SGO** is solely contingent on the fold geometry and independent of the rock stiffness tensor. Therefore, the separation of the EM_S stiffness into **SGO** and $\mathbf{C^{rep}}$ allows for a direct investigation of structural geometry effects on seismic wave velocities.

Using matrix-vector operations, equation (22) becomes

$$[C*^{Voigt}]_{21\times1} = [SGO^{Voigt}]_{21\times21}[C^{rep}]_{21\times1} \tag{23}$$

where the subscripts denote the size of the arrays and matrices, and $[C*^{Voigt}]_{21\times1}$ and $[C^{rep}]_{21\times1}$ are the fold EM_S stiffnesses and the representative rock elastic constants, respectively, arranged as 21×1 column arrays. The elements of the 21×21 **SGO** matrix in equation (23) are obtained through a volumetric averaging of the products of the direction cosines in equation (21). $[SGO^{Voigt}]_{21\times21}$ in generalized form has

441 terms. The full 21-element structure is valid for the lowest material symmetry (triclinic). An increase in rock symmetry of $\mathbf{C}^{\mathbf{rep}}$ will lower the number of non-zero elements and thus simplify the **SGO**. We illustrate the simplest case of the fold **SGO** in the following section by assuming hexagonal (equivalent to transversely isotropic) symmetry rock tensor in $\mathbf{C}^{\mathbf{rep}}$.

4.3.5. Calculation of the $\mathbf{SGO}^{\mathbf{Voigt}}$ for Folds made of Hexagonally Symmetric Rocks

Even though we can theoretically acquire the **SGO** of any geometry that can be expressed mathematically, it is possible to obtain the **SGO** analytically only for fold geometries defined by elementary functions. In the case of folds that can be described only through more complex functions, as is the case for box and cuspate folds, the **SGO** can be computed numerically by discretizing the representative volume into smaller volume elements and subsequently averaging the local rotation tensor at the element centers. The integrations required to obtain the **SGO** matrices were performed symbolically using *Mathematica* (Wolfram Research, 2012).

Since single-layered 3-D cylindrical fold morphology is defined by one-dimensional mathematical functions in the profile plane (see section 4.3.1), the volumetric averaging in equation (21) is simplified to one-dimensional integrations:

$$C_{ijkl}^{*Voigt} = \left[\frac{1}{L} \int_0^L \{ a_{im} a_{jn} a_{ko} a_{lp} \}_{(x)} \, dx \right] C_{mnop}^{rep} \tag{24}$$

It is possible to obtain closed-form expressions for the components of the **SGO** matrix for simple fold geometries by performing the integrations in equation (24) analytically. If the representative rock in a fold is assumed to have hexagonal symmetry with the *c* axis being the symmetry axis, the stiffness tensor of the rock ($\mathbf{C}^{\mathbf{rep}}$) has five independent components (e.g., Nye, 1985, chapter 8). However, due to tensor transformation, the resulting fold EM_S stiffness ($\mathbf{C}^{*\mathbf{Voigt}}$) exhibits orthorhombic symmetry with 9 components. This relationship can be written in column vector forms as follows:

$$\begin{Bmatrix} C_{11}^{*Voigt} \\ C_{12}^{*Voigt} \\ C_{13}^{*Voigt} \\ C_{22}^{*Voigt} \\ C_{23}^{*Voigt} \\ C_{33}^{*Voigt} \\ C_{44}^{*Voigt} \\ C_{55}^{*Voigt} \\ C_{66}^{*Voigt} \end{Bmatrix} = [SGO^{Voigt}] \begin{Bmatrix} C_{11}^{rep} \\ C_{13}^{rep} \\ C_{33}^{rep} \\ C_{44}^{rep} \\ C_{66}^{rep} \end{Bmatrix} \tag{25}$$

In equation (25), the component of the stiffness tensors are expressed using the Voigt contracted notation (i.e., $C_{ijkl} \rightarrow C_{\alpha\beta}$ where α and β range from one to six) (e.g., Nye, 1985, chapter 8). The **SGO** matrix is of dimension 9×5.

For sinusoidal folds defined by the sine wave function (equation (1)), the **SGO** matrix is

$$[SGO^{Voigt}]_{sinusoidal} = \begin{bmatrix} \frac{B+1}{D^3} & \frac{2B}{D^3} & \frac{B(2D-3)+D-1}{D^3} & \frac{4B}{D^3} & 0 \\ \frac{1}{D} & 1-\frac{1}{D} & 0 & 0 & -\frac{2}{D} \\ \frac{B}{D^3} & 1-\frac{2B}{D^3} & \frac{B}{D^3} & -\frac{4B}{D^3} & 0 \\ 1 & 0 & 0 & 0 & 0 \\ 1-\frac{1}{D} & \frac{1}{D} & 0 & 0 & -2+\frac{2}{D} \\ \frac{B(2D-3)+D-1}{D^3} & \frac{2B}{D^3} & \frac{B+1}{D^3} & \frac{4B}{D^3} & 0 \\ 0 & 0 & 0 & \frac{1}{D} & 1-\frac{1}{D} \\ \frac{B}{D^3} & -\frac{2B}{D^3} & \frac{B}{D^3} & 1-\frac{4B}{D^3} & 0 \\ 0 & 0 & 0 & 1-\frac{1}{D} & \frac{1}{D} \end{bmatrix} \tag{26}$$

where B and D are non-dimensional parameters defined as $B = (1/2)\tan^2\theta$ and $D = \sqrt{1+\tan^2\theta}$, and θ is the limb angle.

The **SGO** matrix of chevron folds, which are described by the power function with m = 1 (equations (3), (4), (5) and (6)), is as follows:

$$[SGO^{Voigt}]_{chevron} = \begin{bmatrix} c^4 & 2c^2s^2 & s^4 & 4c^2s^2 & 0 \\ c^2 & s^2 & 0 & 0 & -2c^2 \\ c^2s^2 & c^4+s^4 & c^2s^2 & -4c^2s^2 & 0 \\ 1 & 0 & 0 & 0 & 0 \\ s^2 & c^2 & 0 & 0 & -2s^2 \\ s^4 & 2c^2s^2 & c^4 & 4c^2s^2 & 0 \\ 0 & 0 & 0 & c^2 & s^2 \\ c^2s^2 & -2c^2s^2 & c^2s^2 & (c^2-s^2)^2 & 0 \\ 0 & 0 & 0 & s^2 & c^2 \end{bmatrix} \tag{27}$$

where c and s are non-dimensional parameters defined as $c = \cos\theta$ and $s = \sin\theta$, and θ is the limb angle.

In the case of parabolic folds described by the power function with $m = 2$ (equations (3), (4), (5) and (6)), the **SGO** matrix is given by

$$[SGO^{Voigt}]_{parabolic} = \begin{bmatrix} \frac{c(cs+\theta)}{2s} & \frac{c(-cs+\theta)}{s} & 1+\frac{c(cs-3\theta)}{2s} & \frac{2c(-cs+\theta)}{s} & 0 \\ \frac{c\theta}{s} & 1-\frac{c\theta}{s} & 0 & 0 & -\frac{2c\theta}{s} \\ \frac{c(-cs+\theta)}{2s} & 1+\frac{c(cs-\theta)}{s} & \frac{c(-cs+\theta)}{2s} & \frac{2c(cs-\theta)}{s} & 0 \\ 1 & 0 & 0 & 0 & 0 \\ 1-\frac{c\theta}{s} & \frac{c\theta}{s} & 0 & 0 & -2+\frac{2c\theta}{s} \\ 1+\frac{c(cs-3\theta)}{2s} & \frac{c(-cs+\theta)}{s} & \frac{c(cs+\theta)}{2s} & \frac{2c(-cs+\theta)}{s} & 0 \\ 0 & 0 & 0 & \frac{c\theta}{s} & 1-\frac{c\theta}{s} \\ \frac{c(-cs+\theta)}{2s} & \frac{c(cs-\theta)}{s} & \frac{c(-cs+\theta)}{2s} & 1+\frac{2c(cs-\theta)}{s} & 0 \\ 0 & 0 & 0 & 1-\frac{c\theta}{s} & \frac{c\theta}{s} \end{bmatrix} \tag{28}$$

where c and s are non-dimensional parameters defined as $c = \cos\theta$ and $s = \sin\theta$, and θ is the limb angle in radians.

The **SGO** matrices for box and cuspate folds are numerically computed because those fold geometries do not yield closed-form symbolic expressions. As a numerical method for one-dimensional integration, we use an N-point Gaussian quadrature rule to approximate the value of the integral by a weighted sum of the integrand $f(x)$ evaluated at optimal abscissas (nodes) x_q (e.g., Olver et al., 2010):

$$\int_a^b f(x)dx \approx \sum_{q=1}^{N} w_q f(x_q) \tag{29}$$

where w_q are the weights at x_q. Unlike other quadratures using evenly spaced nodes, Gaussian quadrature chooses the nodes and weights to yield the best possible accuracy. Higher accuracy can also be obtained by increasing N. Here 550 Gaussian points (N) are used within one-complete fold cycle, and the Gaussian locations (x_q) and corresponding weights (w_q) are determined through the *Mathematica* function "GaussianQuadratureWeights." We calculate the numerical **SGO** matrices of box folds defined by the power function with $m = 3$ (equations (3), (4), (5) and (6)) and cuspate folds with $m = 0.5$ (equations (3) and (8)). Although an ideal box fold requires $m \rightarrow \infty$, the exponent $m = 3$ is chosen for systematic comparison with the other fold types of $m \leq 2$. In the numerical computation of **SGO**, all the fold parameters such as limb angle (θ) need to be specified a priori unlike the analytical expressions for the **SGO** described earlier. Thus, numerical **SGO** matrices on specific θ are expressed in numbers.

To examine the accuracy of my numerical integration, we compared the numerically computed **SGO** of the sinusoidal fold at $\theta = 89°$ with the analytically calculated **SGO** of the same fold shape because higher limb angles are expected to lead to larger errors in the numerical calculation. The maximum difference between the corresponding elements of analytical and numerical EM_S stiffness (**C***) at $\theta = 89°$ was 3.08×10^{-5} GPa (~0.00009% of the analytical value) when the stiffness tensor of the Haast schist (Okaya and Christensen, 2002) (see the next section) was used as $\mathbf{C}^{\mathbf{rep}}$.

As seen above, the **SGO** is a function of the limb angle (θ) and dependent on hinge shape, but is scale-independent. Thus, it is possible to investigate variations of the EM_S stiffness with variation in θ and fold types over a full range of relevant scales. This **SGO** concept allows efficient seismic modeling aimed at evaluating the effect of folding on seismic properties from rocks representative of target areas. Using my analytical and numerical solutions, one can obtain variations and limits of seismic velocities, shear wave splitting and seismic anisotropies including magnitude and symmetry, depending on fold limb angle, as shown in the following sections.

4.4. Validation of Fold EM_S Stiffnesses (C*) from the Calculated SGO

In this section, the Voigt and Reuss methods for the calculations of bulk elastic stiffness are validated using the AEH method for sinusoidal folds. Once the accuracy of the Voigt and Reuss methods has been established, comprehensive results will be presented for seismic velocity and anisotropy as functions of fold type and limb angle via the Voigt and Reuss schemes. The Reuss formulation will be presented in section 4.7.1.

In order to validate and investigate the influence of fold geometry on the stiffnesses of its EM_S and the velocities of seismic waves propagating through the EM_S, we take the stiffness tensor of the Haast schist of South Island, New Zealand (Okaya and Christensen, 2002) as an example of the representative rock stiffness ($\mathbf{C}^{\mathbf{rep}}$). The density of the Haast schist (2718 kg/m^3) is used as the EM_S density (ρ^*). The Haast schist has a strong foliation caused by the preferred orientation of micaceous minerals and exhibits hexagonal symmetry with the *c* axis being the slow symmetry axis, and its elastic constants were derived from petrophysical measurements at 600 MPa (Okaya and Christensen, 2002). From the velocity and density data in Okaya and Christensen (2002), we obtain the 6×6 Haast schist stiffness tensor ($\mathbf{C}^{\mathbf{rep}} = \mathbf{C}$):

$$\begin{matrix}\text{Haast schist}\\ \text{(Unit is GPa)}\end{matrix} \quad \mathbf{C}^{\mathbf{rep}} = \mathbf{C} = \begin{bmatrix} 114.87 & 30.87 & 23.86 & 0 & 0 & 0 \\ 30.87 & 114.87 & 23.86 & 0 & 0 & 0 \\ 23.86 & 23.86 & 89.86 & 0 & 0 & 0 \\ 0 & 0 & 0 & 30.18 & 0 & 0 \\ 0 & 0 & 0 & 0 & 30.18 & 0 \\ 0 & 0 & 0 & 0 & 0 & 42.00 \end{bmatrix} \tag{30}$$

Based on equations (25) and (26), the EM_S stiffness ($\mathbf{C}^{*\mathbf{Voigt}}$) for sinusoidal folds of the Haast schist is orthorhombic in symmetry and can be plotted as a function of limb angle (θ). Fig. 4.7a illustrates strong variations of Voigt EM_S stiffness components for sinusoidal folds with respect to θ ranging from 0° to 90°, and also compares them with Reuss and AEH results. With increasing θ, the stiffness in the horizontal direction (C_{11}^{*Voigt}) decreases and the vertical stiffness (C_{33}^{*Voigt}) increases trigonometrically. The stiffnesses are directly related to velocity of quasi-*P* waves propagating in the *x* and *z* directions, respectively, in the geographical frame (e.g., see Auld (1990, appendix 3) for relationship between

velocities and elastic constants in orthorhombic symmetry). The two elastic stiffnesses cross over at a limb angle of 60°, and thus the symmetry of the EM_S stiffness tensor increases at the crossover limb angle. This crossover limb angle (θ_c) is solely a property of the **SGO** and independent of the $\mathbf{C}^{\mathbf{rep}}$. For instance, the chevron fold has θ_c of 45°. In Fig. 4.7a, the Voigt and Reuss values have only minor (second-order) differences and are almost identical to the AEH results, compared with substantial (first-order) variations in EM_S stiffnesses with respect to θ. For example, while the maximum first-order change in C^*_{11} with all θ is 25.01 GPa, the difference between the Voigt and Reuss values for C^*_{11} is at most 2.41 GPa (~9.64% of the maximum first-order change) when $\theta \approx 38°$. In addition, the maximum C^*_{11} differences of the Voigt and Reuss from the AEH results are, respectively, only 2.16 GPa (~8.64% of the maximum first-order change) when $\theta \approx 37°$ and 0.28 GPa (~1.12% of the maximum first-order change) when $\theta \approx 46°$. The quasi-*P* wave velocities in three different propagation directions relative to the geographical axes (*x*-*y*-*z*) are plotted in Fig. 4.7b as a function of θ. In the Voigt graph, the wave speed at a propagation angle of 45° ($qV_{P45°}$) is faster than the wave speeds in the horizontal ($qV_{P90°}$) and vertical direction ($qV_{P0°}$) over ~48° ≤ θ ≤ ~67°. The Reuss and AEH plots also show very similar behavior to the Voigt. The percent anisotropy of a fold structure is expected to show a strong dependence on θ. As seen in Fig. 4.7, the AEH stiffness and wave speed values lie between the Voigt and the Reuss bounds and their close relationship indicate that my methodology for fold EM_S is mathematically correct and the approach using the Voigt or Reuss methods provide useful values for bulk fold stiffness.

Figure 4.6. Comparison of stiffness and wave speed among Voigt, Reuss, and AEH for sinusoidal fold. (a) Strong variations of EM_S stiffnesses (C^*) for sinusoidally folded Haast schist with respect to limb angle (θ) ranging from 0° to 90°. Four bulk elastic stiffnesses are selectively plotted and compared between the Voigt, Reuss and AEH results. Note a very close relationship between the three bounds. The crossover limb angle (θ_c; marked by black dashed line) at $C^*_{11} = C^*_{33}$ is solely a property of the **SGO**, irrespective of the $\mathbf{C}^{\mathbf{rep}}$. (b) Sharp dependence of quasi-*P* wave speeds on θ in three different propagation directions for sinusoidally folded Haast schist. Here qV_{P0°, qV_{P45°, and qV_{P90° denote the quasi-*P* wave velocities in the vertical (i.e., *z* axis), 45° to the vertical geographical axis, and the horizontal direction (i.e., *x* axis), respectively, in the *x*-*z* plane. The seismic velocities from different homogenization methods (Voigt, Reuss and AEH) exhibit only minor second-order differences, compared with substantial first-order changes in wave speed with respect to θ.

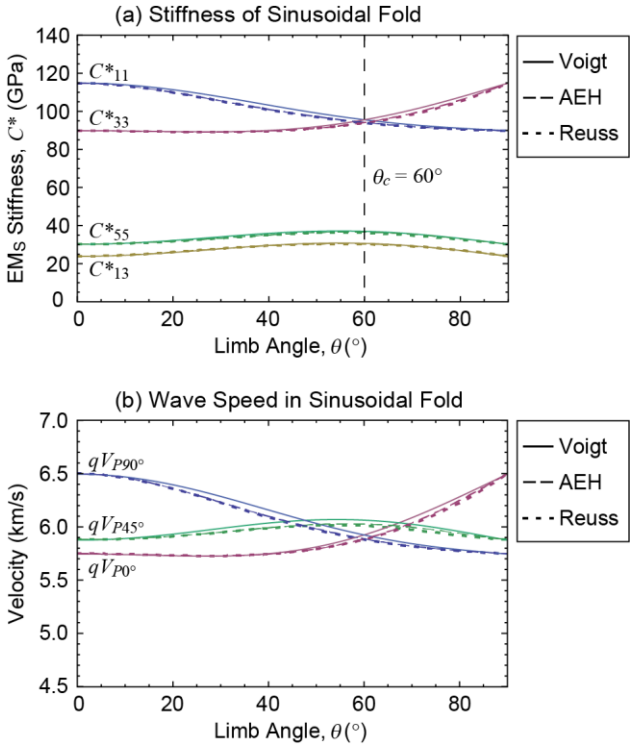

4.5. Effect of Fold Structure on 2-D Seismic Velocity

In this section, we show the velocity results of three body waves from the Voigt EM_S calculation with respect to propagation direction and fold limb angle. Fig. 4.8 illustrates qV_P, qV_{SH} and qV_{SV} in the *x*-*z* axial plane for sinusoidal folds at specific limb angles (θ = 0°, 30°, 60°, 90°). Propagation angle γ is measured from the vertical *z* axis in the sagittal plane and is shown for the range of 0° to 90° owing to its orthorhombic symmetry.

At θ = 0° (Fig. 4.8a), the EM_S is equivalent to the Haast schist with horizontal foliation. In Fig. 4.6a, qV_P and qV_{SH} increase with increasing γ since their propagation and polarization directions draw closer to the foliation, and qV_{SV} shows the minimum in the *x* and *z* axes because either its propagation or polarization direction is perpendicular to the foliation. In the fold at θ = 30° (Fig. 4.8b), the crossover of qV_{SH} and qV_{SV} occurs at a smaller γ and the variation in shear velocities is less pronounced compared with the original rock in Fig. 4.8a. At the crossover limb angle (θ_c = 60°) of the sinusoidal fold, the graph in the *x*-*z* plane shows symmetrical velocity behavior with respect to γ of 45° (Fig. 4.8c). This is because the EM_S stiffness at the θ_c has only 6 components indicating a form of tetragonal symmetry ($C_{11}^{*Voigt} = C_{33}^{*Voigt}$, $C_{44}^{*Voigt} = C_{66}^{*Voigt}$ and $C_{12}^{*Voigt} = C_{23}^{*Voigt}$). Since the variation in qV_P for the fold at its θ_c is less than those at any other θ, a minimum seismic anisotropy is expected. When θ = 90°, the EM_S is equivalent to vertically orientated Haast schist and thus the 90° rotated $\mathbf{C}^{\mathbf{rep}}$ on the *y* axis (hinge line) is used as the EM_S stiffness. Consequently, the velocity graph when θ = 90° is the mirror image of the plot when θ = 0° in the *x*-*z* plane (Fig. 4.8d).

If the velocity graphs in a plane are assembled for all limb angles between 0° to 90°, a surface plot with three axes of limb angle, propagation angle and velocity allows simultaneous investigation of the effect of both the propagation and limb angles on seismic velocity in a plane (Fig. 4.9a). Fig. 4.9b illustrates seismic velocity surface plots of the EM_S for the five fold types with respect to γ and θ in the *x*-*z*, *y*-*z* and *x*-*y* axial planes. γ in the *x*-*y* plane is defined as the angle measured counterclockwise from the horizontal *x* axis to the wave propagation direction (**n**) in the transverse plane. For a specific fold type, the surface plots of the seismic velocities show clear distinction between the three axial planes. Additionally, in a given plane, the velocity surfaces vary with different fold types for all θ except 0° and 90°, as shown by the crossover lines of qV_{SH} (denoted by blue surface) and qV_{SV} (denoted by green surface) in Fig. 4.9b.

The results of my analyses using idealized fold structures suggest that folds much smaller than the seismic wavelength can be detected given appropriate station deployments even though they cannot be directly imaged. It might also be possible to identify limb dip and orientation of subsurface folds in the

crust based on specific velocity patterns. This in turn may shed additional light on the kinematics of in situ crustal deformation in orogenic belts.

Figure 4.7. 2-D seismic velocity plot of the Voigt EM_S for single-layered sinusoidal folds. The velocity graphs are plotted at specific limb angles (θ = (a) 0°, (b) 30°, (c) 60° and (d) 90°) with propagation angle γ in the *x*-*z* plane. qV_{SH} and qV_{SV} are the shear wave velocities with the largest polarization component in the directions normal and parallel, respectively, to their sagittal planes. In the schematic diagrams, each cube illustrates an effective medium (bulk stiffness tensor and density) representing the fold with specific θ. Planar and folded foliation forms are provided only for illustrative purposes and do not represent layers. The fold EM_S when θ = 0° has the same stiffness as the representative rock (Haast schist with horizontal foliation), i.e., $\mathbf{C}^{\mathbf{rep}}$, and thus the geographical axes (*x*-*y*-*z*) are identical to the rock symmetry axes (*a*-*b*-*c*). When θ = 90°, the fold EM_S displays vertical foliation and the 90° rotated $\mathbf{C}^{\mathbf{rep}}$ on the *y* axis is used as the EM_S stiffness. A propagation direction (**n**) is denoted by red arrow.

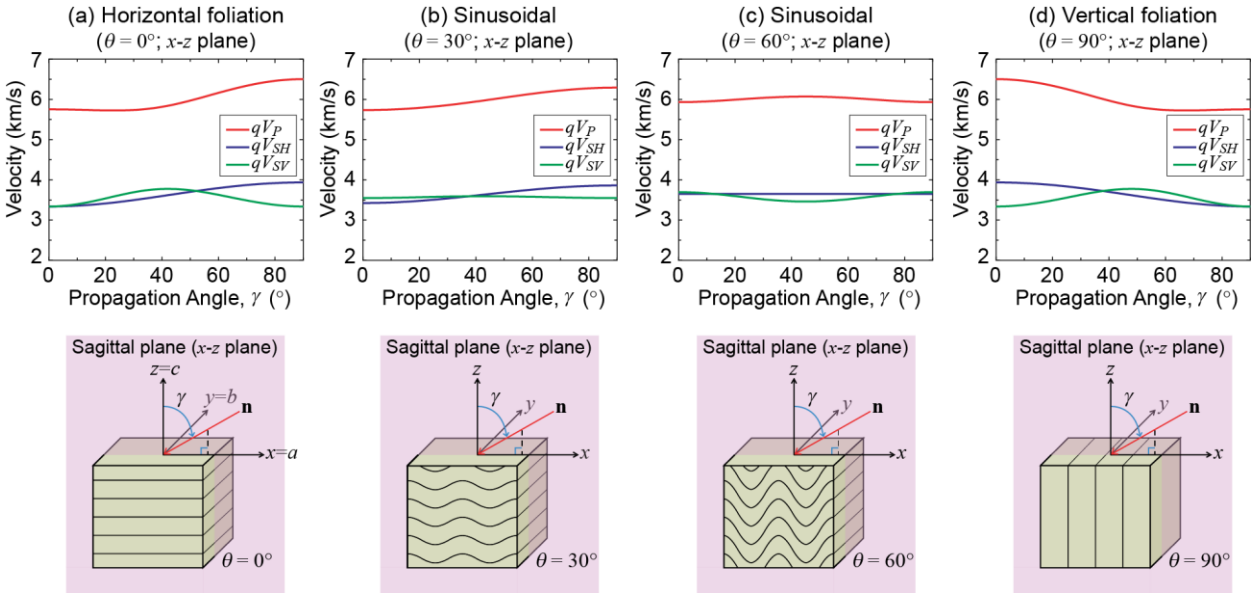

Figure 4.8. Seismic velocity surface plots of the Voigt EM_S as functions of propagation angle (γ) and limb angle (θ). *qP* and two *qS* velocities are shown for the three axial planes. (a) Conceptual method to create each set of velocity surface plots. Two horizontal axes are propagation angle and fold limb angle; one vertical axis is seismic velocity. A velocity versus propagation angle graph in an axial plane such as Fig. 4.6 is drawn for a given limb angle. When the graphs for all θ from 0° to 90° are assembled, seismic velocity surfaces for the axial plane are produced. As an example, four graphs for sinusoidal folds at θ = 0°, 30°, 60°, 90° in the *x*-*z* plane are illustrated. (b) Velocity surface plots for the five fold types in the *x*-*z*, *y*-*z*, and *x*-*y* planes. They are presented in order of decreasing hinge curvature (i.e., from cuspate to box fold). The grid (marked by black solid lines) on the colored surfaces represents propagation and limb angles from 0° to 90° in 5° intervals. Note the crossover of qV_{SH} and qV_{SV} (i.e., the intersection of the blue and green surfaces), explicitly showing variations of velocity patterns between the different fold types in each axial plane as well as between the three axial planes for a fold type. The employed axial planes are marked by pink color in the schematic diagrams. The cube in the diagrams illustrates a sinusoidal fold EM_S as an example of the idealized folds.

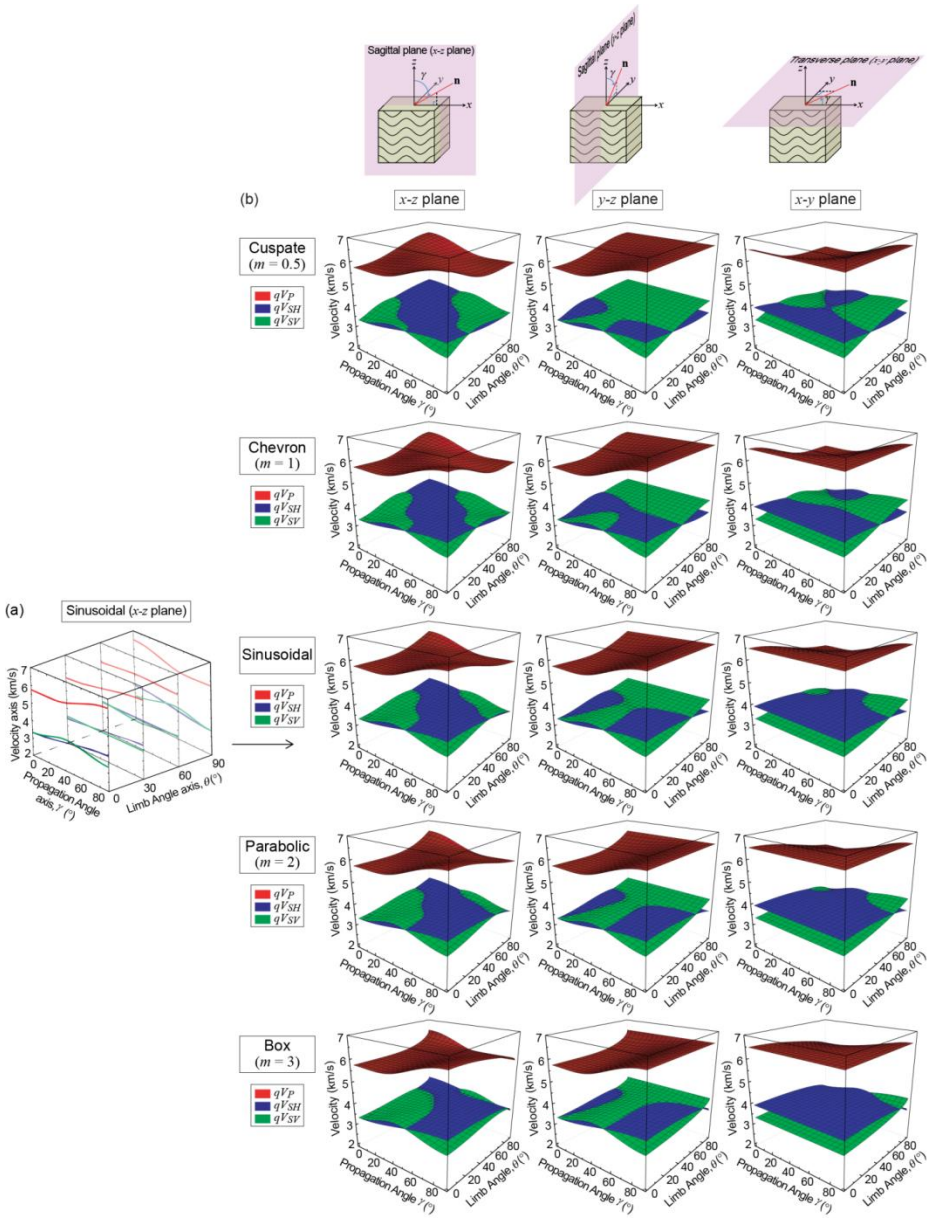

4.6. Effect of Fold Structure on 3-D seismic Properties and Anisotropy

Seismic anisotropy of a fold EM_S at a specific limb angle is calculated from seismic wave velocities propagating in all possible directions through the 3-D fold structure. Fig. 4.9 displays the 3-D seismic velocity of quasi-*P* wave (qV_P) and 3-D shear wave splitting (δt) for the EM_S at specific limb angles (θ = 0°, 15°, 30°, 45°, 60°, 75°, 90°) on spherical surfaces in the *x*-*y*-*z* geographical frame. Shear wave splitting (δt) is defined by the difference in fast (qV_{S1}) and slow (qV_{S2}) shear wave velocities and expressed in split time per propagation distance (s/km):

$$\delta t = \frac{1}{qV_{S2}} - \frac{1}{qV_{S1}} \tag{31}$$

Seismic anisotropy (*A*) is defined as follows (Birch, 1961) and the quasi-*P* wave anisotropy (AV_P) is presented below each velocity sphere in Fig. 4.9:

$$A = 100 \times \frac{qV_{\max} - qV_{\min}}{(qV_{\max} + qV_{\min}) \times 0.5} \tag{32}$$

In the foliated Haast schist showing slow-axis hexagonal symmetry, the fastest propagation direction of quasi-*P* wave (*qP*) is parallel to the foliation and the slowest *qP* direction is normal to the foliation. The chevron fold geometry composed solely of locally planar foliation provides relatively simple interpretation of the relationship between qV_P and foliation orientation (Fig. 4.9b). qV_P in the *y* direction is fastest for all θ since the *y* axis as the hinge line is always parallel to the foliation. qV_P in the *x* direction decreases with increasing θ and is minimum when θ = 90° because the angle between the *x* axis and foliation increases during progressive folding. On the other hand, qV_P behavior in the *z* axis is opposite to that in the *x* axis. When θ = 45° (crossover limb angle (θ_c) for chevron folds), qV_P in the *x* and z directions show the same minimum velocity but higher value than other minimum velocities in the qV_P spheres at other θ since both axes make an angle of 45° with the foliation. Consequently, the chevron fold at its θ_c has minimum seismic anisotropy (AV_P = 10.39%). The symmetry of velocity patterns also differ based on fold limb angle. At θ = 0° and 90°, the fold represents vertical-axis hexagonal symmetry equal to the Haast schist and horizontal-axis hexagonal symmetry, respectively. However, the fold symmetry is

changed to tetragonal at the θ_c and orthorhombic at all other θ, even though the internal rock filling the fold is still hexagonal.

For other fold types, although aspects of qV_P variations during progressive folding are similar to the chevron fold, velocity distributions on the spherical surfaces are different from the chevron fold at the same θ owing to differences in fold hinge curvature. In the sinusoidal fold at θ = 45°, qV_P in the x direction is faster than in the z direction because the curved foliation in the hinge area forms smaller angles with the x axis than with the z axis (Fig. 4.9c). Thus, a sinusoidal fold at a limb angle larger than 45° will have an equivalent effect on qV_P in the x and z directions. In this case, the θ_c is 60°. Similarly, lower θ_c in cuspate fold than that of chevron fold is expected due to its sharper hinge shape, and parabolic and box folds will have larger θ_c than sinusoidal fold (see Figs 4.9a, 4.9d, 4.9e, and 4.10). Thus, the seismic anisotropy of a fold is influenced by its hinge shape as well as its limb dip.

Since the degree of anisotropy can be determined from a measurement of shear wave splitting at a single station, splitting delay time (δt) is used as a powerful tool for investigating the seismic anisotropy of an area of interest. In the case of θ = 0°, shear waves propagating parallel to foliation exhibit maximum splitting delay (0.0457 s/km) and there is no shear wave splitting in the z direction (Fig. 4.9). The chevron fold at θ = 45° has maximum splitting of 0.0306 s/km, which is ~70% of the original rock maximum δt. However, the maximum δt direction is not parallel to the foliation of the chevron fold but tilted by 45° from all three (x-y-z) axes (Fig. 4.9b). As seen in all the δt plots, the δt patterns and maximum values of folds are changed based on fold type and limb angle, which are clearly different from the original rock (Fig. 4.9). We note that these splitting values reflect the idealized fold geometries, and would vary accordingly in real folds owing to variable foliation orientations and other geometrical and compositional variability.

Fig. 4.11 illustrates seismic anisotropies (A) of three body waves (*qP*, *qS1* and *qS2*) with respect to limb angle (θ) for the five fold types made of the Haast schist. Each anisotropy value is computed using equation (32) and plotted at each integer θ from 0° to 90° and also at the crossover limb angle (θ_c). Folding lowers the seismic anisotropy of the original Haast schist. The seismic anisotropies for *qP* and

qS1 generally decrease approaching θ_c and show minimum values at the θ_c. Difference in anisotropy graph patterns with θ between fold types in Fig. 4.11 indicates that seismic anisotropy is obviously affected by fold geometry including limb angle and hinge shape.

Figure 4.9. 3-D seismic velocity of quasi-*P* wave (qV_P) and shear wave splitting (δt) for the Voigt EM_S of single-layered folds. The velocity spheres are plotted for (a) cuspate with m = 0.5, (b) chevron, (c) sinusoidal, (d) parabolic and (e) box with m = 3 (in order of increasing fold crossover limb angle) at specific limb angles (θ = 0°, 15°, 30°, 45°, 60°, 75° and 90°). They were computed and plotted at 64800 (=360×180) points for full 360°×180° coverage (i.e., 1° interval plot in all propagation directions on spherical surfaces). The 3-D seismic properties for each EM_S were visualized using the same color scale to emphasize relative values and distributions (i.e., maximum 6.5010 km/s and minimum 5.7218 km/s for qV_P; maximum 0.0457 s/km and minimum 0 s/km for δt). The EM_S schematic diagrams display the foliation orientation and the fold geometries at their θ. The *x*-*y*-*z* geographical frame and legends of qV_P and δt are also shown in the rightmost column. The maximum and minimum velocities and seismic anisotropy (AV_P) for the EM_S at each θ are rounded off to two decimal places and presented below each velocity sphere. The maximum δt is shown below each δt sphere. Note variations in value and pattern (symmetry) of qV_P and δt based on fold type and limb angle.

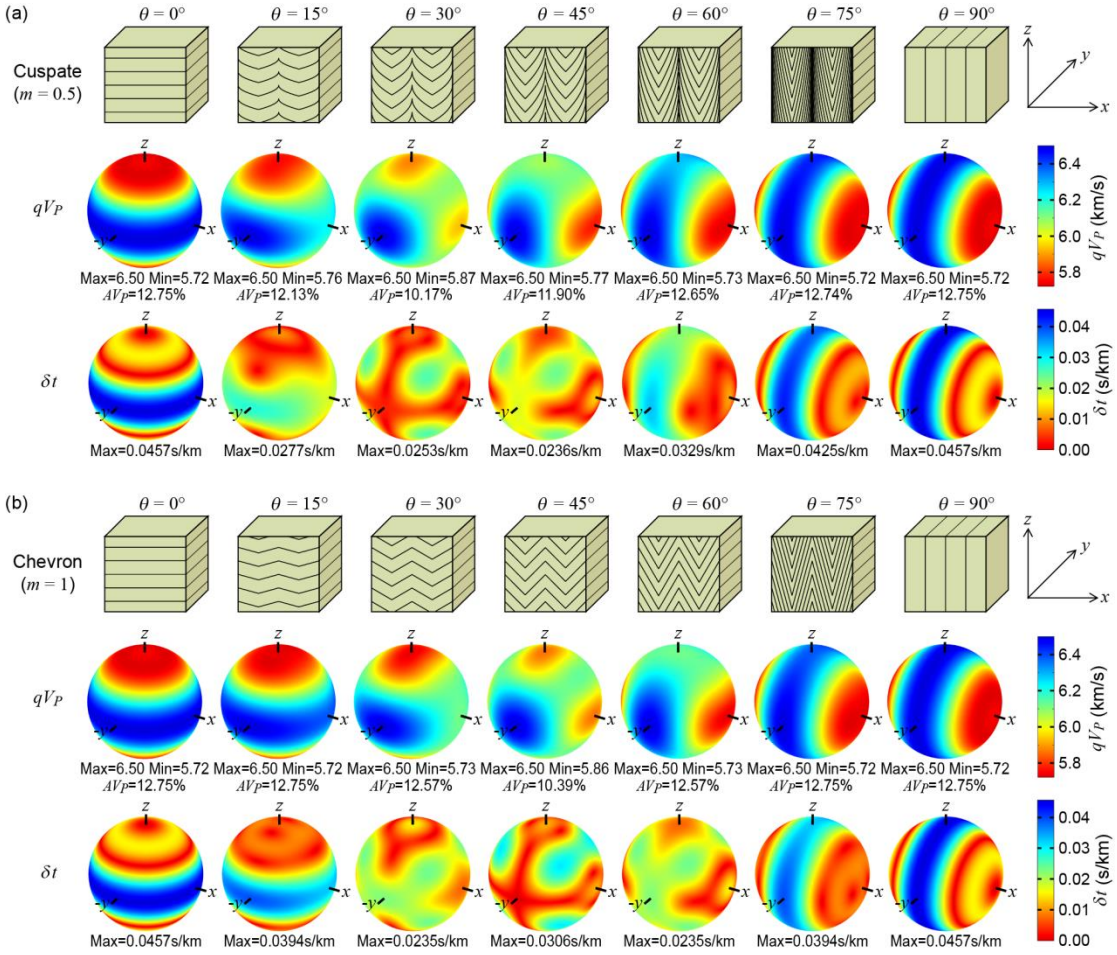

Figure 4.9. (continued)

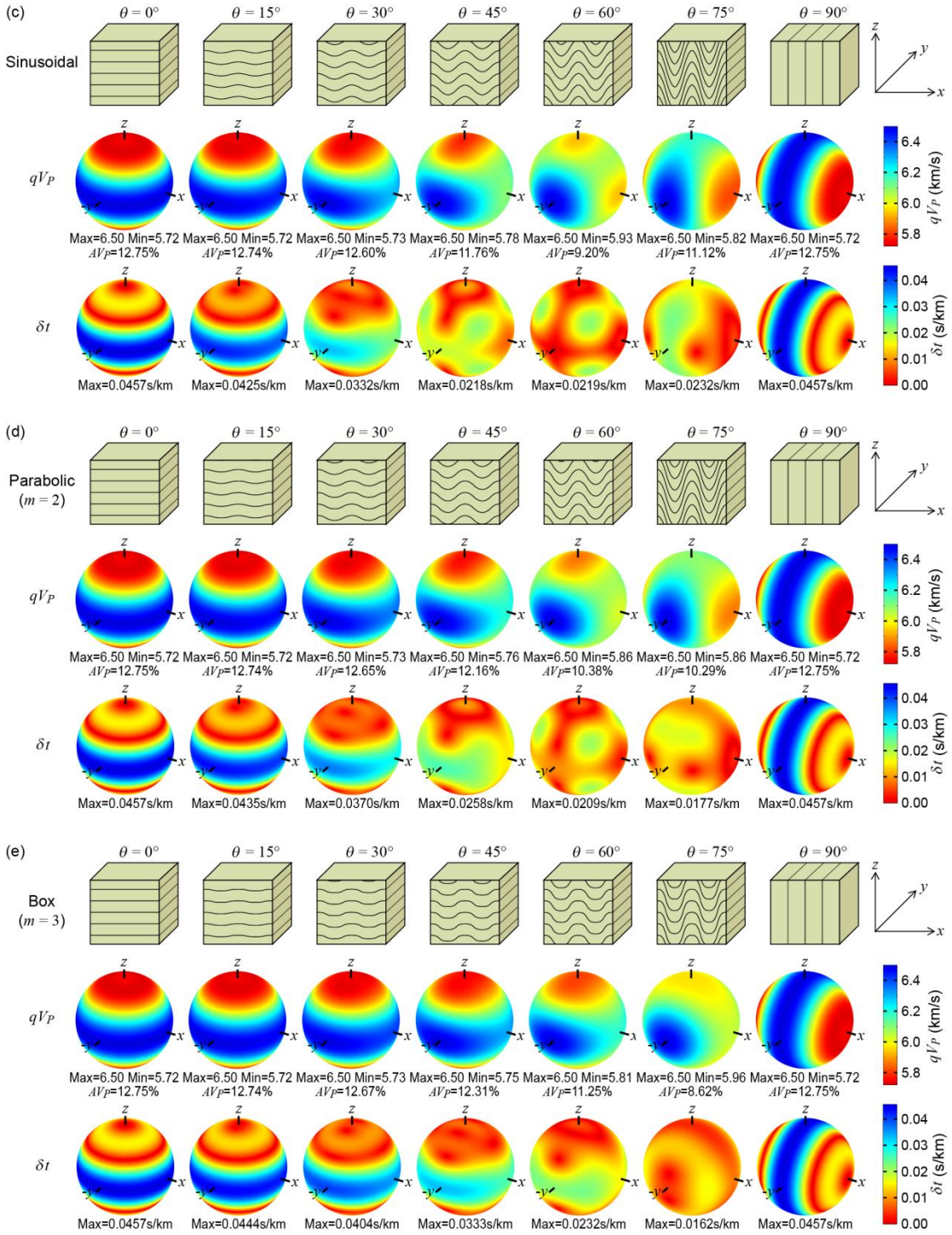

Figure 4.10. 3-D seismic velocity of quasi-*P* wave (qV_P) and shear wave splitting (δt) at critical limb angles (θ_c). The velocity spheres are plotted for the Voigt EM_S of the five types of single-layered folds made of the Haast schist. They were computed and plotted in the same way as Fig. 4.9. The schematic diagrams display the fold geometries at their θ_c. Because all the EM_S at θ_c have tetragonal symmetry, the seismic properties exhibit similar patterns between the different fold types. However, the values of seismic properties are different.

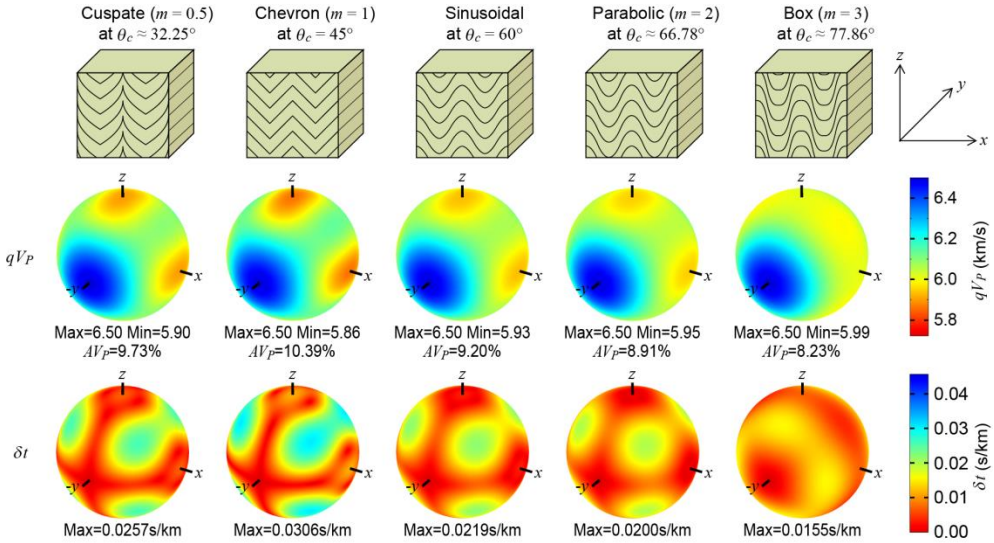

Figure 4.11. Seismic anisotropy plots of the Voigt EM_S for the five fold types with respect to limb angle (θ). They are presented in order of increasing fold crossover angle (i.e., from cuspate to box fold). A single seismic anisotropy value is computed from a 3-D seismic velocity sphere and plotted at each integer θ from 0° to 90° including the crossover limb angle (θ_c) at which the horizontal and vertical stiffnesses are equal. Our idealized folds made of the Haast schist show minimum seismic anisotropies for both *qP* and *qS1* waves at their θ_c except that box fold with $m = 3$ displays a minimum anisotropy for *qP* at $\theta = 77°$ and for *qS1* at its θ_c.

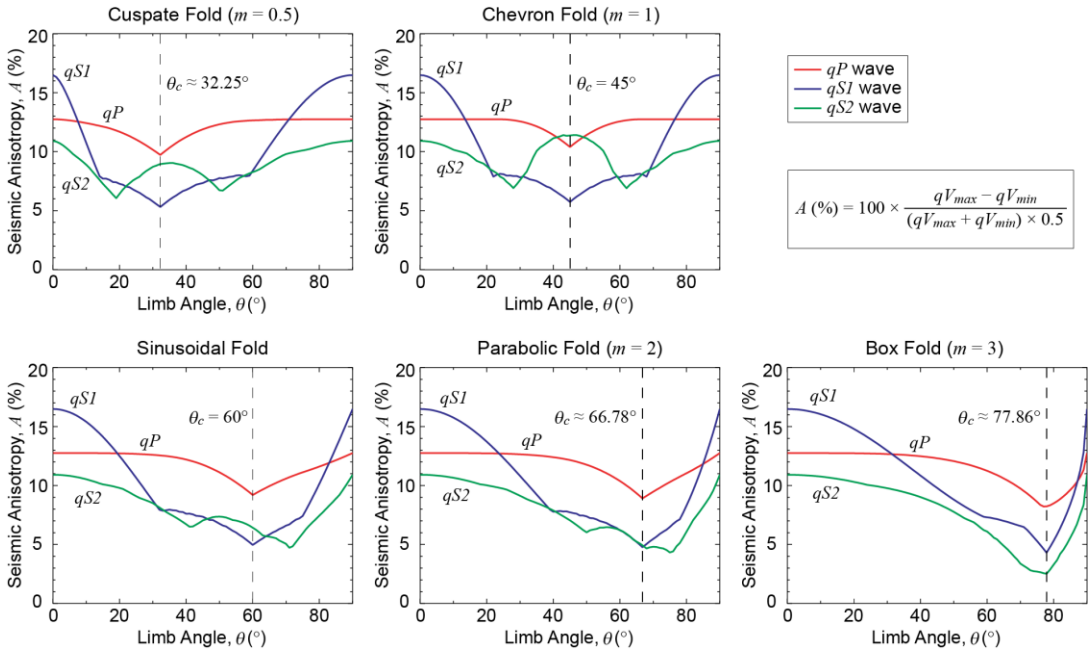

4.7. Discussion

4.7.1. Comparison to Reuss Estimate

We have used the Voigt estimate to calculate the bulk stiffness tensors of fold EM_S (equation (13)). The Voigt estimate assumes uniform elastic strain and provides an upper bound of effective stiffness (Voigt, 1928). The Reuss estimate on the other hand assumes uniform elastic stress and gives a lower bound of effective stiffness (Reuss, 1929). The true bulk stiffness of a fold EM_S will fall somewhere between the two theoretical bounds depending on its geometric details as shown in section 4.4 and Fig. 4.6. Here we compare the Reuss lower bound for chevron, sinusoidal and parabolic folds made of the Haast schist to my previous results.

Similar to the Voigt averaging scheme, if the local rock compliance tensor (**S**) can be replaced by a representative rock compliance tensor ($\mathbf{S}^{\mathbf{rep}}$) in equation (15), the bulk compliance ($\mathbf{S}^{*\mathbf{Reuss}}$) is given by the product of a $\mathbf{SGO}^{\mathbf{Reuss}}$ and the $\mathbf{S}^{\mathbf{rep}}$:

$$S_{ijkl}^{*Reuss} = \left[\frac{1}{V} \int \{ a_{im} a_{jn} a_{ko} a_{lp} \}_{(x,y,z)} dV \right] S_{mnop}^{rep} \tag{33}$$

or

$$\mathbf{S}^{*\mathbf{Reuss}} = \mathbf{SGO}^{\mathbf{Reuss}} \mathbf{S}^{\mathbf{rep}} \tag{34}$$

This can be expressed using matrix operations as

$$[S^{*Reuss}]_{21\times 1} = [SGO^{Reuss}]_{21\times 21} [S^{rep}]_{21\times 1} \tag{35}$$

It is noted that the $\mathbf{SGO}^{\mathbf{Reuss}}$ matrix for the compliance in equation (34) is different from the $\mathbf{SGO}^{\mathbf{Voigt}}$ matrix for the stiffness in equation (22) because the Voigt contraction of the elastic compliances is not the same as those for the elastic stiffnesses (e.g., Nye, 1985, chapter 8; Ting, 1996, chapter 2). Finally, the EM_S bulk stiffness tensor ($\mathbf{C}^{*\mathbf{Reuss}}$) for the Reuss bound is obtained by

$$\mathbf{C}^{*\mathbf{Reuss}} = [\mathbf{S}^{*\mathbf{Reuss}}]^{-1} \tag{36}$$

4.7.1.1. $\mathbf{SGO}^{\mathbf{Reuss}}$ for Folds Made of Hexagonally Symmetric Rocks

If the $\mathbf{S}^{\mathbf{rep}}$ for a cylindrical fold is assumed to have hexagonal symmetry with 5 independent components, which can be calculated from the representative rock stiffness ($\mathbf{C}^{\mathbf{rep}}$), the **SGO** matrix for the elastic compliances is of dimension 9×5. Each $\mathbf{SGO}^{\mathbf{Reuss}}$ for chevron, sinusoidal and parabolic folds is as follows:

$$[SGO^{Reuss}]_{sinusoidal} = \begin{bmatrix} \frac{B+1}{D^3} & \frac{2B}{D^3} & \frac{B(2D-3)+D-1}{D^3} & \frac{B}{D^3} & 0 \\ \frac{1}{D} & 1-\frac{1}{D} & 0 & 0 & -\frac{1}{2D} \\ \frac{B}{D^3} & 1-\frac{2B}{D^3} & \frac{B}{D^3} & -\frac{B}{D^3} & 0 \\ 1 & 0 & 0 & 0 & 0 \\ 1-\frac{1}{D} & \frac{1}{D} & 0 & 0 & -\frac{1}{2}+\frac{1}{2D} \\ \frac{B(2D-3)+D-1}{D^3} & \frac{2B}{D^3} & \frac{B+1}{D^3} & \frac{B}{D^3} & 0 \\ 0 & 0 & 0 & \frac{1}{D} & 1-\frac{1}{D} \\ \frac{4B}{D^3} & -\frac{8B}{D^3} & \frac{4B}{D^3} & 1-\frac{4B}{D^3} & 0 \\ 0 & 0 & 0 & 1-\frac{1}{D} & \frac{1}{D} \end{bmatrix} \quad (37)$$

where B and D are non-dimensional parameters that have been previously defined in section 4.3.5, and θ is the limb angle.

$$[SGO^{Reuss}]_{chevron} = \begin{bmatrix} c^4 & 2c^2s^2 & s^4 & c^2s^2 & 0 \\ c^2 & s^2 & 0 & 0 & -\frac{c^2}{2} \\ c^2s^2 & c^4+s^4 & c^2s^2 & -c^2s^2 & 0 \\ 1 & 0 & 0 & 0 & 0 \\ s^2 & c^2 & 0 & 0 & -\frac{s^2}{2} \\ s^4 & 2c^2s^2 & c^4 & c^2s^2 & 0 \\ 0 & 0 & 0 & c^2 & s^2 \\ 4c^2s^2 & -8c^2s^2 & 4c^2s^2 & (c^2-s^2)^2 & 0 \\ 0 & 0 & 0 & s^2 & c^2 \end{bmatrix} \quad (38)$$

$$[SGO^{Reuss}]_{parabolic} = \begin{bmatrix} \frac{c(cs+\theta)}{2s} & \frac{c(-cs+\theta)}{s} & 1+\frac{c(cs-3\theta)}{2s} & \frac{c(-cs+\theta)}{2s} & 0 \\ \frac{c\theta}{s} & 1-\frac{c\theta}{s} & 0 & 0 & -\frac{c\theta}{2s} \\ \frac{c(-cs+\theta)}{2s} & 1+\frac{c(cs-\theta)}{s} & \frac{c(-cs+\theta)}{2s} & \frac{c(cs-\theta)}{2s} & 0 \\ 1 & 0 & 0 & 0 & 0 \\ 1-\frac{c\theta}{s} & \frac{c\theta}{s} & 0 & 0 & -\frac{1}{2}+\frac{c\theta}{2s} \\ 1+\frac{c(cs-3\theta)}{2s} & \frac{c(-cs+\theta)}{s} & \frac{c(cs+\theta)}{2s} & \frac{c(-cs+\theta)}{2s} & 0 \\ 0 & 0 & 0 & \frac{c\theta}{s} & 1-\frac{c\theta}{s} \\ \frac{2c(-cs+\theta)}{s} & \frac{4c(cs-\theta)}{s} & \frac{2c(-cs+\theta)}{s} & 1+\frac{2c(cs-\theta)}{s} & 0 \\ 0 & 0 & 0 & 1-\frac{c\theta}{s} & \frac{c\theta}{s} \end{bmatrix} \quad (39)$$

where c and s are non-dimensional parameters that have been previously defined in section 4.3.5, and θ is the limb angle in radians.

4.7.1.2. Comparison of Seismic Velocity and Anisotropy among Voigt, Reuss, and AEH Estimates

We first compare the Reuss results to Voigt estimate. Fig. 4.12 shows the axial quasi-*P* and *S* wave velocities from Voigt and Reuss estimates for the EM_S of cylindrical chevron, sinusoidal and parabolic folds made of the Haast schist with hexagonal symmetry. Both estimates exhibit same velocity patterns with respect to limb angle (θ). For instance, the Reuss quasi-*P* wave velocities in the horizontal (*Px*) and vertical directions (*Pz*) trigonometrically decrease and increase, respectively, with increasing θ, and they cross over at their crossover limb angles (45° for chevron; 60° for sinusoidal; ~66.78° for parabolic), which are identical to the Voigt bound. At θ = 0° and 90°, the Voigt and Reuss bounds have the same wave speed because the bulk stiffness for both estimates is the same as the representative rock stiffness. At other θ, Reuss velocities are slightly lower than Voigt. The differences from the two bounds are minuscule compared with the first-order variations (the maximum change of ~0.75 km/s for *qP* and ~0.60 km/s for *qS*) caused by folding. In chevron folds, a maximum difference in quasi-*P* wave velocity between Voigt and Reuss bounds is ~0.07 km/s (~9.33% of the maximum first-order change) at θ = 27° for *Px* and at θ = 63° for *Pz*. In sinusoidal folds, a maximum difference of ~0.07 km/s between them is shown at θ = 39° for *Px* and at θ = 74° for *Pz*, and in parabolic folds, the same maximum difference

(~0.07 km/s) is at $\theta = 47°$ for *Px* and at $\theta = 78°$ for *Pz*. For horizontal (*Sxy*) and vertical quasi-shear waves (*Syz*), the Reuss velocities are lower than the Voigt by ~0.05 km/s (~8.33% of the maximum first-order change), which is a maximum difference between the two bounds, at their θ_c in the chevron, sinusoidal and parabolic folds.

Seismic anisotropies through the Ruess approach are also plotted and compared with the Voigt anisotropies in Fig. 4.13. The Reuss seismic anisotropies in the chevron, sinusoidal and parabolic folds display less variation with limb angle (θ) than the Voigt bounds. As expected from the velocity graphs of Fig. 4.13, a maximum difference in *qP* anisotropy between two estimates is shown at the crossover limb angle (θ_c), where Reuss anisotropy is higher by ~0.40% in the chevron fold, ~0.66% in the sinusoidal fold and ~0.71% in the parabolic fold (Fig. 4.13). A faster shear wave (*qS1*) has a similar pattern to *qP* seismic anisotropy. For instance, a difference in *qS1* anisotropy between two bounds increases approaching θ_c, at which the chevron, sinusoidal and parabolic folds have differences of ~1.06%, ~0.96% and ~0.95%, respectively (Fig. 4.13). For a slower shear wave (*qS2*), there is a maximum difference in anisotropy between two estimates near θ_c (35° and 55° for chevron; 53° for sinusoidal; 63° for parabolic). Therefore, if a fold limb angle is close to its θ_c, both the Voigt and Reuss approaches may need to be considered when studying seismic responses of the fold structure through a seismic anisotropy analysis. However, the differences in seismic anisotropy between the averaging methods (e.g., maximum of ~0.66% in *qP* anisotropy of the sinusoidal fold) are considerably smaller than the anisotropy variations caused by geometry, or limb angle (e.g., maximum of ~3.55% (= 12.75% − 9.20%) for Voigt and ~2.89% (= 12.75% − 9.86%) for Reuss in *qP* anisotropy of the sinusoidal fold) (Fig. 4.13).

Figure 4.12. Comparison of axial velocities between Voigt and Reuss estimates. The velocities are plotted for the EM_S of the (a) chevron, (b) sinusoidal and (c) parabolic folds made of the Haast schist. The wave speeds are plotted as a function of limb angle (θ). Propagation directions and particle motion of *qP* and *qS* waves are labeled relative to the geographical axes (*x*-*y*-*z*). For instance, *Sxy* denotes *qS* wave propagating in the *x* direction and polarized in the *y* direction. Solid and dotted curves represent the Voigt and Reuss bounds, respectively. The AEH velocities are also plotted for sinusoidal folds in (b) and marked by dashed curve. Note only minor differences between the Voigt and Reuss velocities for the three fold types and also that the AEH graphs lie between the Voigt and Reuss bounds in (b).

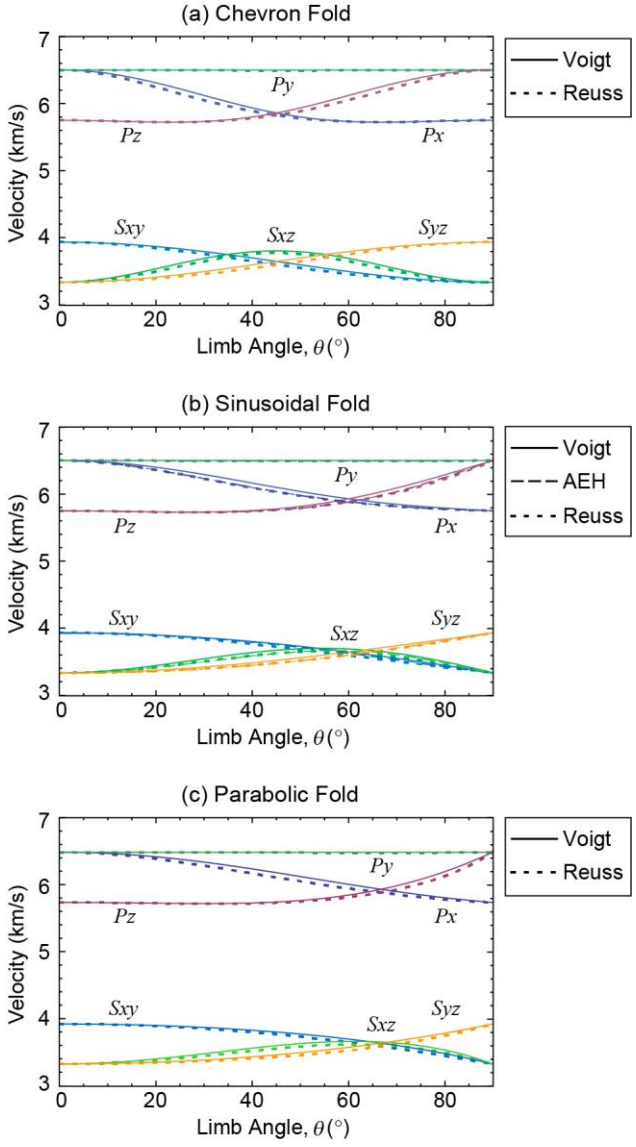

Figure 4.13. Comparison of seismic anisotropies between Voigt and Reuss estimates The seismic anisotropies are plotted for the EM_S of the (a) chevron, (b) sinusoidal and (c) parabolic folds made of the Haast schist. The Reuss seismic anisotropies (dotted curves) are plotted on the Voigt anisotropy graphs (solid curves) in Fig. 4.10 and exhibit less variation with limb angle than the Voigt anisotropies. The AEH anisotropies (dashed curves) are also shown for sinusoidal folds in (b). Note that the differences between the three bounds are considerably smaller than the anisotropy variations caused by folding.

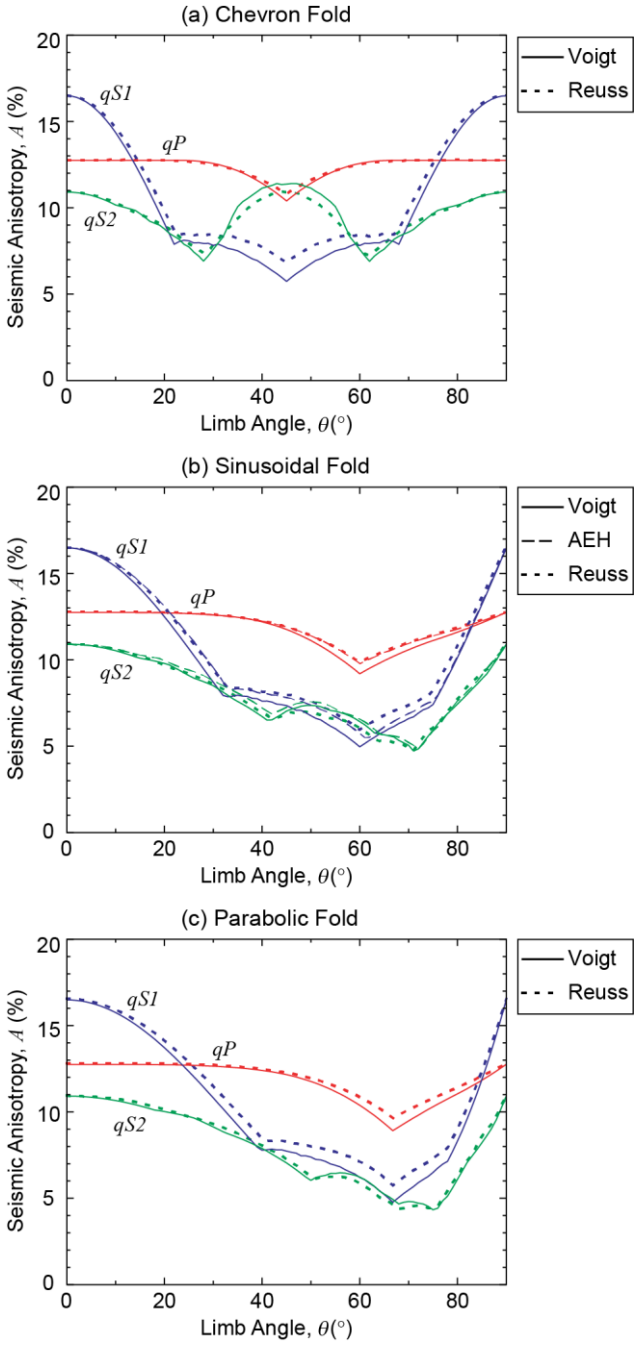

Figs 4.11b and 4.13b also include the AEH results. In Fig. 4.12b, the AEH axial velocities with respect to limb angle lie between the Voigt and Reuss bounds, but are closer to the Reuss, and have maximum differences in *qP* and *qS* waves, respectively, of ~0.07 km/s and ~0.05 km/s from the Voigt, and ~0.02 km/s and ~0.04 km/s from the Reuss. The AEH seismic anisotropy graphs for the sinusoidal fold show interesting results. In Fig. 4.13b, the AEH values with respect to limb angle are not consistently placed between the Voigt and Reuss bounds. While the AEH anisotropies of *qP* are closer to the Reuss through almost all the limb angles, the *qS1* AEH values are closer to the Reuss until $\theta = 60°$ (crossover limb angle of sinusoidal fold) and after its θ_c, to the Voigt anisotropies. However, the differences of the AEH anisotropies in all the seismic waves from the Voigt or Reuss are far smaller than the first-order anisotropy variations due to folding. The AEH *qP* and *qS1* anisotropies have maximum differences, respectively, of ~0.60% and ~0.82% from the Voigt, and ~0.08% and ~0.76% from the Reuss (Fig. 4.13b).

The comparisons of seismic velocities and anisotropies between the three bounds reemphasize that the Voigt and Reuss estimates for EM_S are quite close to the precise AEH solution and hence provide reliable results.

4.7.2. Natural Fold Geometries

Folds are very common geological structures developed at a variety of scales and depths and in varied tectonic settings. Geologists have investigated their geometries and formation mechanisms for a long time to obtain information on rheology, strain, kinematics, and deformation history in ancient and modern orogenic belts from the foreland fold-and-thrust belt to high-grade metamorphic rocks of the central crystalline core complex, and natural fold examples are found in their literature and textbooks (e.g., Ramsay, 1967; Ramsay and Huber, 1987; references within Hudleston and Treagus, 2010; Poblet and Lisle, 2011; Bastida et al., 2014). Fold structures are also recognized in ductile shear zones (e.g., Carreras et al., 2005) and in extensional tectonic settings (e.g., Harris et al., 2002). However, it is not straightforward to predict natural fold geometry based on tectonic settings or locations, since inhomogeneous rheology and strain form various structures from consistently oriented rocks with foliation to complex fold structures.

Recently, a few studies quantified geometries of natural folds in greenschist and amphibolite facies rocks from the ancient Variscan orogenic belt of Europe (Baratoux et al., 2005; Bastida et al., 2010) and turbidites from the Pyrenees of the Alpine orogenic belt (Bastida et al., 2012). Those folds mainly range from chevron to parabolic shape, based on area balance and Fourier harmonic analyses (e.g., Bastida et al., 1999; Bastida et al., 2005), and their limb angles mostly show 40° to 80° (inferred from aspect ratio and interlimb angle data). The natural folds are rarely upright symmetric as described in the previous sections, which may be found in an initial stage of buckle folding, but inclined to recumbent or plunged. In such a case, their EM_S can be obtained by simple transformation of bulk stiffness tensors calculated for upright symmetric folds. If rock layers are not parallel to the principle shortening direction, or shearing deformation is involved, then asymmetric folds can be developed (e.g., Treagus, 1973; Anthony and Wickham, 1978; Carreras et al., 2005; Aller et al., 2010). Practically, both fold asymmetry and inclined axial surfaces are common in nature. We analyze geometry and seismic velocities of simple asymmetric cylindrical folds in section 4.7.2.1 below.

Meso- and macro-scale folds of mica-rich rocks in the middle crust often have complex structures at microscopic scale, for instance, asymmetric and symmetric microfolds (crenulation cleavage) in the limb and hinge area, respectively, of the large-scale folds, since the folding is accommodated by internal deformation such as dissolution-precipitation (e.g., Williams et al., 2001; Naus-Thijssen et al., 2011a). To get EM_S of such large-scale folds using the methodology in the present study, elastic properties of local rocks distributed throughout the folds may need to be averaged for the representative rock stiffness.

Another consideration to investigate natural fold seismic anisotropy is non-cylindrical folds such as superimposed folds. Two generations of folds may form during a continuous deformation or during two periods of deformation separated by a large time interval (e.g., Ramsay, 1967, chapter 10; Simón, 2004). Okaya et al. (2018) provided an example of doubly-plunging folds, their 3-D mathematical expressions and seismic property results.

4.7.2.1. Asymmetric Cylindrical Folds

This section introduces simple periodic asymmetric fold geometries with planar enveloping surfaces (Fig. 4.14a). They can be generated by shearing a symmetric cylindrical fold, but the resulting geometries may be used in asymmetric folds with same morphology caused by other mechanisms for a seismic anisotropy analysis. A degree of fold asymmetry is measured by angular shear strain (ψ), called tilt angle here, ranging between −90° and 90° (Fig. 4.14a). When $\psi > 45°$ or $\psi < -45°$, the asymmetric fold is overturned. New rotation angle (ϕ') between the rock symmetry axes and the asymmetric fold reference frame is a function of ψ and ϕ (old rotation angle in symmetric fold):

$$\phi'(x) = \arctan\left(\frac{\tan\phi(x)}{1+\tan\psi\tan\phi(x)}\right); \qquad -180° < \phi' < 180° \tag{40}$$

where $\phi(x)$ is from equation (10). Thus, the direction cosine matrix in the asymmetric cylindrical fold is as follows:

$$a_{ij}(x,y,z) = a_{ij}(x) = \begin{bmatrix} \cos\phi'(x) & 0 & -\sin\phi'(x) \\ 0 & 1 & 0 \\ \sin\phi'(x) & 0 & \cos\phi'(x) \end{bmatrix} \tag{41}$$

We numerically compute the Voigt EM_S of asymmetric folds with specific tilt angles (ψ = 30°, 45°, 60°, 75°) made from all types of original symmetric fold at θ = 45°, due to their complex geometries. Fig. 4.14b illustrates the geometries and seismic velocities of the asymmetric sinusoidal folds and the symmetric fold for comparison. With varying ψ, the seismic anisotropy and the minimum velocity direction are changed. Additionally, the asymmetric fold volumes no longer represent orthorhombic but monoclinic velocity patterns, although the same hexagonal internal rock is used. In the bottom row of Fig. 4.14b, while the velocity graph in the *x*-*z* plane of the symmetric fold is symmetrical with respect to γ of 45° (orthorhombic), the asymmetric velocity graphs do not have any line of symmetry in the *x*-*z* plane. Other types of asymmetric folds are shown in Fig. 4.15.

Figure 4.14. Design of asymmetric fold geometry and seismic velocities for the Voigt EM_S of single-layered asymmetric sinusoidal folds. (a) Simple periodic asymmetric fold made by shearing a symmetric cylindrical fold. Depending on the tilt angle (ψ), degree of fold asymmetry and new rotation angle (ϕ') are determined. (b) Geometry and 3-D seismic velocity of quasi-*P* wave (qV_P) (top row) and 2-D velocity plot with propagation angle γ in the *x*-*z* plane (bottom row) with specific tilt angles (ψ = 30°, 45°, 60° and 75°) made from symmetric sinusoidal fold at a limb angle (e.g., θ = 45°). Two limb angles (θ'_1 and θ'_2) of asymmetric fold are provided. The original symmetric fold geometry and seismic results are shown in the leftmost column for comparison. Note that the asymmetric fold EM_S exhibit monoclinic symmetry.

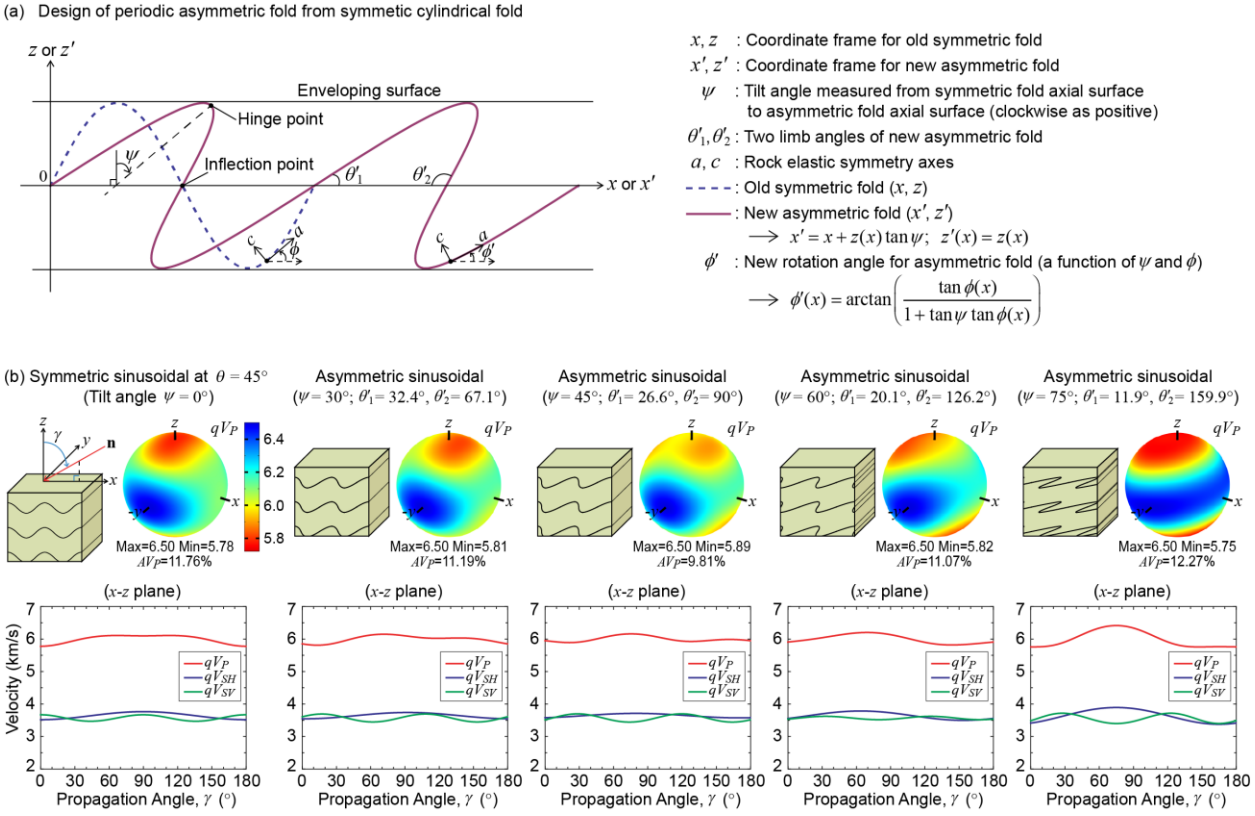

Figure 4.15. Seismic velocity plot for the Voigt EM_S of single-layered asymmetric folds. 3-D seismic velocity of quasi-*P* wave (qV_P) (top row) and 2-D velocity plot with propagation angle γ in the *x*-*z* plane (bottom row) are plotted for asymmetric (a) cuspate (m = 0.5), (b) chevron, (c) parabolic, and (d) box (m = 3) folds with specific tilt angles (ψ = 30°, 45°, 60° and 75°) made from symmetric sinusoidal fold at a limb angle (e.g., θ = 45°). Two limb angles (θ'_1 and θ'_2) of asymmetric fold are provided. The original symmetric fold geometry and seismic results are shown in the leftmost column for comparison. Note that all the asymmetric fold EM_S exhibit monoclinic symmetry. While the velocity graph in the *x*-*z* plane of the symmetric fold is symmetrical with respect to γ of 45° (orthorhombic), the asymmetric velocity graphs do not have any line of symmetry in the *x*-*z* plane.

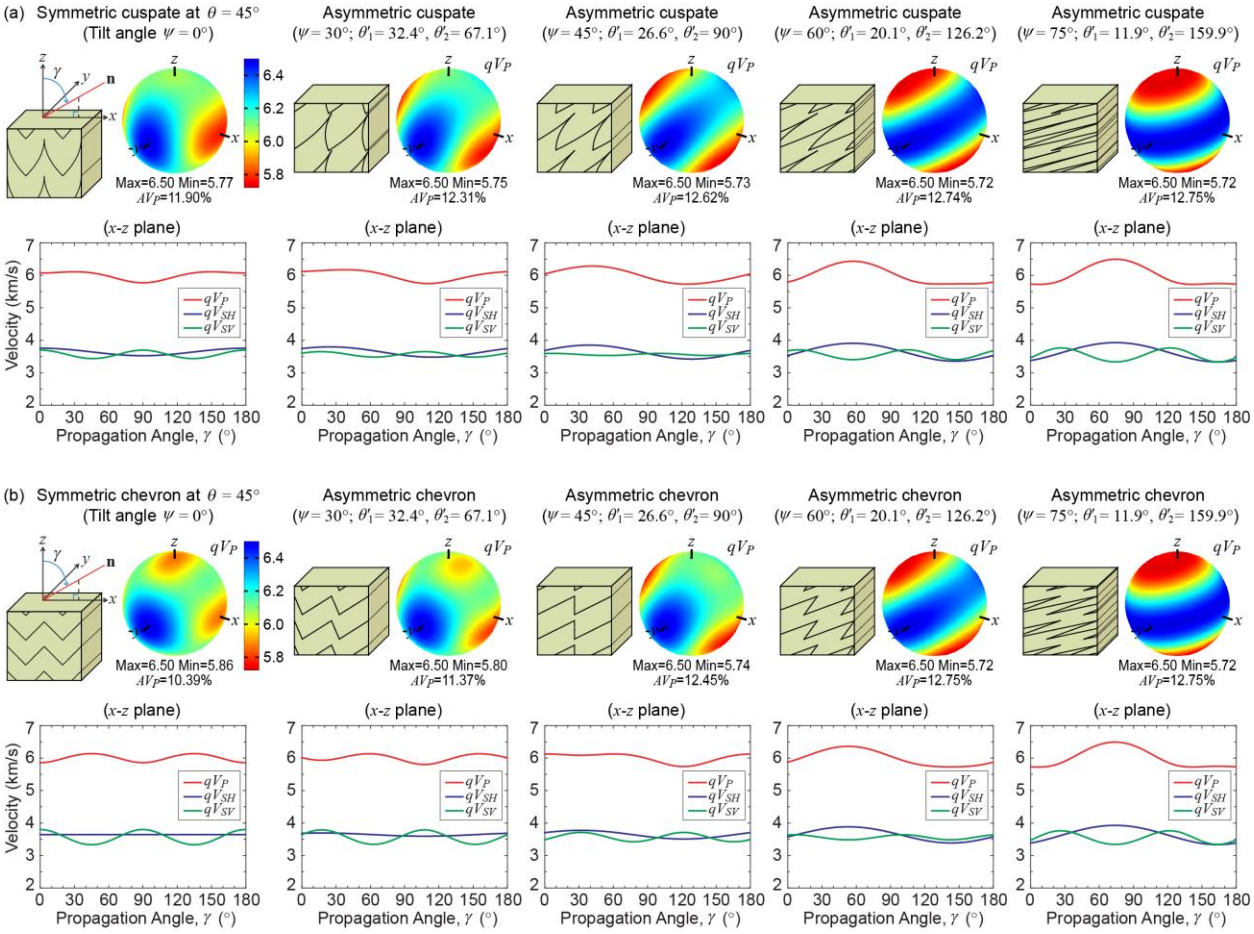

Figure 4.15. (continued)

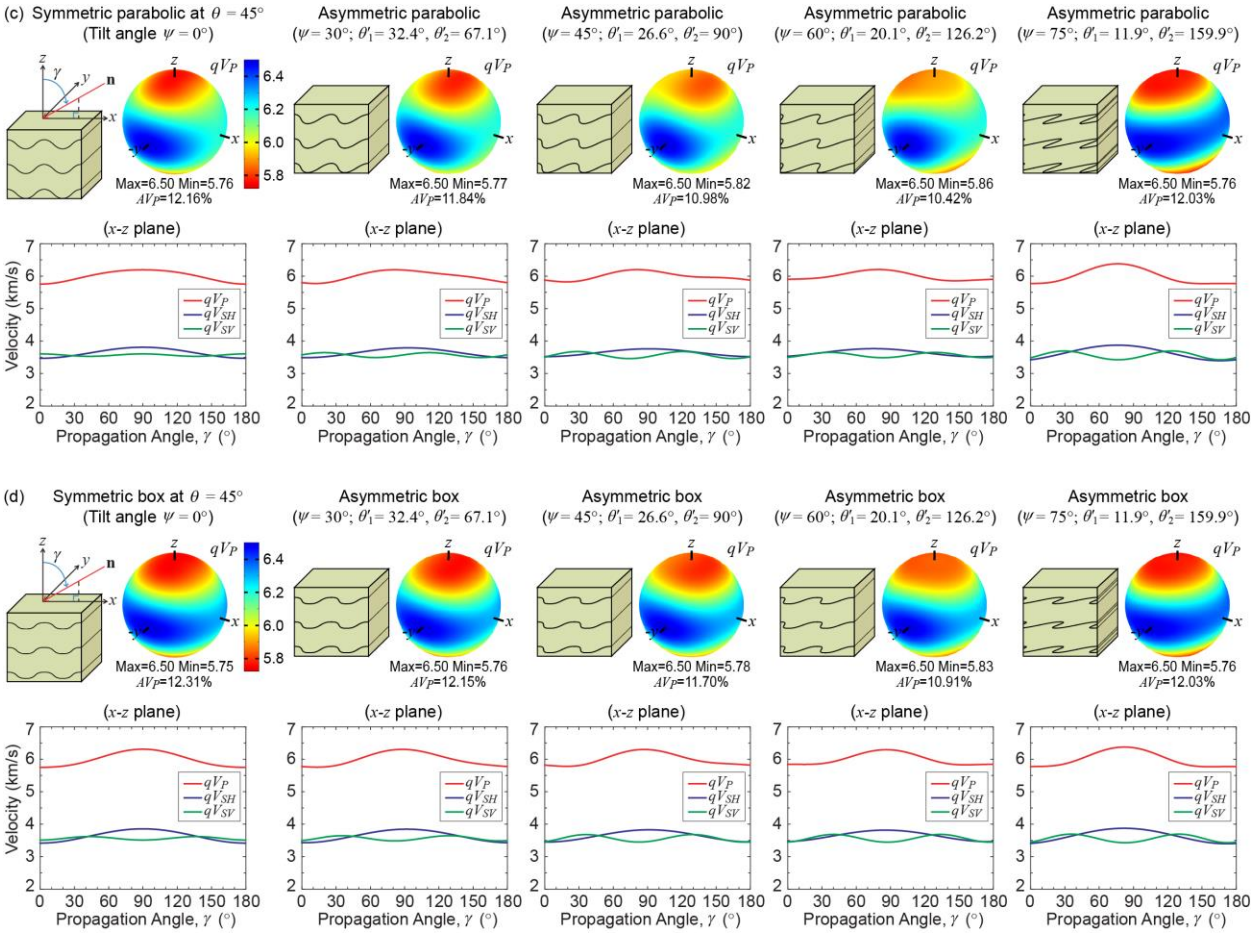

4.7.3. EM_S for Multi-Layered Cylindrical Folds

Thus far, the EM_S stiffness tensors have been computed for single-layered folds (Fig. 4.1a). It has been well known for decades that stacked isotropic or anisotropic thin layers produce another anisotropic property (e.g., Backus, 1962; Levshin and Ratnikova, 1984; Schoenberg and Muir, 1989). Given that the crust is a layered medium, multi-layered folds are very common. Let me consider a cylindrical fold with multiple layers (Fig. 4.1c) where the representative rock of each layer can have different elastic stiffness. One solution for EM_S stiffness tensors of the multi-layered fold is to first obtain the representative rock stiffness incorporating all the layers, and then use the same **SGO** tensors as the single-layered folds. As illustrated in Figs 4.1c and 4.16, we assume that a multi-layered cylindrical fold consists of two kinds of

layers (Layer 1 and Layer 2) with different representative rock stiffness ($\mathbf{C}^{\mathbf{rep}}_{\mathbf{L1}}$ and $\mathbf{C}^{\mathbf{rep}}_{\mathbf{L2}}$) and the thickness of layers (l) is much smaller than the seismic wavelength. Now the representative rock of the multiple layers ($\mathbf{C}^{\mathbf{repm}}$) in Fig. 4.16b can be treated as a finely layered, horizontally stratified, elastic medium. Homogenization techniques for stiffness calculation of a finely layered medium are presented by Backus (1962) in the case of isotropic or transversely isotropic (hexagonal) symmetry with vertical symmetry axis (called the "Backus average") and by Schoenberg and Muir (1989) in the case of generally anisotropic symmetry. Alternatively, the homogenized representative rock stiffness ($\mathbf{C}^{\mathbf{repm}}$) of multiple layers for all the cases can be obtained numerically via the AEH method (e.g., Vel and Goupee, 2010; Naus-Thijssen et al., 2011a; Vel et al., 2016). Once the $\mathbf{C}^{\mathbf{repm}}$ incorporating the multiple layers is obtained, the bulk elastic stiffness ($\mathbf{C^*}$) of the multi-layered EM_S can be computed using the same **SGO** tensors as the single-layered folds (e.g., equation (22) for the Voigt estimate). For instance, a multi-layered sinusoidal fold consists of schist (Layer 1; e.g., the Haast schist) and gneiss (Layer 2; e.g., the Nanga Parbat gneiss from Okaya and Christensen (2002)) with same volume fraction, and we want to know the *qP* seismic anisotropy of the fold with limb angle of 45°. Since the Haast schist in Layer 1 and the Nanga Parbat gneiss in Layer 2 have hexagonal symmetry (Okaya and Christensen, 2002), the homogenized $\mathbf{C}^{\mathbf{repm}}$ of the two layers by the Backus average also has hexagonal symmetry (Figs 4.17a, 4.17b, and 4.17c). Using the $\mathbf{C}^{\mathbf{repm}}$ and the sinusoidal **SGO** for the Voigt (equation (26)), the fold EM_S with limb angle of 45° can be easily calculated, and thus its *qP* seismic anisotropy (7.24%) for the Voigt bound is obtained (Fig. 4.17d).

Figure 4.16. Multi-layered fold and its representative rock. Schematic diagrams show (a) the structural effective medium (EM_S) and (b) the selected representative rock ($\mathbf{C}^{\mathbf{repm}}$) for the multi-layered cylindrical fold of Fig. 4.1c in the profile plane. The fold consists of two kinds of layers (Layer 1 and Layer 2) with different representative rock stiffness ($\mathbf{C}^{\mathbf{rep}}_{\mathbf{L1}}$ and $\mathbf{C}^{\mathbf{rep}}_{\mathbf{L2}}$). The thickness of layers (l) is assumed to be much smaller than the seismic wavelength to calculate the $\mathbf{C}^{\mathbf{repm}}$ using homogenization techniques. The local rock symmetry axes (a-b-c) and the geographical frame (x-y-z) are also illustrated.

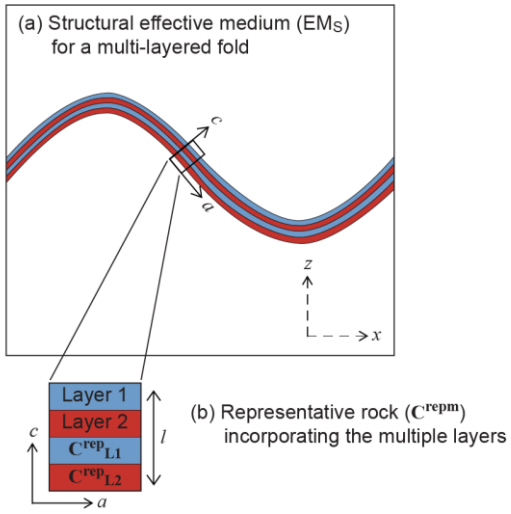

Figure 4.17. Example of strategy to obtain a multi-layered fold EM_S with a specific limb angle (e.g., θ = 45°). Seismic velocity (qV_P) and anisotropy (AV_P) are shown at each step. From (a) Layer 1 of the Haast schist and (b) Layer 2 of the Nanga Parbat gneiss (Okaya and Christensen, 2002), (c) the homogenized representative rock stiffness ($\mathbf{C}^{\mathbf{repm}}$) incorporating the two layers can be computed via the Backus average (Backus, 1962) since all the layers have hexagonal symmetry. And then (d) the EM_S of the multi-layered fold can be obtained from (c) using the same **SGO** as for single-layered folds. In (d), the Voigt EM_S velocity result for sinusoidal fold at θ = 45° is presented as an example. Shear wave splitting (δt) results at all the steps are also provided in the bottom row.

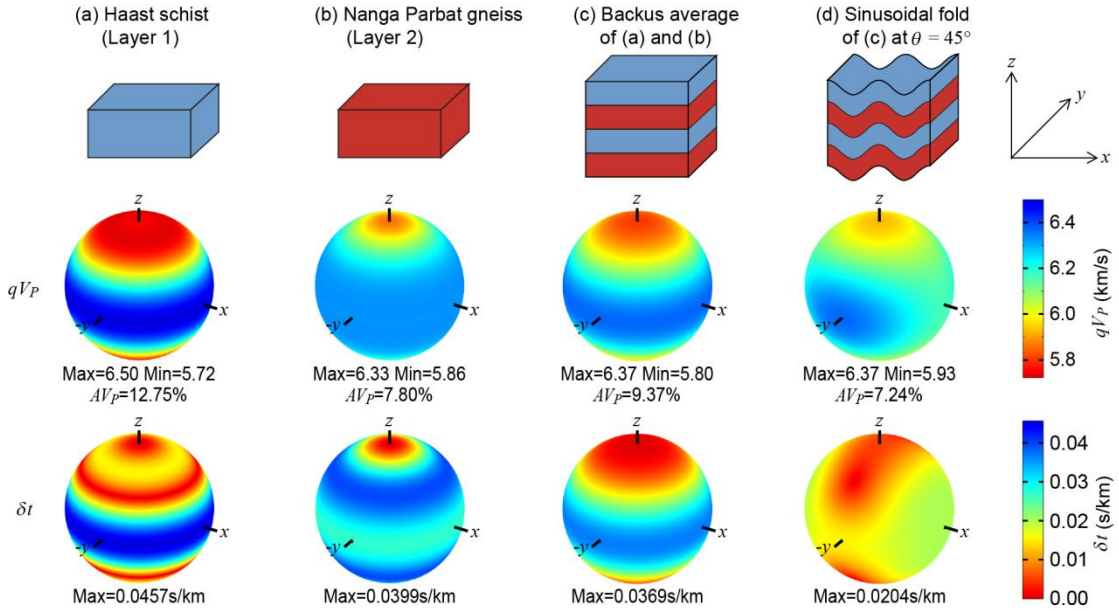

4.7.4. Work Flow for EM_S Analysis and Associated Uncertainties

The EM_S analysis intrinsically involves multiscale homogenization (approximation) and hence cumulative uncertainties from microscale fabric heterogeneity to larger-scale structure. Fig. 4.18 shows a flow diagram for the multiscale analysis of fold EM_S and highlights possible sources of uncertainty. To calculate bulk stiffness tensors of polycrystalline rocks at hand-specimen or thin-section scales (Fig. 4.18a), two types of approaches are widely used: petrophysical measurements, and fabric (e.g., LPO) measurements using X-ray/neutron diffraction or EBSD. Petrophysical measurements produce a single value of the bulk rock stiffness under specific pressure and temperature, but it is relatively challenging to measure full 3-D seismic properties especially for low symmetry rocks. On the other hand, the thin-section-based approaches can estimate bulk elastic properties of any symmetry rocks from single crystals, but the resulting values are dependent on homogenization methods for arriving at a bulk stiffness tensor.

There are cases in which homogenized properties of same polycrystalline rocks are quite different between the Voigt (1928) and Reuss (1929) estimates. For instance, highly anisotropic rocks such as mica schists can show a large difference more than 1 km/s in seismic velocity between the two bounds (e.g., Mainprice and Humbert, 1994; Naus-Thijssen et al., 2011a). This is because the rocks do not have uniform stress and strain fields due to heterogeneous microstructure and elastically anisotropic grains. Thus, it is important to determine an appropriate homogenization technique to compute a reasonable bulk stiffness for a specific rock at the sample scale. The AEH-finite element method explicitly considers cumulative effects of grain-scale elastic interactions throughout the heterogeneous rock, incorporating the effects of LPO, grain size, shape, shape-preferred orientation and spatial arrangement of grains. Naus-Thijssen et al. (2011a) provided methodologies for determining rock elastic properties using the AEH method coupled with EBSD data. Using precise methods such as AEH can reduce the uncertainty that arises from averaging techniques for the bulk rock stiffness at micro to mesoscales, especially for highly anisotropic rocks.

We have assumed that a fold structure has relatively uniform rock type throughout the fold volume, so that a local rock stiffness tensor (**C**), determined from petrophysical laboratory or thin-section methods, could be used as a representative rock stiffness tensor ($\mathbf{C}^{\mathbf{rep}}$) (e.g., equations (13) and (21)). However, there would be situations when the local rock variation is considerable along the fold. For instance, when foliated or finely laminated rocks are folded, small-scale folds and crenulation cleavage may form in the hinge area and its rock stiffness could be markedly different from the more planar foliated limb (e.g., Naus-Thijssen et al., 2011a). In such a case, an appropriate homogenization strategy is required to obtain the representative rock stiffness from variable local rocks (Fig. 4.18b).

In multi-layered folds, assuming that $\mathbf{C}^{\mathbf{rep}}$ of each layer is appropriately obtained using the methods in Figs 4.18a and 4.18b, an accurate homogenized representative rock stiffness of the multiple layers ($\mathbf{C}^{\mathbf{repm}}$) may be computed as discussed in section 4.7.3 (Fig. 4.18c).

In computing the bulk fold EM_S (**C***), the separation of geometry (**SGO)** from rock property ($\mathbf{C}^{\mathbf{rep}}$) allows us to efficiently investigate the variations of fold seismic properties depending on its geometry

(e.g., fold type and limb angle) regardless of the rock type (Fig. 4.18d). This approach will greatly reduce computational time of a number of EM_S with various fold geometries compared with time-intensive numerical methods such as AEH (see section 4.3.3.3). It is also possible to explore various types of representative rocks if the fold morphology is known. Although my approximations for EM_S using the Voigt and Reuss methods produce uncertainties, the differences between the upper and lower bounds are minor relative to the limb angle variation (Figs 4.12 and 4.13). Interestingly, the fold EM_S uncertainty (e.g., up to ~0.07 km/s; Fig. 4.12) arising from different averaging methods is considerably smaller than the rock EM uncertainty (e.g., up to ~1 km/s in highly anisotropic rocks; see Mainprice and Humbert (1994) and Naus-Thijssen et al. (2011a)).

Lastly, we have used the effective medium theory for predicting the bulk fold elastic properties assuming that the size of the structural heterogeneity (L) is much smaller that the seismic wavelength (λ) (Fig. 4.1). However, the influence of various seismic wavelengths from the scattering regime to the effective medium would be an interesting topic for further investigation.

Figure 4.18. Flow diagram for multiscale analysis of the fold EM_S. (a) to (d) indicate homogenization for effective medium (EM) at each scale and possible sources of uncertainty (gray boxes). See the text in section 4.7.4 for details.

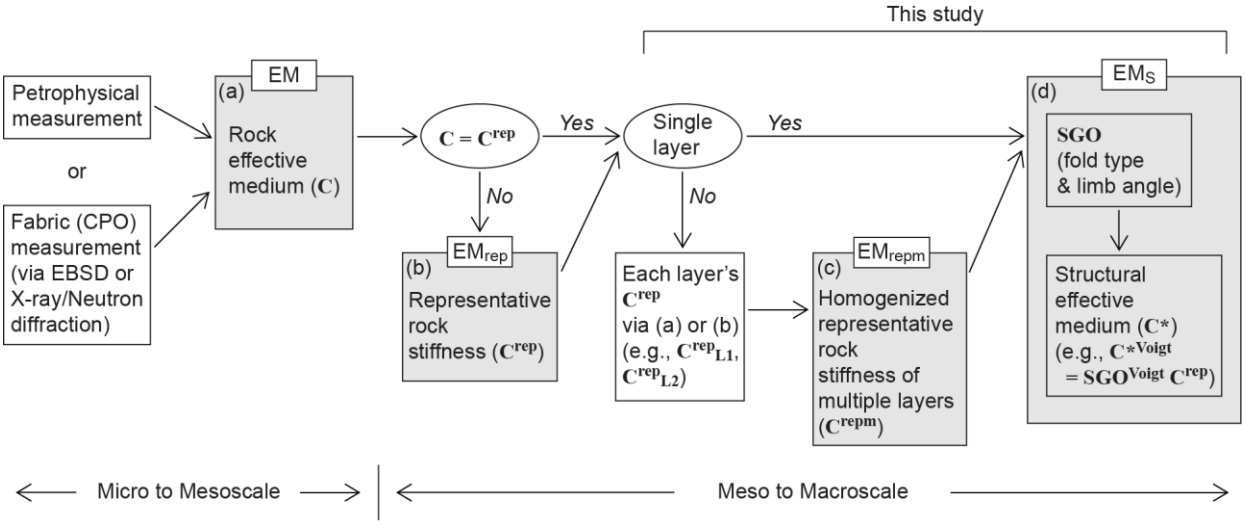

4.8. Conclusions and Implications

(4) New tensor formulations via the Voigt and Reuss averages are presented for calculating bulk stiffness tensors (structural effective medium, or EM_S) of single-layered macroscale folds that can modify (rotate) intrinsic rock fabric. The formulations effectively highlight the influence of the macroscale geometries on seismic properties by defining a structural geometry operator (**SGO**) which is solely dependent on the geometry and separated from the constituent rock stiffness tensor.

(5) The **SGO** can be analytically or numerically computed if a structure of interest can be expressed mathematically. For idealized cylindrical folds (sinusoidal, chevron, parabolic, box and cuspate), the **SGO** is a function of both limb angle and hinge shape, and in turn the velocity and anisotropy of seismic waves propagating through the folds vary with different limb angle and fold type even if they are comprised of the same rock.

(6) Seismic waves propagating through the cylindrical folds in different directions show different velocity patterns. Consequently, the comparison of real seismic observables to my model results may provide information about folding at depth and therefore on the kinematics of crustal deformation.

(7) Seismic anisotropies for quasi-*P* and fast quasi-*S* waves decrease approaching the crossover limb angle (θ_c) at which the horizontal and vertical stiffnesses for a cylindrical fold are equal, and the θ_c for each fold type increases with decreasing hinge curvature; for example, θ_c of chevron and sinusoidal folds are 45° and 60°, respectively. This indicates that the fold seismic anisotropy is strongly affected by limb angle and hinge shape.

(8) In instances where the local rock has hexagonal (or transversely isotropic) symmetry, the calculated EM_S for the symmetric cylindrical folds range from tetragonal to orthorhombic symmetry depending on limb angle, and the asymmetric folds exhibit monoclinic symmetry. When the folds display tetragonal symmetry at their θ_c, the seismic anisotropies are effectively muted, for example, decreased by ~19% to 35% of the original rock anisotropy of the Haast schist in quasi-*P* wave. This implies the possibility of further muted seismic anisotropy for non-cylindrical folds such as superimposed folds with different shortening directions.

(9) Fold EM_S from the two different averaging techniques (Voigt and Reuss) show only minor variances compared with that caused by fold morphology changes, and are considerably close to a precise numerical solution such as asymptotic expansion homogenization. This indicates that my approach is efficient and valuable for exploring the influence of various fold geometries on seismic velocity and anisotropy in varied tectonic settings.

(10) A more complete understanding of crustal seismic anisotropy modified by natural folds might help better interpret mantle dynamics based on teleseismic waves passing through orogenic belts where crustal thickening occurs.

4.9. Supporting Information

The supporting information contains the Voigt and Reuss **SGO**s of folds filled with an orthorhombic symmetry rock.

4.9.1. SGO^{Voigt} for Folds Made of Rocks with Orthorhombic Symmetry

This section describes the analytical **SGO** matrices for single-layered sinusoidal, chevron and parabolic folds using the Voigt method when the representative rock ($\mathbf{C}^{\mathbf{rep}}$) has orthorhombic symmetry with 9 independent components. The resulting fold EM_S stiffness ($\mathbf{C}^{*\mathbf{Voigt}}$) also exhibits orthorhombic symmetry. This relationship (equation (24)) can be written in column vector forms as follows:

$$\begin{Bmatrix} C_{11}^{*Voigt} \\ C_{12}^{*Voigt} \\ C_{13}^{*Voigt} \\ C_{22}^{*Voigt} \\ C_{23}^{*Voigt} \\ C_{33}^{*Voigt} \\ C_{44}^{*Voigt} \\ C_{55}^{*Voigt} \\ C_{66}^{*Voigt} \end{Bmatrix} = [SGO^{Voigt}] \begin{Bmatrix} C_{11}^{rep} \\ C_{12}^{rep} \\ C_{13}^{rep} \\ C_{22}^{rep} \\ C_{23}^{rep} \\ C_{33}^{rep} \\ C_{44}^{rep} \\ C_{55}^{rep} \\ C_{66}^{rep} \end{Bmatrix} \tag{42}$$

The **SGO** matrix is of dimension 9×9.

For sinusoidal folds defined by the sine wave function (equation (1)), the **SGO** matrix is

$$[SGO^{Voigt}]_{sinusoidal} =$$

$$\begin{bmatrix}
\frac{B+1}{D^3} & 0 & \frac{2B}{D^3} & 0 & 0 & \frac{B(2D-3)+D-1}{D^3} & 0 & \frac{4B}{D^3} & 0 \\
0 & \frac{1}{D} & 0 & 0 & 1-\frac{1}{D} & 0 & 0 & 0 & 0 \\
\frac{B}{D^3} & 0 & 1-\frac{2B}{D^3} & 0 & 0 & \frac{B}{D^3} & 0 & -\frac{4B}{D^3} & 0 \\
0 & 0 & 0 & 1 & 0 & 0 & 0 & 0 & 0 \\
0 & 1-\frac{1}{D} & 0 & 0 & \frac{1}{D} & 0 & 0 & 0 & 0 \\
\frac{B(2D-3)+D-1}{D^3} & 0 & \frac{2B}{D^3} & 0 & 0 & \frac{B+1}{D^3} & 0 & \frac{4B}{D^3} & 0 \\
0 & 0 & 0 & 0 & 0 & 0 & \frac{1}{D} & 0 & 1-\frac{1}{D} \\
\frac{B}{D^3} & 0 & -\frac{2B}{D^3} & 0 & 0 & \frac{B}{D^3} & 0 & 1-\frac{4B}{D^3} & 0 \\
0 & 0 & 0 & 0 & 0 & 0 & 1-\frac{1}{D} & 0 & \frac{1}{D}
\end{bmatrix} \quad (43)$$

where *B* and *D* are non-dimensional parameters defined as $B = (1/2)\tan^2\theta$ and $D = \sqrt{1+\tan^2\theta}$, and θ is the limb angle.

The **SGO** matrix of chevron folds, which are described by the power function with *m* = 1 (equations (3), (4), (5) and (6)), is as follows:

$$[SGO^{Voigt}]_{chevron} = \begin{bmatrix}
c^4 & 0 & 2c^2s^2 & 0 & 0 & s^4 & 0 & 4c^2s^2 & 0 \\
0 & c^2 & 0 & 0 & s^2 & 0 & 0 & 0 & 0 \\
c^2s^2 & 0 & c^4+s^4 & 0 & 0 & c^2s^2 & 0 & -4c^2s^2 & 0 \\
0 & 0 & 0 & 1 & 0 & 0 & 0 & 0 & 0 \\
0 & s^2 & 0 & 0 & c^2 & 0 & 0 & 0 & 0 \\
s^4 & 0 & 2c^2s^2 & 0 & 0 & c^4 & 0 & 4c^2s^2 & 0 \\
0 & 0 & 0 & 0 & 0 & 0 & c^2 & 0 & s^2 \\
c^2s^2 & 0 & -2c^2s^2 & 0 & 0 & c^2s^2 & 0 & (c^2-s^2)^2 & 0 \\
0 & 0 & 0 & 0 & 0 & 0 & s^2 & 0 & c^2
\end{bmatrix} \quad (44)$$

where *c* and *s* are non-dimensional parameters defined as $c = \cos\theta$ and $s = \sin\theta$, and θ is the limb angle.

In the case of parabolic folds described by the power function with *m* = 2 (equations (3), (4), (5) and (6)), the **SGO** matrix is given by

$$[SGO^{Voigt}]_{parabolic} =$$

$$\begin{bmatrix}
\frac{c(cs+\theta)}{2s} & 0 & \frac{c(-cs+\theta)}{s} & 0 & 0 & 1+\frac{c(cs-3\theta)}{2s} & 0 & \frac{2c(-cs+\theta)}{s} & 0 \\
0 & \frac{c\theta}{s} & 0 & 0 & 1-\frac{c\theta}{s} & 0 & 0 & 0 & 0 \\
\frac{c(-cs+\theta)}{2s} & 0 & 1+\frac{c(cs-\theta)}{s} & 0 & 0 & \frac{c(-cs+\theta)}{2s} & 0 & \frac{2c(cs-\theta)}{s} & 0 \\
0 & 0 & 0 & 1 & 0 & 0 & 0 & 0 & 0 \\
0 & 1-\frac{c\theta}{s} & 0 & 0 & \frac{c\theta}{s} & 0 & 0 & 0 & 0 \\
1+\frac{c(cs-3\theta)}{2s} & 0 & \frac{c(-cs+\theta)}{s} & 0 & 0 & \frac{c(cs+\theta)}{2s} & 0 & \frac{2c(-cs+\theta)}{s} & 0 \\
0 & 0 & 0 & 0 & 0 & 0 & \frac{c\theta}{s} & 0 & 1-\frac{c\theta}{s} \\
\frac{c(-cs+\theta)}{2s} & 0 & \frac{c(cs-\theta)}{s} & 0 & 0 & \frac{c(-cs+\theta)}{2s} & 0 & 1+\frac{2c(cs-\theta)}{s} & 0 \\
0 & 0 & 0 & 0 & 0 & 0 & 1-\frac{c\theta}{s} & 0 & \frac{c\theta}{s}
\end{bmatrix} \quad (45)$$

where c and s are non-dimensional parameters defined as $c = \cos\theta$ and $s = \sin\theta$, and θ is the limb angle in radians.

4.9.2. $\mathbf{SGO^{Reuss}}$ for Folds Made of Rocks with Orthorhombic Symmetry

This section describes the analytical **SGO** matrices for single-layered sinusoidal, chevron and parabolic folds using the Reuss method when the representative rock compliance tensor ($\mathbf{S^{rep}}$) has orthorhombic symmetry with 9 independent components, the **SGO** matrix for the compliance is of dimension 9×9, and equation (33) can be written in column vector forms as follows:

$$\begin{Bmatrix}
S_{11}^{*Reuss} \\ S_{12}^{*Reuss} \\ S_{13}^{*Reuss} \\ S_{22}^{*Reuss} \\ S_{23}^{*Reuss} \\ S_{33}^{*Reuss} \\ S_{44}^{*Reuss} \\ S_{55}^{*Reuss} \\ S_{66}^{*Reuss}
\end{Bmatrix} = [SGO^{Reuss}] \begin{Bmatrix}
S_{11}^{rep} \\ S_{12}^{rep} \\ S_{13}^{rep} \\ S_{22}^{rep} \\ S_{23}^{rep} \\ S_{33}^{rep} \\ S_{44}^{rep} \\ S_{55}^{rep} \\ S_{66}^{rep}
\end{Bmatrix} \quad (46)$$

Each $\mathbf{SGO^{Reuss}}$ for chevron, sinusoidal and parabolic folds is as follows

$$[SGO^{Reuss}]_{sinusoidal} =$$

$$\begin{bmatrix}
\frac{B+1}{D^3} & 0 & \frac{2B}{D^3} & 0 & 0 & \frac{B(2D-3)+D-1}{D^3} & 0 & \frac{B}{D^3} & 0 \\
0 & \frac{1}{D} & 0 & 0 & 1-\frac{1}{D} & 0 & 0 & 0 & 0 \\
\frac{B}{D^3} & 0 & 1-\frac{2B}{D^3} & 0 & 0 & \frac{B}{D^3} & 0 & -\frac{B}{D^3} & 0 \\
0 & 0 & 0 & 1 & 0 & 0 & 0 & 0 & 0 \\
0 & 1-\frac{1}{D} & 0 & 0 & \frac{1}{D} & 0 & 0 & 0 & 0 \\
\frac{B(2D-3)+D-1}{D^3} & 0 & \frac{2B}{D^3} & 0 & 0 & \frac{B+1}{D^3} & 0 & \frac{B}{D^3} & 0 \\
0 & 0 & 0 & 0 & 0 & 0 & \frac{1}{D} & 0 & 1-\frac{1}{D} \\
\frac{4B}{D^3} & 0 & -\frac{8B}{D^3} & 0 & 0 & \frac{4B}{D^3} & 0 & 1-\frac{4B}{D^3} & 0 \\
0 & 0 & 0 & 0 & 0 & 0 & 1-\frac{1}{D} & 0 & \frac{1}{D}
\end{bmatrix} \quad (47)$$

where B and D are non-dimensional parameters defined as $B = (1/2)\tan^2\theta$ and $D = \sqrt{1+\tan^2\theta}$, and θ is the limb angle.

$$[SGO^{Reuss}]_{chevron} = \begin{bmatrix}
c^4 & 0 & 2c^2s^2 & 0 & 0 & s^4 & 0 & c^2s^2 & 0 \\
0 & c^2 & 0 & 0 & s^2 & 0 & 0 & 0 & 0 \\
c^2s^2 & 0 & c^4+s^4 & 0 & 0 & c^2s^2 & 0 & -c^2s^2 & 0 \\
0 & 0 & 0 & 1 & 0 & 0 & 0 & 0 & 0 \\
0 & s^2 & 0 & 0 & c^2 & 0 & 0 & 0 & 0 \\
s^4 & 0 & 2c^2s^2 & 0 & 0 & c^4 & 0 & c^2s^2 & 0 \\
0 & 0 & 0 & 0 & 0 & 0 & c^2 & 0 & s^2 \\
4c^2s^2 & 0 & -8c^2s^2 & 0 & 0 & 4c^2s^2 & 0 & (c^2-s^2)^2 & 0 \\
0 & 0 & 0 & 0 & 0 & 0 & s^2 & 0 & c^2
\end{bmatrix} \quad (48)$$

$$[SGO^{Reuss}]_{parabolic} =$$

$$\begin{bmatrix}
\frac{c(cs+\theta)}{2s} & 0 & \frac{c(-cs+\theta)}{s} & 0 & 0 & 1+\frac{c(cs-3\theta)}{2s} & 0 & \frac{c(-cs+\theta)}{2s} & 0 \\
0 & \frac{c\theta}{s} & 0 & 0 & 1-\frac{c\theta}{s} & 0 & 0 & 0 & 0 \\
\frac{c(-cs+\theta)}{2s} & 0 & 1+\frac{c(cs-\theta)}{s} & 0 & 0 & \frac{c(-cs+\theta)}{2s} & 0 & \frac{c(cs-\theta)}{2s} & 0 \\
0 & 0 & 0 & 1 & 0 & 0 & 0 & 0 & 0 \\
0 & 1-\frac{c\theta}{s} & 0 & 0 & \frac{c\theta}{s} & 0 & 0 & 0 & 0 \\
1+\frac{c(cs-3\theta)}{2s} & 0 & \frac{c(-cs+\theta)}{s} & 0 & 0 & \frac{c(cs+\theta)}{2s} & 0 & \frac{c(-cs+\theta)}{2s} & 0 \\
0 & 0 & 0 & 0 & 0 & 0 & \frac{c\theta}{s} & 0 & 1-\frac{c\theta}{s} \\
\frac{2c(-cs+\theta)}{s} & 0 & \frac{4c(cs-\theta)}{s} & 0 & 0 & \frac{2c(-cs+\theta)}{s} & 0 & 1+\frac{2c(cs-\theta)}{s} & 0 \\
0 & 0 & 0 & 0 & 0 & 0 & 1-\frac{c\theta}{s} & 0 & \frac{c\theta}{s}
\end{bmatrix} \quad (49)$$

where c and s are non-dimensional parameters defined as $c = \cos\theta$ and $s = \sin\theta$, and θ is the limb angle in radians.

REFERENCES

Aller, J., Bobillo-Ares, N.C., Bastida, F., Lisle, R.J., Menéndez, C.O., 2010. Kinematic analysis of asymmetric folds in competent layers using mathematical modelling. Journal of Structural Geology 32, 1170–1184, doi:10.1016/j.jsg.2010.07.008.

Anders, M.H., Laubach, S.E., Scholz, C.H., 2014. Microfractures: A review. Journal of Structural Geology 69, 377-394, doi:10.1016/j.jsg.2014.05.011.

Andrews, D.J., 2005. Rupture dynamics with energy loss outside the slip zone. Journal of Geophysical Research 110, B01307, doi:10.1029/2004JB003191.

Anthony, M., Wickham, J., 1978. Finite-element simulation of asymmetric folding. Tectonophysics 47, 1–14, doi:10.1016/0040-1951(78)90148-8.

Auld, B.A., 1990. Acoustic Fields and Waves in Solids, Volume 1, 2nd ed. Krieger Publishing Company, Malabar, FL, USA.

Austrheim, H., Dunkel, K.G., Plümper, O., Ildefonse, B., Liu, Y., Jamtveit, B., 2017. Fragmentation of wall rock garnets during deep crustal earthquakes. Science Advances 3, e1602067, doi:10.1126/sciadv.1602067.

Babuška, V., Cara, M., 1991. Seismic Anisotropy in the Earth. Kluwer Academic Publishers, Dordrecht, Netherlands, doi:10.1007/978-94-011-3600-6.

Backus, G.E., 1962. Long-wave elastic anisotropy produced by horizontal layering. Journal of Geophysical Research 67, 4427–4440, doi:10.1029/JZ067i011p04427.

Baratoux, L., Lexa, O., Cosgrove, J.W., Schulmann, K., 2005. The quantitative link between fold geometry, mineral fabric and mechanical anisotropy: as exemplified by the deformation of amphibolites across a regional metamorphic gradient. Journal of Structural Geology 27, 707–730, doi:10.1016/j.jsg.2005.01.001.

Bastida, F., Aller, J., Bobillo-Ares, N.C., 1999. Geometrical analysis of folded surfaces using simple functions. Journal of Structural Geology 21, 729–742, doi:10.1016/S0191-8141(99)00079-6.

Bastida, F., Aller, J., Bobillo-Ares, N.C., Toimil, N.C., 2005. Fold geometry: a basis for their kinematical analysis. Earth-Science Reviews 70, 129–164, doi:10.1016/j.earscirev.2004.11.006.

Bastida, F., Aller, J., Fernández, F.J., Lisle, R.J., Bobillo-Ares, N.C., Menéndez, O., 2014. Recumbent folds: Key structural elements in orogenic belts. Earth-Science Reviews 135, 162–183, doi:10.1016/j.earscirev.2014.05.002.

Bastida, F., Aller, J., Lisle, R.J., Bobillo-Ares, N.C., Menéndez, C.O., 2012. Saw-tooth structures and curved veins related to folds in the south-central Pyrenees (Spain). Journal of Structural Geology 34, 43–53, doi:10.1016/j.jsg.2011.10.009.

Bastida, F., Aller, J., Pulgar, J.A., Toimil, N.C., Fernández, F.J., Bobillo-Ares, N.C., Menéndez, C.O., 2010. Folding in orogens: a case study in the northern Iberian Variscan Belt. Geological Journal 45, 597–622, doi:10.1002/gj.1199.

Behrmann, J.H., 1985. Crystal plasticity and superplasticity in quartzite; A natural example. Tectonophysics 115, 101-129, doi:10.1016/0040-1951(85)90102-7.

Ben-Zion, Y., Peng, Z., Okaya, D., Seeber, L., Armbruster, J.G., Ozer, N., Michael, A.J., Baris, S., Aktar, M., 2003. A shallow fault-zone structure illuminated by trapped waves in the Karadere–Duzce branch of the North Anatolian Fault, western Turkey. Geophysical Journal International 152, 699-717, doi:10.1046/j.1365-246X.2003.01870.x.

Ben-Zion, Y., Sammis, C.G., 2003. Characterization of fault zones. Pure and Applied Geophysics 160, 677-715, doi:10.1007/pl00012554.

Ben-Zion, Y., Sammis, C.G., 2013. Shear heating during distributed fracturing and pulverization of rocks. Geology 41, 139-142, doi:10.1130/G33665.1.

Ben-Zion, Y., Shi, Z., 2005. Dynamic rupture on a material interface with spontaneous generation of plastic strain in the bulk. Earth and Planetary Science Letters 236, 486-496, doi:10.1016/j.epsl.2005.03.025.

Bensoussan, A., Lions, J.-L., Papanicolau, G., 1978. Asymptotic Analysis for Periodic Structures. North-Holland Publishing Company, Amsterdam, Netherlands.

Bestmann, M., Prior, D.J., 2003. Intragranular dynamic recrystallization in naturally deformed calcite marble: diffusion accommodated grain boundary sliding as a result of subgrain rotation recrystallization. Journal of Structural Geology 25, 1597-1613, doi:10.1016/S0191-8141(03)00006-3.

Birch, F., 1961. The velocity of compressional waves in rocks to 10 kilobars, part 2. Journal of Geophysical Research 66, 2199–2224, doi:10.1029/JZ066i007p02199.

Bleibinhaus, F., Gebrande, H., 2006. Crustal structure of the Eastern Alps along the TRANSALP profile from wide-angle seismic tomography. Tectonophysics 414, 51–69, doi:10.1016/j.tecto.2005.10.028.

Bons, P.D., den Brok, B., 2000. Crystallographic preferred orientation development by dissolution–precipitation creep. Journal of Structural Geology 22, 1713–1722, doi:10.1016/S0191-8141(00)00075-4.

Brace, W.F., Kohlstedt, D.L., 1980. Limits on lithospheric stress imposed by laboratory experiments. Journal of Geophysical Research 85, 6248-6252, doi:10.1029/JB085iB11p06248.

Brantley, S.L., Evans, B., Hickman, S.H., Crerar, D.A., 1990. Healing of microcracks in quartz: Implications for fluid flow. Geology 18, 136-139, doi:10.1130/0091-7613(1990)018<0136:HOMIQI>2.3.CO;2.

Capdeville, Y., Guillot, L., Marigo, J.-J., 2010a. 1-D non-periodic homogenization for the seismic wave equation. Geophysical Journal International 181, 897–910, doi:10.1111/j.1365-246X.2010.04529.x.

Capdeville, Y., Guillot, L., Marigo, J.-J., 2010b. 2-D non-periodic homogenization to upscale elastic media for P–SV waves. Geophysical Journal International 182, 903–922, doi:10.1111/j.1365-246X.2010.04636.x.

Capdeville, Y., Marigo, J.-J., 2007. Second order homogenization of the elastic wave equation for non-periodic layered media. Geophysical Journal International 170, 823–838, doi:10.1111/j.1365-246X.2007.03462.x.

Carreras, J., Druguet, E., Griera, A., 2005. Shear zone-related folds. Journal of Structural Geology 27, 1229–1251, doi:10.1016/j.jsg.2004.08.004.

Chester, F.M., Evans, J.P., Biegel, R.L., 1993. Internal structure and weakening mechanisms of the San Andreas Fault. Journal of Geophysical Research 98, 771-786, doi:10.1029/92JB01866.

Chester, J.S., Chester, F.M., Kronenberg, A.K., 2005. Fracture surface energy of the Punchbowl fault, San Andreas system. Nature 437, 133-136, doi:10.1038/nature03942.

Christensen, N.I., Mooney, W.D., 1995. Seismic velocity structure and composition of the continental crust: A global view. Journal of Geophysical Research 100, 9761–9788, doi:10.1029/95JB00259.

Christoffel, E.B., 1877. Ueber die Fortpflanzung von Stössen durch elastische feste Körper. Annali di Matematica Pura ed Applicata 8, 193–243, doi:10.1007/bf02420789.

Cochran, E.S., Li, Y.-G., Shearer, P.M., Barbot, S., Fialko, Y., Vidale, J.E., 2009. Seismic and geodetic evidence for extensive, long-lived fault damage zones. Geology 37, 315-318, doi:10.1130/G25306A.1.

Cook, R.D., Malkus, D.S., Plesha, M.E., Witt, R.J., 2002. Concepts and Applications of Finite Element Analysis, 4th ed. John Wiley & Sons, Inc., New York, NY, USA.

Crampin, S., 1981. A review of wave motion in anisotropic and cracked elastic-media. Wave Motion 3, 343–391, doi:10.1016/0165-2125(81)90026-3.

Crampin, S., Chastin, S., 2003. A review of shear wave splitting in the crack-critical crust. Geophysical Journal International 155, 221–240, doi:10.1046/j.1365-246X.2003.02037.x.

Dempsey, E.D., Prior, D.J., Mariani, E., Toy, V.G., Tatham, D.J., 2011. Mica-controlled anisotropy within mid-to-upper crustal mylonites: an EBSD study of mica fabrics in the Alpine Fault Zone, New Zealand, in: Prior, D.J., Rutter, E.H., Tatham, D.J. (Eds.), Deformation Mechanisms, Rheology and Tectonics: Microstructures, Mechanics and Anisotropy. Geological Society, London, Special Publications, pp. 33–47, doi:10.1144/SP360.3.

Doll, W.E., Domoracki, W.J., Costain, J.K., Çoruh, C., Ludman, A., Hopeck, J.T., 1996. Seismic reflection evidence for the evolution of a transcurrent fault system: The Norumbega fault zone, Maine. Geology 24, 251-254, doi:10.1130/0091-7613(1996)024<0251:SREFTE>2.3.CO;2.

Dor, O., Rockwell, T.K., Ben-Zion, Y., 2006. Geological observations of damage asymmetry in the structure of the San Jacinto, San Andreas and Punchbowl faults in southern California: A possible indicator for preferred rupture propagation direction. Pure and Applied Geophysics 163, 301-349, doi:10.1007/s00024-005-0023-9.

Drury, M.R., Urai, J.L., 1990. Deformation-related recrystallization processes. Tectonophysics 172, 235-253, doi:10.1016/0040-1951(90)90033-5.

Ellsworth, W.L., Malin, P.E., 2011. Deep rock damage in the San Andreas Fault revealed by P- and S-type fault-zone-guided waves. In: Fagereng, Å ., Toy, V.G., Rowland, J.V. (Eds.), Geology of the Earthquake Source: A Volume in Honour of Rick Sibson, Geological Society, London, Special Publications 359, 39-53, doi:10.1144/SP359.3.

Faulkner, D.R., Mitchell, T.M., Healy, D., Heap, M.J., 2006. Slip on 'weak' faults by the rotation of regional stress in the fracture damage zone. Nature 444, 922-925, doi:10.1038/nature05353.

Faulkner, D.R., Mitchell, T.M., Jensen, E., Cembrano, J., 2011. Scaling of fault damage zones with displacement and the implications for fault growth processes. Journal of Geophysical Research 116, B05403, doi:10.1029/2010JB007788.

Fish, J., Wagiman, A., 1992. Multiscale finite element method for a periodic and nonperiodic heterogeneous medium. In: Noor, A.K. (Ed.), Adaptive, Multilevel, and Hierarchical Computational Strategies. American Society of Mechanical Engineers, New York, N.Y, 95–117.

Fliervoet, T.F., White, S.H., Drury, M.R., 1997. Evidence for dominant grain-boundary sliding deformation in greenschist- and amphibolite-grade polymineralic ultramylonites from the Redbank Deformed Zone, Central Australia. Journal of Structural Geology 19, 1495-1520, doi:10.1016/S0191-8141(97)00076-X.

Godfrey, N.J., Christensen, N.I., Okaya, D.A., 2000. Anisotropy of schists: Contribution of crustal anisotropy to active source seismic experiments and shear wave splitting observations. Journal of Geophysical Research 105, 27991–28007, doi:10.1029/2000JB900286.

Grover, T.W., Fernandes, L.C., 2003. Bedrock geology of the Weeks Mills quadrangle, Maine. Maine Geological Survey, Open-File Map 03-49, color map, scale 1:24000. https://digitalmaine.com/mgs_maps/31/

Guedes, J.M., Kikuchi, N., 1990. Preprocessing and postprocessing for materials based on the homogenization method with adaptive finite element methods. Computer Methods in Applied Mechanics and Engineering 83, 143–198, doi:10.1016/0045-7825(90)90148-F.

Guillot, L., Capdeville, Y., Marigo, J.-J., 2010. 2-D non-periodic homogenization of the elastic wave equation: SH case. Geophysical Journal International 182, 1438–1454, doi:10.1111/j.1365-246X.2010.04688.x.

Halfpenny, A., Prior, D.J., Wheeler, J., 2006. Analysis of dynamic recrystallization and nucleation in a quartzite mylonite. Tectonophysics 427, 3-14, doi:10.1016/j.tecto.2006.05.016.

Halfpenny, A., Prior, D.J., Wheeler, J., 2012. Electron backscatter diffraction analysis to determine the mechanisms that operated during dynamic recrystallisation of quartz-rich rocks. Journal of Structural Geology 36, 2-15, doi:10.1016/j.jsg.2012.01.001.

Handy, M.R., Hirth, G., Bürgmann, R., 2007. Continental fault structure and rheology from the frictional-to-viscous transition downward. In: Handy, M.R., Hirth, G., Hovius, N. (Eds.), Tectonic Faults: Agents of Change on a Dynamic Earth. MIT Press, Cambridge, MA, USA, 139-181.

Harris, L.B., Koyi, H.A., Fossen, H., 2002. Mechanisms for folding of high-grade rocks in extensional tectonic settings. Earth-Science Reviews 59, 163–210, doi:10.1016/S0012-8252(02)00074-0.

Hess, H.H., 1964. Seismic anisotropy of the uppermost mantle under oceans. Nature 203, 629–631, doi:10.1038/203629a0.

Hill, R., 1952. The elastic behaviour of a crystalline aggregate. Proceedings of the Physical Society. Section A 65, 349–354, doi:10.1088/0370-1298/65/5/307.

Hobbs, B.E., 1985. The geological significance of microfabric analysis. In: Wenk, H.-R. (Ed.), Preferred Orientation in Deformed Metal and Rocks: An Introduction to Modern Texture Analysis. Academic Press, San Diego, CA, USA, 463-484, doi:10.1016/B978-0-12-744020-0.50027-4.

Hobbs, B.E., Means, W.D., Williams, P.F., 1976. An Outline of Structural Geology. John Wiley & Sons, Inc., New York, NY, USA.

Hobbs, B.E., Ord, A., Teyssier, C., 1986. Earthquakes in the ductile regime? Pure and Applied Geophysics 124, 309-336, doi:10.1007/bf00875730.

Hollister, L.S., 1990. Enrichment of CO2 in fluid inclusions in quartz by removal of H2O during crystal-plastic deformation. Journal of Structural Geology 12, 895-901, doi:10.1016/0191-8141(90)90062-4.

Huang, Y., Ampuero, J.-P., Helmberger, D.V., 2016. The potential for supershear earthquakes in damaged fault zones – theory and observations. Earth and Planetary Science Letters 433, 109-115, doi:10.1016/j.epsl.2015.10.046.

Huang, Y., Ampuero, J.P., Helmberger, D.V., 2014. Earthquake ruptures modulated by waves in damaged fault zones. Journal of Geophysical Research 119, 3133-3154, doi:10.1002/2013JB010724.

Hubbard, M.S., 1999. Norumbega fault zone: Part of an orogen-parallel strike-slip system, northern Appalachians. In: Ludman, A., West, D.P., Jr. (Eds.), Norumbega Fault System of the Northern Appalachians. Geological Society of America Special Paper 331, 155-165, doi:10.1130/0-8137-2331-0.155.

Hudleston, P.J., Treagus, S.H., 2010. Information from folds: A review. Journal of Structural Geology 32, 2042–2071, doi:10.1016/j.jsg.2010.08.011.

Huntington, K.W., Klepeis, K.A., with 66 community contributors, 2018. Challenges and Opportunities for Research in Tectonics: Understanding Deformation and the Processes that Link Earth Systems, from Geologic Time to Human Time. A Community Vision Document Submitted to the National Science Foundation. University of Washington, doi:10.6069/H52R3PQ5.

Husseini, M.I., Randall, M.J., 1976. Rupture velocity and radiation efficiency. Bulletin of the Seismological Society of America 66, 1173-1187.

Imon, R., Okudaira, T., Kanagawa, K., 2004. Development of shape- and lattice-preferred orientations of amphibole grains during initial cataclastic deformation and subsequent deformation by dissolution–precipitation creep in amphibolites from the Ryoke metamorphic belt, SW Japan. Journal of Structural Geology 26, 793–805, doi:10.1016/j.jsg.2003.09.004.

Jiang, Z., Prior, D.J., Wheeler, J., 2000. Albite crystallographic preferred orientation and grain misorientation distribution in a low-grade mylonite: implications for granular flow. Journal of Structural Geology 22, 1663-1674, doi:10.1016/S0191-8141(00)00079-1.

Johnson, S.E., Lenferink, H.J., Price, N.A., Marsh, J.H., Koons, P.O., West, D.P., Beane, R., 2009. Clast-based kinematic vorticity gauges: The effects of slip at matrix/clast interfaces. Journal of Structural Geology 31, 1322-1339, doi:10.1016/j.jsg.2009.07.008.

Kanamori, H., Rivera, L., 2006. Energy partitioning during an earthquake. In: Abercrombie, R., McGarr, A., Toro, G.D., Kanamori, H. (Eds.), Earthquakes: Radiated Energy and the Physics of Faulting, American Geophysical Union Geophysical Monograph 170, 3-13, doi:10.1029/170GM03.

Karato, S., Jung, H., Katayama, I., Skemer, P., 2008. Geodynamic significance of seismic anisotropy of the upper mantle: New insights from laboratory studies. Annual Review of Earth and Planetary Sciences 36, 59–95, doi:10.1146/annurev.earth.36.031207.124120.

Kern, H., Ivankina, T.I., Nikitin, A.N., Lokajíček, T., Pros, Z., 2008. The effect of oriented microcracks and crystallographic and shape preferred orientation on bulk elastic anisotropy of a foliated biotite gneiss from Outokumpu. Tectonophysics 457, 143–149, doi:10.1016/j.tecto.2008.06.015.

Kerrich, R., 1976. Some effects of tectonic recrystallisation on fluid inclusions in vein quartz. Contributions to Mineralogy and Petrology 59, 195-202, doi:10.1007/BF00371308.

Kirkpatrick, J.D., Rowe, C.D., 2013. Disappearing ink: How pseudotachylytes are lost from the rock record. Journal of Structural Geology 52, 183-198, doi:10.1016/j.jsg.2013.03.003.

Kohlstedt, D.L., Evans, B., Mackwell, S.J., 1995. Strength of the lithosphere: Constraints imposed by laboratory experiments. Journal of Geophysical Research 100, 17587-17602, doi:10.1029/95JB01460.

Levshin, A., Ratnikova, L., 1984. Apparent ansiotropy in inhomogeneous media. Geophysical Journal of the Royal Astronomical Society 76, 65–69, doi:10.1111/j.1365-246X.1984.tb05022.x.

Lewis, M.A., Ben-Zion, Y., 2010. Diversity of fault zone damage and trapping structures in the Parkfield section of the San Andreas Fault from comprehensive analysis of near fault seismograms. Geophysical Journal International 183, 1579-1595, doi:10.1111/j.1365-246X.2010.04816.x.

Li, Y.-G., De Pascale, G.P., Quigley, M.C., Gravley, D.M., 2014. Fault damage zones of the M7.1 Darfield and M6.3 Christchurch earthquakes characterized by fault-zone trapped waves. Tectonophysics 618, 79-101, doi:10.1016/j.tecto.2014.01.029.

Li, Y.-G., Malin, P.E., 2008. San Andreas Fault damage at SAFOD viewed with fault-guided waves. Geophysical Research Letters 35, L08304, doi:10.1029/2007GL032924.

Lloyd, G.E., Butler, R.W.H., Casey, M., Mainprice, D., 2009. Mica, deformation fabrics and the seismic properties of the continental crust. Earth and Planetary Science Letters 288, 320–328, doi:10.1016/j.epsl.2009.09.035.

Lloyd, G.E., Butler, R.W.H., Casey, M., Tatham, D.J., Mainprice, D., 2011a. Constraints on the seismic properties of the middle and lower continental crust. In: Prior, D.J., Rutter, E.H., Tatham, D.J. (Eds.), Deformation Mechanisms, Rheology and Tectonics: Microstructures, Mechanics and Anisotropy. Geological Society, London, Special Publications, 7–32, doi:10.1144/SP360.2

Lloyd, G.E., Halliday, J.M., Butler, R.W.H., Casey, M., Kendall, J.-M., Wookey, J., Mainprice, D., 2011b. From crystal to crustal: petrofabric-derived seismic modelling of regional tectonics. In: Prior, D.J., Rutter, E.H., Tatham, D.J. (Eds.), Deformation Mechanisms, Rheology and Tectonics: Microstructures, Mechanics and Anisotropy. Geological Society, London, Special Publications, 49–78, doi:10.1144/SP360.4.

Lloyd, G.E., Kendall, J.M., 2005. Petrofabric-derived seismic properties of a mylonitic quartz simple shear zone: implications for seismic reflection profiling. In: Harvey, P.K., Brewer, T.S., Pezard, P.A., Petrov, V.A. (Eds.), Petrophysical Properties of Crystalline Rocks. Geological Society, London, Special Publications, 75–94, doi:10.1144/GSL.SP.2005.240.01.07.

Lowry, A.R., Pérez-Gussinyé, M., 2011. The role of crustal quartz in controlling Cordilleran deformation. Nature 471, 353-357, doi:10.1038/nature09912.

Ludman, A., West, D.P., Jr., 1999. Norumbega Fault System of the Northern Appalachians. Geological Society of America Special Paper 331, doi:10.1130/0-8137-2331-0.

Mahan, K., 2006. Retrograde mica in deep crustal granulites: Implications for crustal seismic anisotropy. Geophysical Research Letters 33, L24301, doi:10.1029/2006GL028130.

Mainprice, D., Humbert, M., 1994. Methods of calculating petrophysical properties from lattice preferred orientation data. Surveys in Geophysics 15, 575–592, doi:10.1007/BF00690175.

Mainprice, D., Nicolas, A., 1989. Development of shape and lattice preferred orientations: application to the seismic anisotropy of the lower crust. Journal of Structural Geology 11, 175–189, doi:10.1016/0191-8141(89)90042-4.

Matthies, S., Humbert, M., 1993. The realization of the concept of a geometric mean for calculating physical constants of polycrystalline materials. physica status solidi (b) 177, K47–K50, doi:10.1002/pssb.2221770231.

Mavko, G., Mukerji, T., Dvorkin, J., 2009. The Rock Physics Handbook: Tools for Seismic Analysis of Porous Media, 2nd ed. Cambridge University Press, New York, NY, USA.

Meissner, R., Rabbel, W., Kern, H., 2006. Seismic lamination and anisotropy of the lower continental crust. Tectonophysics 416, 81–99, doi:10.1016/j.tecto.2005.11.013.

Miller, S.A., Collettini, C., Chiaraluce, L., Cocco, M., Barchi, M., Kaus, B.J.P., 2004. Aftershocks driven by a high-pressure CO2 source at depth. Nature 427, 724-727, doi:10.1038/nature02251.

Mitchell, T.M., Ben-Zion, Y., Shimamoto, T., 2011. Pulverized fault rocks and damage asymmetry along the Arima-Takatsuki Tectonic Line, Japan. Earth and Planetary Science Letters 308, 284-297, doi:10.1016/j.epsl.2011.04.023.

Mitchell, T.M., Faulkner, D.R., 2008. Experimental measurements of permeability evolution during triaxial compression of initially intact crystalline rocks and implications for fluid flow in fault zones. Journal of Geophysical Research 113, B11412, doi:10.1029/2008JB005588.

Mitchell, T.M., Faulkner, D.R., 2009. The nature and origin of off-fault damage surrounding strike-slip fault zones with a wide range of displacements: A field study from the Atacama fault system, northern Chile. Journal of Structural Geology 31, 802-816, doi:10.1016/j.jsg.2009.05.002.

Morton, N., Girty, G.H., Rockwell, T.K., 2012. Fault zone architecture of the San Jacinto fault zone in Horse Canyon, southern California: A model for focused post-seismic fluid flow and heat transfer in the shallow crust. Earth and Planetary Science Letters 329-330, 71-83, doi:10.1016/j.epsl.2012.02.013.

Naus-Thijssen, F.M.J., Goupee, A.J., Johnson, S.E., Vel, S.S., Gerbi, C., 2011a. The influence of crenulation cleavage development on the bulk elastic and seismic properties of phyllosilicate-rich rocks. Earth and Planetary Science Letters 311, 212–224, doi:10.1016/j.epsl.2011.08.048.

Naus-Thijssen, F.M.J., Goupee, A.J., Vel, S.S., Johnson, S.E., 2011b. The influence of microstructure on seismic wave speed anisotropy in the crust: computational analysis of quartz-muscovite rocks. Geophysical Journal International 185, 609–621, doi:10.1111/j.1365-246X.2011.04978.x.

Nicolas, A., Poirier, J.P., 1976. Crystalline Plasticity and Solid State Flow in Metamorphic Rocks. John Wiley & Sons, Inc., New York, NY, USA.

Nye, J.F., 1985. Physical Properties of Crystals: Their Representation by Tensors and Matrices. Oxford University Press, New York, NY, USA.

O'Connell, R.J., Budiansky, B., 1974. Seismic velocities in dry and saturated cracked solids. Journal of Geophysical Research 79, 5412–5426, doi:10.1029/JB079i035p05412.

Okaya, D., Vel, S.S., Song, W.J., Johnson, S.E., 2018. Modification of crustal seismic anisotropy by geological structures ("structural geometric anisotropy"). Geosphere (in press).

Okaya, D.A., Christensen, N.I., 2002. Anisotropic effects of non-axial seismic wave propagation in foliated crustal rocks. Geophysical Research Letters 29, 2-1–2-4, doi:10.1029/2001GL014285.

Okaya, D.A., McEvilly, T.V., 2003. Elastic wave propagation in anisotropic crustal material possessing arbitrary internal tilt. Geophysical Journal International 153, 344–358, doi:10.1046/j.1365-246X.2003.01896.x.

Okudaira, T., Ogawa, D., Michibayashi, K., 2010. Grain-size-sensitive deformation of upper greenschist- to lower amphibolite-facies metacherts from a low-P/high-T metamorphic belt. Tectonophysics 492, 141-149, doi:10.1016/j.tecto.2010.06.002.

Olver, F.W.J., Lozier, D.W., Boisvert, R.F., Clark, C.W. (Eds.), 2010. NIST Handbook of Mathematical Functions. Cambridge University Press, New York, NY, USA.

Panozzo, R., 1984. Two-dimensional strain from the orientation of lines in a plane. Journal of Structural Geology 6, 215-221, doi:10.1016/0191-8141(84)90098-1.

Panozzo, R.H., 1983. Two-dimensional analysis of shape-fabric using projections of digitized lines in a plane. Tectonophysics 95, 279-294, doi:10.1016/0040-1951(83)90073-2.

Passchier, C.W., 1982. Pseudotachylyte and the development of ultramylonite bands in the Saint-Barthélemy Massif, French Pyrenees. Journal of Structural Geology 4, 69-79, doi:10.1016/0191-8141(82)90008-6.

Perrin, C., Manighetti, I., Ampuero, J.P., Cappa, F., Gaudemer, Y., 2016. Location of largest earthquake slip and fast rupture controlled by along-strike change in fault structural maturity due to fault growth. Journal of Geophysical Research 121, 3666-3685, doi:10.1002/2015JB012671.

Poblet, J., Lisle, R.J. (Eds.), 2011. Kinematic Evolution and Structural Styles of Fold-and-Thrust Belts. Geological Society, London, Special Publications, 349.

Poliakov, A.N.B., Dmowska, R., Rice, J.R., 2002. Dynamic shear rupture interactions with fault bends and off-axis secondary faulting. Journal of Geophysical Research 107, 2295, doi:10.1029/2001JB000572.

Price, N.A., Johnson, S.E., Gerbi, C.C., West, D.P., 2012. Identifying deformed pseudotachylyte and its influence on the strength and evolution of a crustal shear zone at the base of the seismogenic zone. Tectonophysics 518-521, 63-83, doi:10.1016/j.tecto.2011.11.011.

Price, N.A., Song, W.J., Johnson, S.E., Gerbi, C.C., Beane, R.J., West, D.P., Jr., 2016. Recrystallization fabrics of sheared quartz veins with a strong pre-existing crystallographic preferred orientation from a seismogenic shear zone. Tectonophysics 682, 214-236, doi:10.1016/j.tecto.2016.05.030.

Ramsay, J.G., 1967. Folding and Fracturing of Rocks. McGraw-Hill, New York, NY, USA.

Ramsay, J.G., Huber, M.I., 1987. The Techniques of Modern Structural Geology, Volume 2: Folds and Fractures. Academic Press, London, UK.

Ranalli, G., 1984. Grain size distribution and flow stress in tectonites. Journal of Structural Geology 6, 443-447, doi:10.1016/0191-8141(84)90046-4.

Rempe, M., Mitchell, T., Renner, J., Nippress, S., Ben-Zion, Y., Rockwell, T., 2013. Damage and seismic velocity structure of pulverized rocks near the San Andreas Fault. Journal of Geophysical Research 118, 2813-2831, doi:10.1002/jgrb.50184.

Reuss, A., 1929. Berechnung der fließgrenze von mischkristallen auf grund der plastizitätsbedingung für einkristalle. Zeitschrift für Angewandte Mathematik und Mechanik 9, 49–58, doi:10.1002/zamm.19290090104.

Rice, J.R., Sammis, C.G., Parsons, R., 2005. Off-fault secondary failure induced by a dynamic slip pulse. Bulletin of the Seismological Society of America 95, 109-134, doi:10.1785/0120030166.

Savage, H.M., Brodsky, E.E., 2011. Collateral damage: Evolution with displacement of fracture distribution and secondary fault strands in fault damage zones. Journal of Geophysical Research 116, B03405, doi:10.1029/2010JB007665.

Savage, M.K., 1999. Seismic anisotropy and mantle deformation: What have we learned from shear wave splitting? Reviews of Geophysics 37, 65–106, doi:10.1029/98RG02075.

Schmatz, J., Urai, J.L., 2011. The interaction of migrating grain boundaries and fluid inclusions in naturally deformed quartz: A case study of a folded and partly recrystallized quartz vein from the Hunsrück Slate, Germany. Journal of Structural Geology 33, 468-480, doi:10.1016/j.jsg.2010.12.010.

Schmid, S.M., Casey, M., 1986. Complete fabric analysis of some commonly observed quartz c-axis patterns. In: Hobbs, B.E., Heard, H.C. (Eds.), Mineral and Rock Deformation: Laboratory Studies, American Geophysical Union Geophysical Monograph 36, 263-286, doi:10.1029/GM036p0263.

Schoenberg, M., Muir, F., 1989. A calculus for finely layered anisotropic media. Geophysics 54, 581–589, doi:10.1190/1.1442685.

Shipton, Z.K., Evans, J.P., Abercrombie, R.E., Brodsky, E.E., 2006. The missing sinks: Slip localization in faults, damage zones, and the seismic energy budget. In: Abercrombie, R., McGarr, A., Toro, G.D., Kanamori, H. (Eds.), Earthquakes: Radiated Energy and the Physics of Faulting, American Geophysical Union Geophysical Monograph 170, 217-222, doi:10.1029/170GM22.

Sibson, R.H., 1975. Generation of pseudotachylyte by ancient seismic faulting. Geophysical Journal International 43, 775-794, doi:10.1111/j.1365-246X.1975.tb06195.x.

Sibson, R.H., 1980. Transient discontinuities in ductile shear zones. Journal of Structural Geology 2, 165-171, doi:10.1016/0191-8141(80)90047-4.

Siegesmund, S., Takeshita, T., Kern, H., 1989. Anisotropy of V_P and V_S in an amphibolite of the deeper crust and its relationship to the mineralogical, microstructural and textural characteristics of the rock. Tectonophysics 157, 25–38, doi:10.1016/0040-1951(89)90338-7.

Silver, P.G., 1996. Seismic anisotropy beneath the continents: Probing the depths of geology. Annual Review of Earth and Planetary Sciences 24, 385–432, doi:10.1146/annurev.earth.24.1.385.

Simón, J.L., 2004. Superposed buckle folding in the eastern Iberian Chain, Spain. Journal of Structural Geology 26, 1447–1464, doi:10.1016/j.jsg.2003.11.026.

Skemer, P., Katayama, I., Jiang, Z., Karato, S.-i., 2005. The misorientation index: Development of a new method for calculating the strength of lattice-preferred orientation. Tectonophysics 411, 157-167, doi:10.1016/j.tecto.2005.08.023.

Spudich, P., Olsen, K.B., 2001. Fault zone amplified waves as a possible seismic hazard along the Calaveras Fault in central California. Geophysical Research Letters 28, 2533-2536, doi:10.1029/2000GL011902.

Stipp, M., Tullis, J., 2003. The recrystallized grain size piezometer for quartz. Geophysical Research Letters 30, 2088, doi:10.1029/2003gl018444.

Sullivan, W.A., Peterman, E.M., 2017. Pulverized granite at the brittle-ductile transition: An example from the Kellyland fault zone, eastern Maine, U.S.A. Journal of Structural Geology 101, 109-123, doi:10.1016/j.jsg.2017.07.002.

Tatham, D.J., Lloyd, G.E., Butler, R.W.H., Casey, M., 2008. Amphibole and lower crustal seismic properties. Earth and Planetary Science Letters 267, 118–128, doi:10.1016/j.epsl.2007.11.042.

Thomas, M.Y., Bhat, H.S., Klinger, Y., 2017. Effect of brittle off-fault damage on earthquake rupture dynamics. In: Thomas, M.Y., Mitchell, T.M., Bhat, H.S. (Eds.), Fault Zone Dynamic Processes, American Geophysical Union Geophysical Monograph 227, 225-280, doi:10.1002/9781119156895.ch14.

Ting, T.C.T., 1996. Anisotropic Elasticity: Theory and Applications. Oxford University Press, New York, NY, USA.

Treagus, S.H., 1973. Buckling stability of a viscous single-layer system, oblique to the principal compression. Tectonophysics 19, 271–289, doi:10.1016/0040-1951(73)90022-X.

Trepmann, C.A., Hsu, C., Hentschel, F., Döhler, K., Schneider, C., Wichmann, V., 2017. Recrystallization of quartz after low-temperature plasticity – The record of stress relaxation below the seismogenic zone. Journal of Structural Geology 95, 77-92, doi:10.1016/j.jsg.2016.12.004.

Trepmann, C.A., Stöckhert, B., 2002. Cataclastic deformation of garnet: a record of synseismic loading and postseismic creep. Journal of Structural Geology 24, 1845-1856, doi:10.1016/S0191-8141(02)00004-4.

Trepmann, C.A., Stöckhert, B., Dorner, D., Moghadam, R.H., Küster, M., Röller, K., 2007. Simulating coseismic deformation of quartz in the middle crust and fabric evolution during postseismic stress relaxation — An experimental study. Tectonophysics 442, 83-104, doi:10.1016/j.tecto.2007.05.005.

Underwood, E.E., 1970. Quantitative Stereology. Addison-Wesley Publishing Company, Reading, MA, USA.

Vel, S.S., Cook, A.C., Johnson, S.E., Gerbi, C., 2016. Computational homogenization and micromechanical analysis of textured polycrystalline materials. Computer Methods in Applied Mechanics and Engineering 310, 749-779, doi:10.1016/j.cma.2016.07.037.

Vel, S.S., Goupee, A.J., 2010. Multiscale thermoelastic analysis of random heterogeneous materials, Part I: Microstructure characterization and homogenization of material properties. Computational Materials Science 48, 22–38, doi:10.1016/j.commatsci.2009.11.015.

Venkataraman, A., Kanamori, H., 2004. Observational constraints on the fracture energy of subduction zone earthquakes. Journal of Geophysical Research 109, B05302, doi:10.1029/2003JB002549.

Voigt, W., 1928. Lehrbuch der Kristallphysik. B.G. Teubner, Leipzig, Germany.

Ward, D., Mahan, K., Schulte-Pelkum, V., 2012. Roles of quartz and mica in seismic anisotropy of mylonites. Geophysical Journal International 190, 1123–1134, doi:10.1111/j.1365-246X.2012.05528.x.

Weiss, T., Siegesmund, S., Rabbel, W., Bohlen, T., Pohl, M., 1999. Seismic velocities and anisotropy of the lower continental crust: A review. Pure and Applied Geophysics 156, 97–122, doi:10.1007/s000240050291.

Wenk, H.-R., 1985. Preferred Orientation in Deformed Metal and Rocks: An Introduction to Modern Texture Analysis. Academic Press, Inc., Orlando, FL, USA.

West, D.P., Jr., 1999. Timing of displacements along the Norumbega fault system, south-central and south-coastal Maine. In: Ludman, A., West, D.P., Jr. (Eds.), Norumbega Fault System of the Northern Appalachians. Geological Society of America Special Paper 331, 167-178, doi:10.1130/0-8137-2331-0.167.

West, D.P., Jr., Peterman, E.M., 2004. Bedrock geology of the Razorville quadrangle, Maine. Maine Geological Survey, Open-File Map 04-29, color map, scale 1:24000. https://digitalmaine.com/mgs_maps/40/

Wheeler, J., Prior, D., Jiang, Z., Spiess, R., Trimby, P., 2001. The petrological significance of misorientations between grains. Contributions to Mineralogy and Petrology 141, 109-124, doi:10.1007/s004100000225.

White, S., 1979. Grain and sub-grain size variations across a mylonite zone. Contributions to Mineralogy and Petrology 70, 193-202, doi:10.1007/bf00374448.

Williams, M.L., Scheltema, K.E., Jercinovic, M.J., 2001. High-resolution compositional mapping of matrix phases: implications for mass transfer during crenulation cleavage development in the Moretown Formation, western Massachusetts. Journal of Structural Geology 23, 923–939, doi:10.1016/S0191-8141(00)00164-4.

Wolfram Research, Inc., 2012. Mathematica, version 9.0. Wolfram Research, Inc., Champaign, IL, USA.

Xu, S., Ben-Zion, Y., 2017. Theoretical constraints on dynamic pulverization of fault zone rocks. Geophysical Journal International 209, 282-296, doi:10.1093/gji/ggx033.

APPENDIX. BASIC TUTORIAL OF THERMOELASTIC AND SEISMIC ANALYSIS (TESA) TOOLBOX VERSION 2.1

This basic tutorial was written on April 26, 2018 for Stress/Strain Analysis, describing Phase Information, Mesh Options, AEH-FE Homogenization, and Stress/Strain Analysis in TESA toolbox. Heat Conduction analysis and Seismic Speed Wave Analysis will be explained in the future.

A.1. Install TESA Toolbox (standalone program)

Go to the web page (https://umaine.edu/mecheng/vel/software/tesa_toolbox/; Fig. A1), download, and install the program (see the instructions in the web page).

Figure A1. Screen capture of the web page to download the TESA Toolbox.

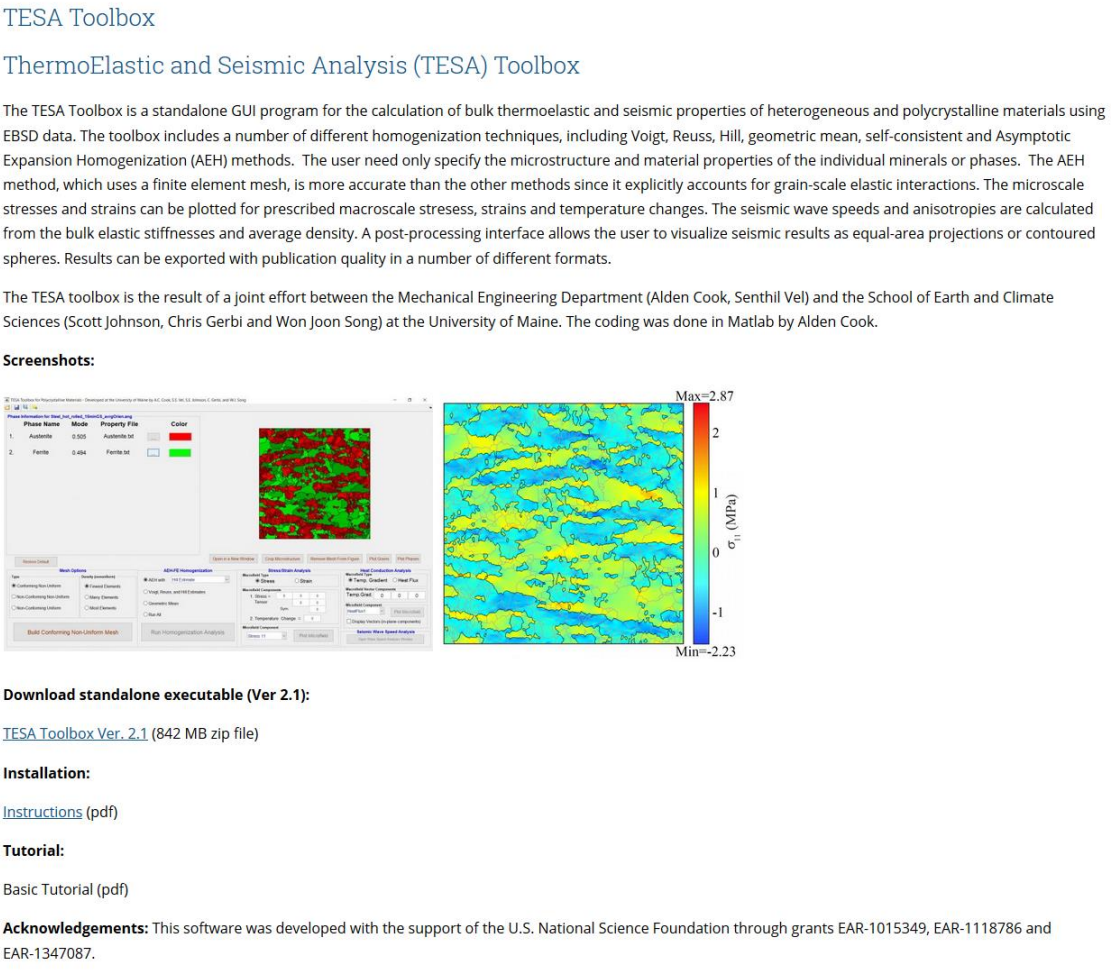

TESA Toolbox

ThermoElastic and Seismic Analysis (TESA) Toolbox

The TESA Toolbox is a standalone GUI program for the calculation of bulk thermoelastic and seismic properties of heterogeneous and polycrystalline materials using EBSD data. The toolbox includes a number of different homogenization techniques, including Voigt, Reuss, Hill, geometric mean, self-consistent and Asymptotic Expansion Homogenization (AEH) methods. The user need only specify the microstructure and material properties of the individual minerals or phases. The AEH method, which uses a finite element mesh, is more accurate than the other methods since it explicitly accounts for grain-scale elastic interactions. The microscale stresses and strains can be plotted for prescribed macroscale stresess, strains and temperature changes. The seismic wave speeds and anisotropies are calculated from the bulk elastic stiffnesses and average density. A post-processing interface allows the user to visualize seismic results as equal-area projections or contoured spheres. Results can be exported with publication quality in a number of different formats.

The TESA toolbox is the result of a joint effort between the Mechanical Engineering Department (Alden Cook, Senthil Vel) and the School of Earth and Climate Sciences (Scott Johnson, Chris Gerbi and Won Joon Song) at the University of Maine. The coding was done in Matlab by Alden Cook.

Screenshots:

Download standalone executable (Ver 2.1):

TESA Toolbox Ver. 2.1 (842 MB zip file)

Installation:

Instructions (pdf)

Tutorial:

Basic Tutorial (pdf)

Acknowledgements: This software was developed with the support of the U.S. National Science Foundation through grants EAR-1015349, EAR-1118786 and EAR-1347087.

A.2. Homogenization Analysis using EBSD Data

This tutorial is to analyze grain-scale stresses and strains of a polycrystalline material subjected to macroscale loads. Thus, we consider here only Asymptotic Expansion Homogenization (AEH) using a finite element mesh.

A.2.1. Open TESA Toolbox

The standalone GUI (graphic user interface) program (Fig. A2) and other two windows (Fig. A3) will open. Do not close the 'black' window during analysis, which is linked to the GUI program.

Figure A2. The standalone TESA program.

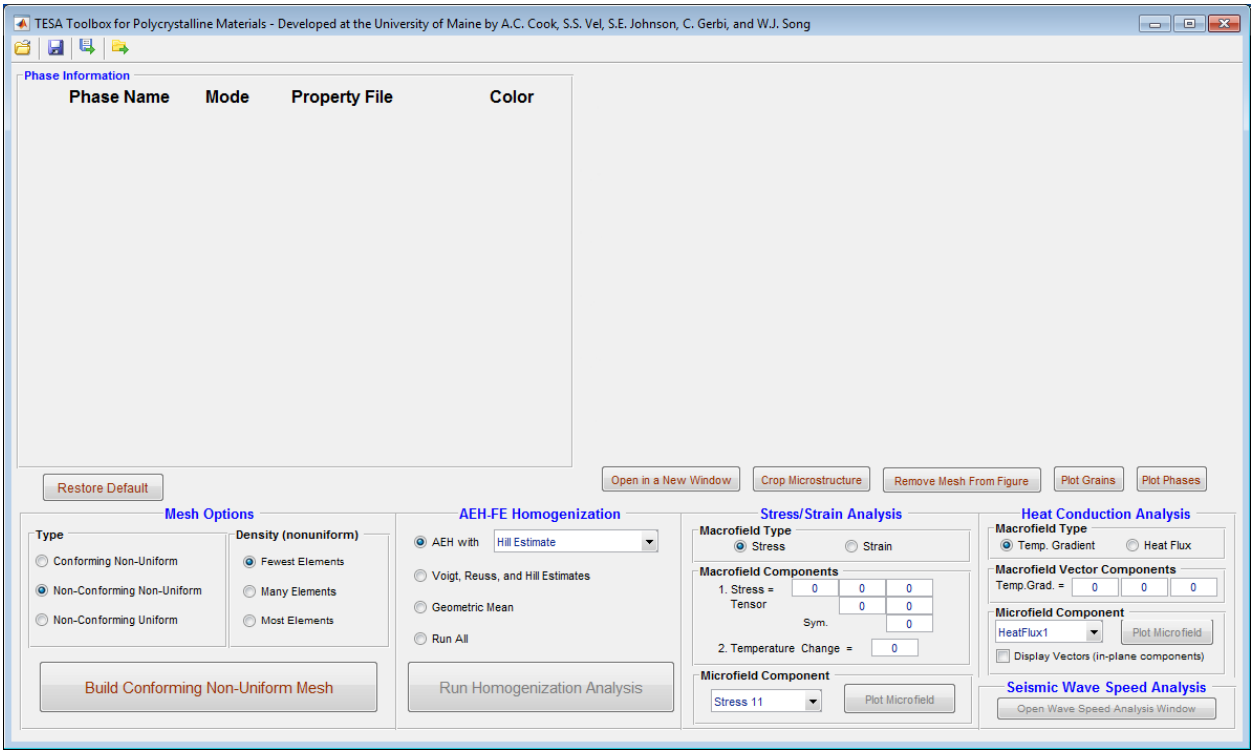

Figure A3. Additional windows when opening TESA Toolbox.

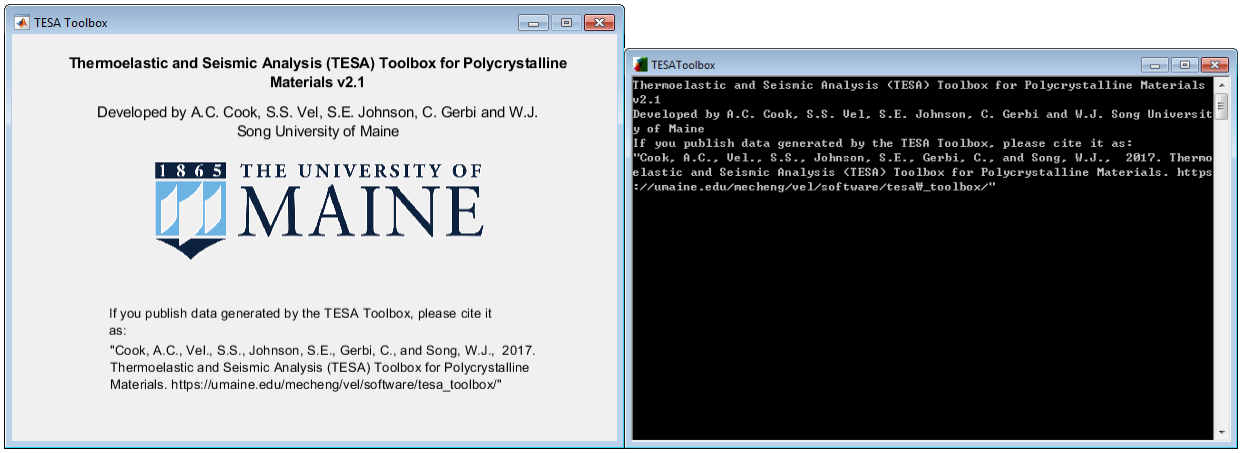

A.2.2. Load Analysis File

Open the sample file, "TestSample1.ang" in the folder of "Tutorial_TestSample" (Fig. A4). The Electron backscatter diffraction (EBSD) data must be acquired in square grid format. Note that EBSD data file for TESA Toolbox should be made using single orientation per grain. In other words, all the crystallographic orientations (Euler angles) within a grain should be same.

Figure A4. Loading analysis file.

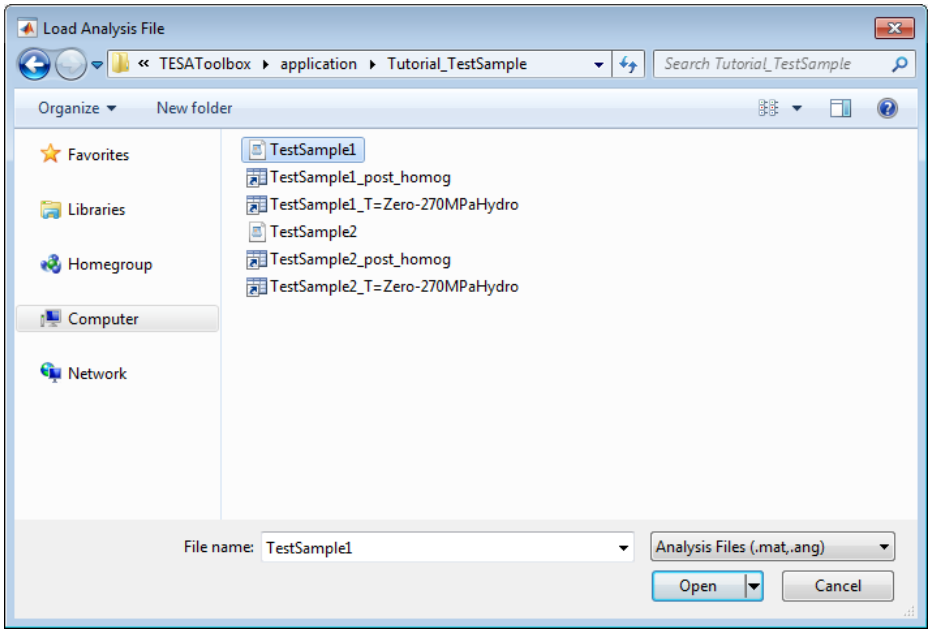

A.2.3. Choose the type of analysis

After loading the sample file, select “Wave Speeds and Microfields” of the analysis types.

Figure A5. Choosing the type of analysis.

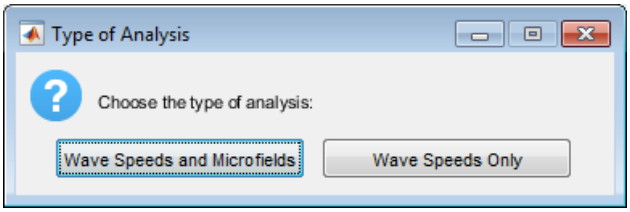

A.2.4. EBSD Data Input

The input file must have three Euler angle, x- and y-coordinates, and phase information. Typical .ang files exported from EDAX OIM software have the phase information in 8th column, but the sample file has it in 6th column. Enter “1”, “4”, “6” (default values) in each entry (Fig. A6).

Figure A6. EBSD data input.

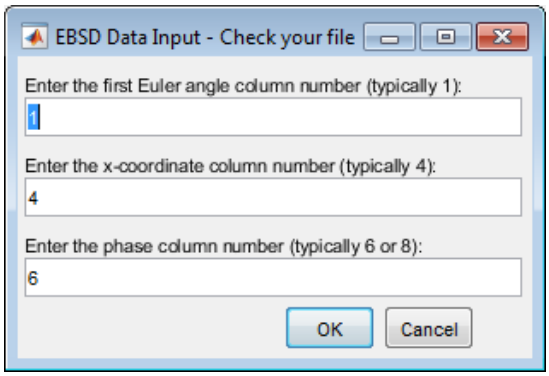

A.2.5. Input Reference Frame Orientation

The current version supports only .ang file format. If the file was converted from .ctf format exported from Oxford HKL CHANNEL system, note that OIM and HKL systems generally use different reference frames. The reference direction in OIM is the Ypixel direction and in HKL is the Xpixel direction. Typically, the OIM system needs 90 degrees for the reference frame orientation in TESA Toolbox, and the HKL system requires 180 degrees assuming CS0=CS1. See below.

Reference direction = RD (OIM) = X0 (HKL) = R (HKL) Transverse direction = TD (OIM) = Y0 (HKL) = T (HKL)	
Reference frame options and their orientations for TESA Toolbox	
(a) RD (OIM) is coincident with the –Ypixel direction (upward on screen)	90
(b) RD (OIM) is coincident with the +Ypixel direction (downward on screen)	–90
(c) Y0 (HKL) is coincident with the +Ypixel direction (downward on screen)	180
(d) Y0 (HKL) is coincident with the –Ypixel direction (upward on screen)	0

For EBSD file from EDAX OIM system, enter "90" (default value) to specify the orientation of the reference frame (Fig. A7).

Figure A7. Input of reference frame orientation.

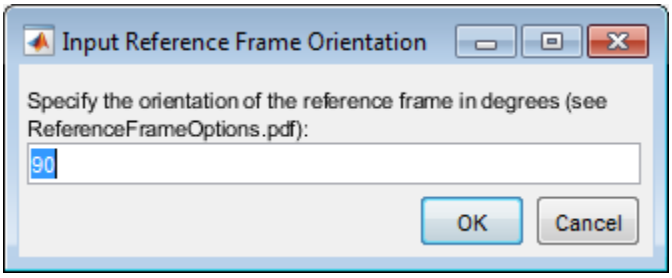

A.2.6. (Optional) Remove Small Grains

You can remove small grains by defining the number of pixels for the minimum grain size. Here "10" pixels per grain is selected (default values; Fig. A8).

Figure A8. Removing small grains.

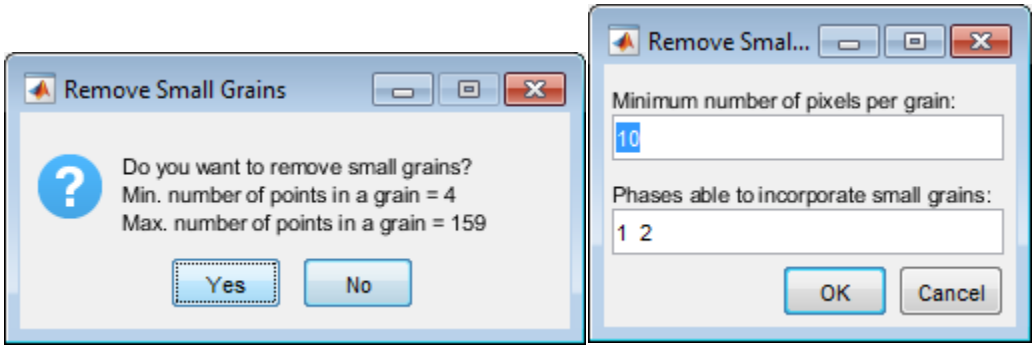

Now, the toolbox will be shown as below (Fig. A9).

Figure A9. TESA Toolbox after loading an EBSD file and deciding basic options for the EBSD data.

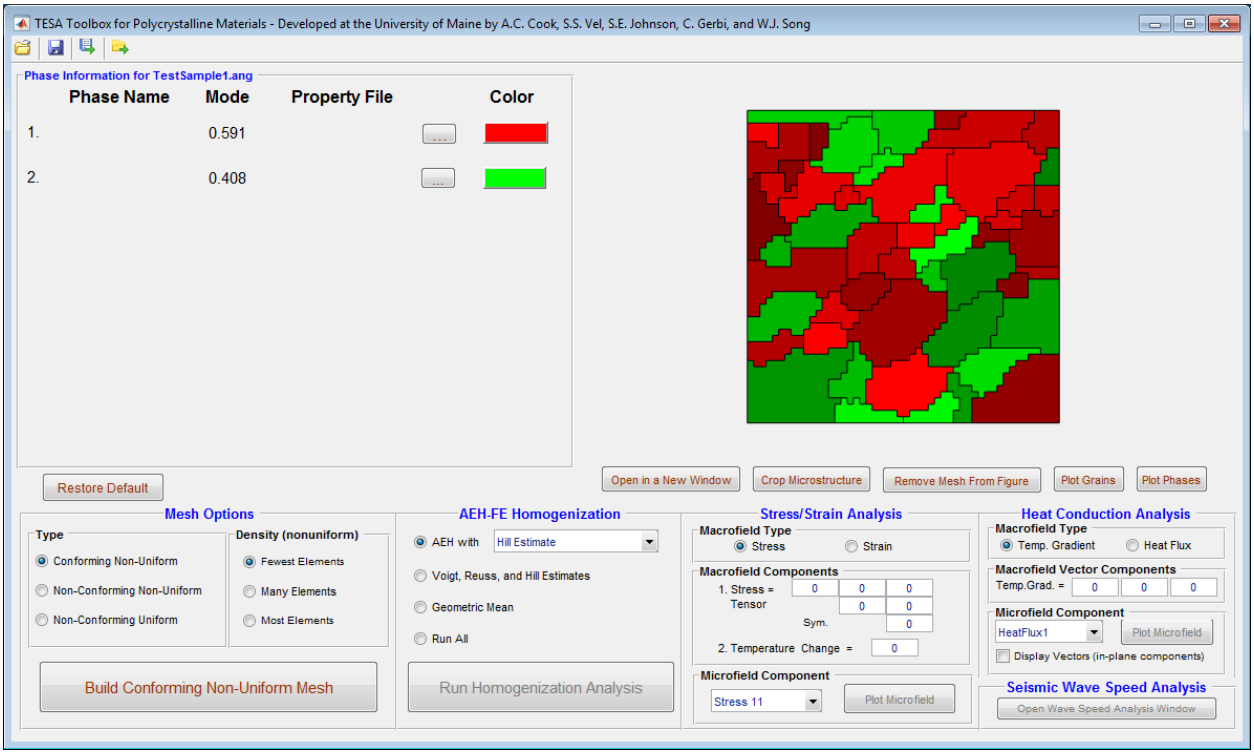

A.2.7. Assign Properties to Each Phase

For TestSample1, select "alpha-Quartz_2006_Ohno.txt" for Phase 1 and "Plagioclase_An25_2016_Brown.txt" for Phase 2, from the folder of "Tutorial_TestSample" (Fig. A10).

Figure A10. TESA Toolbox after assigning properties for each phase.

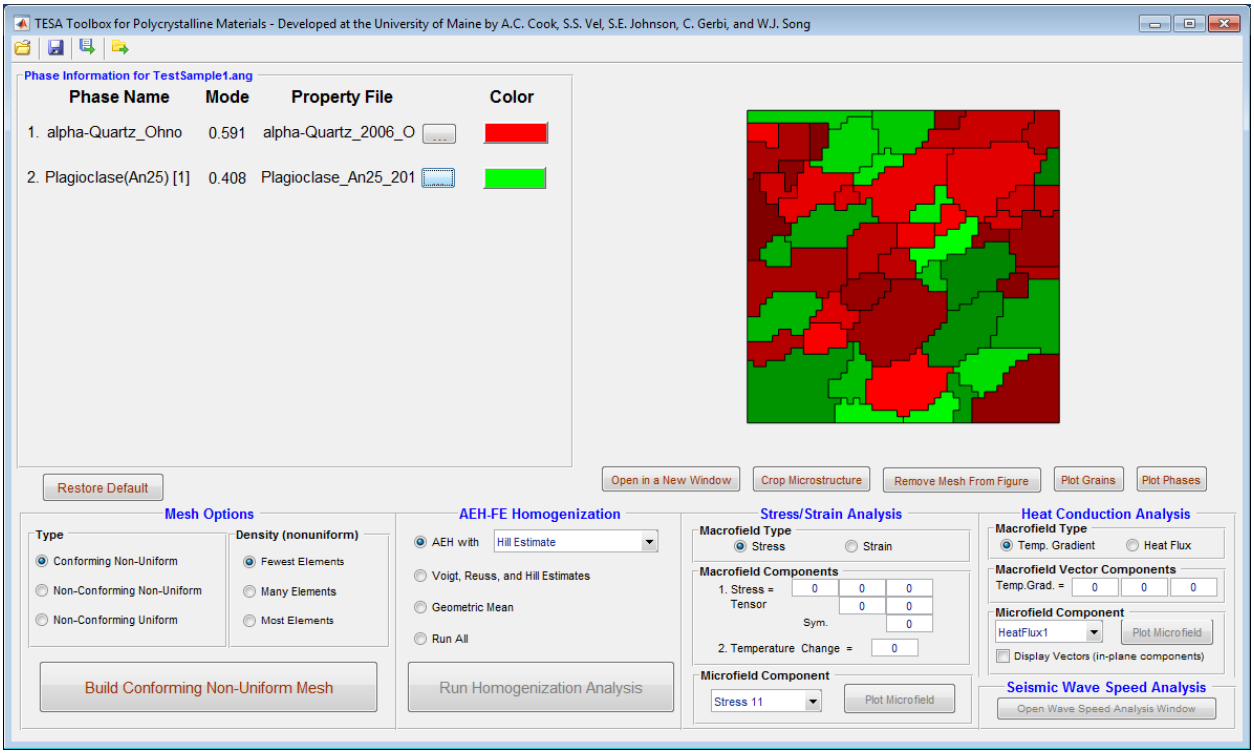

Note that Property files for TESA Toolbox should contain the five items: phase name, density (kg/m3), elastic stiffness matrix (Pascals), thermal expansion coefficients (1/K), and thermal conductivity matrix (W/(m K)). If there is no information of the last two items for the phase, type any numbers, and do not use the items in your analysis. Property file must be written in the same format as the provided property files (do not add or delete lines between items) (Fig. A11).

Figure A11. An example of property file. Elements of the thermal expansion tensor are arranged as 11, 22, 33, 23, 13, and 12 from top to bottom.

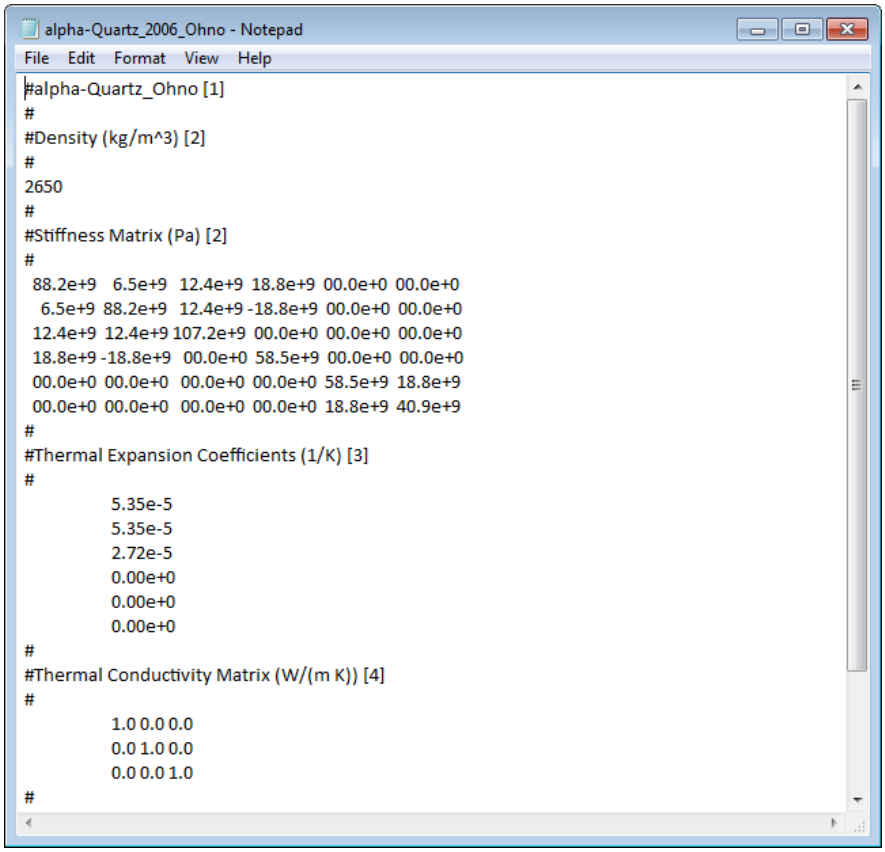

A.2.8. Select Mesh Options

Click “Build Conforming Non-Uniform Mesh” with default options (“conforming non-uniform” for mesh type and “fewest elements” for mesh density) (Fig. A12).

Figure A12. Mesh options.

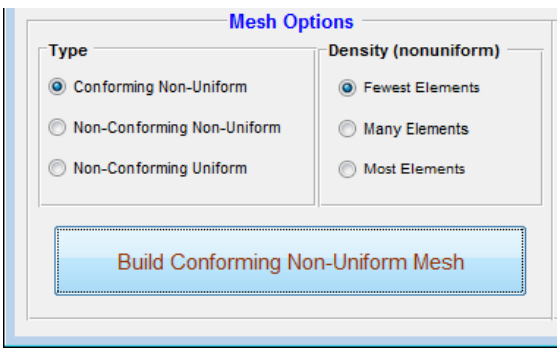

A.2.9. Mesh Size Function Parameters

Enter “0.007” for the first entry and select default values for the other entries, or you may select default for all the entries (Fig. A13).

Figure A13. Mesh size function parameters.

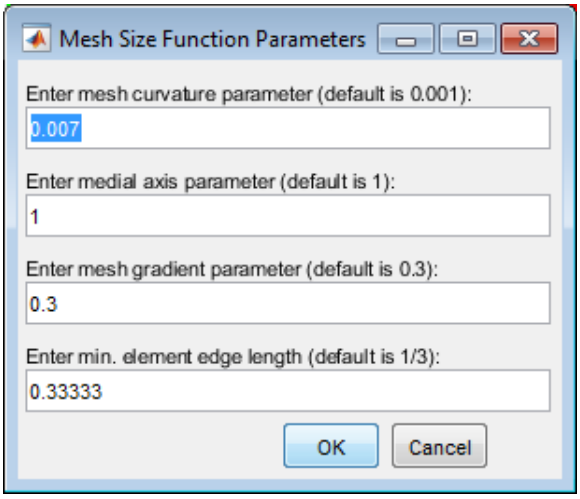

After clicking OK, you can see the following windows (Fig. A14).

Figure A14. Meshing progress and information.

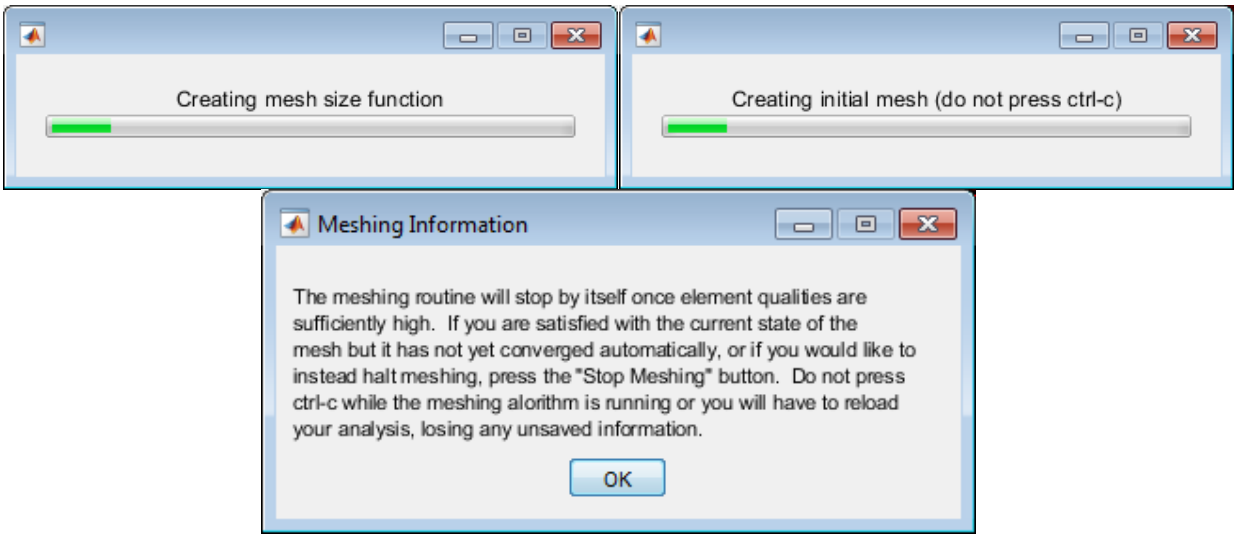

If your EBSD file has relatively small data points and simple grain boundary shapes, you can see the meshing routine is complete and stops automatically in some time (e.g., several hours or a day). However, in the case of relatively big file size, you may need to stop the meshing routine by yourself after the initial mesh.

After building the mesh, the toolbox will be shown as below (Fig. A15). You can save or export the mesh plot as MATLAB figure (.fig) or bitmap format after "Open in a New Window". Similarly, you can also "Plot Grains" and save it.

Figure A15. TESA Toolbox when completing meshing.

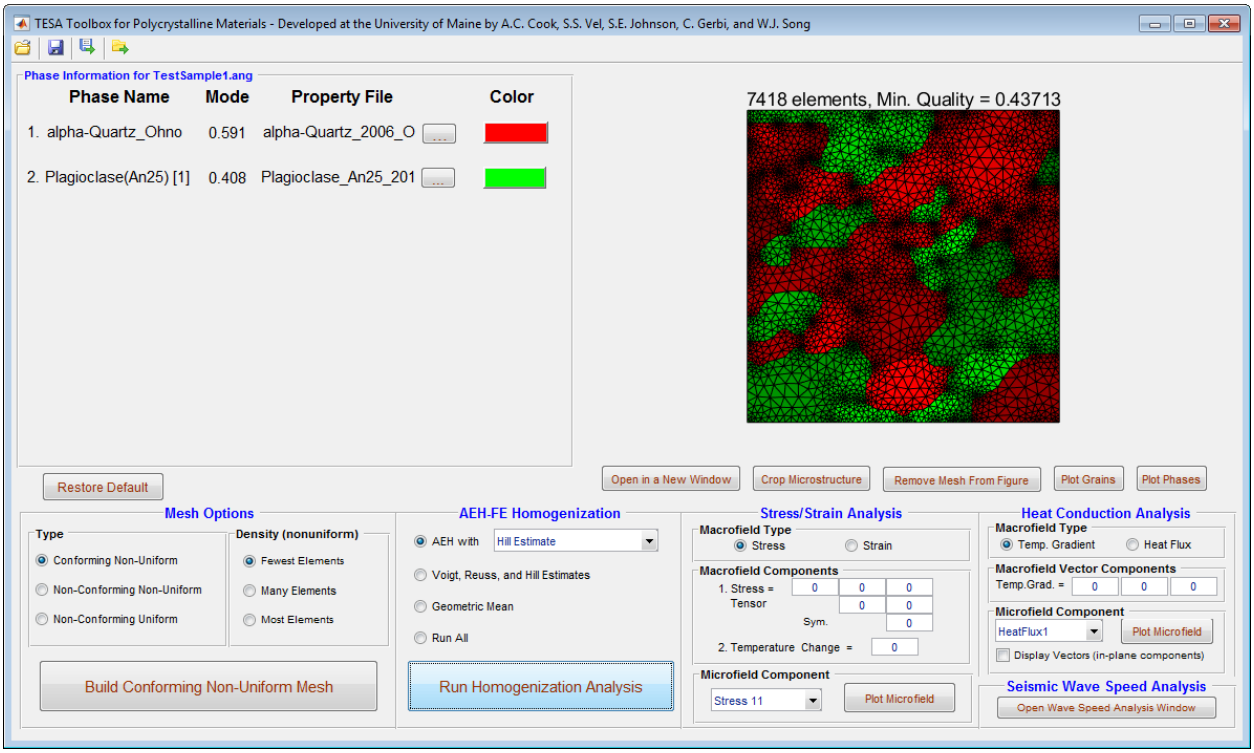

A.2.10. AEH-FE Homogenization

For the analysis of grain-scale stresses and strains, “Run Homogenization Analysis” using AEH with Hill Estimate (default option) (Fig. A16).

Figure A16. AEH-FE homogenization.

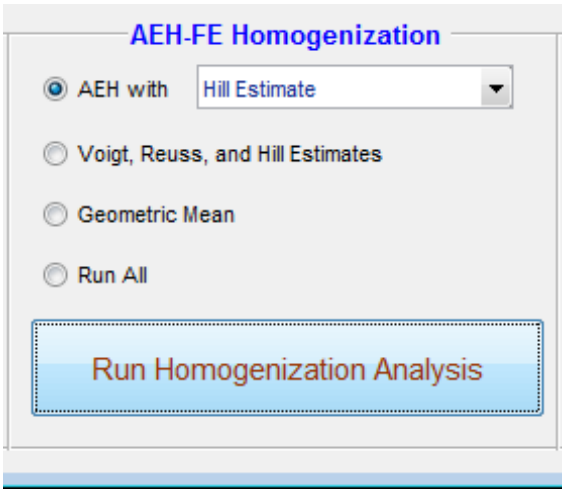

And then, progress bars will be displays as below (Fig. A17).

Figure A17. Progress bars related to AEH-FE homogenization.

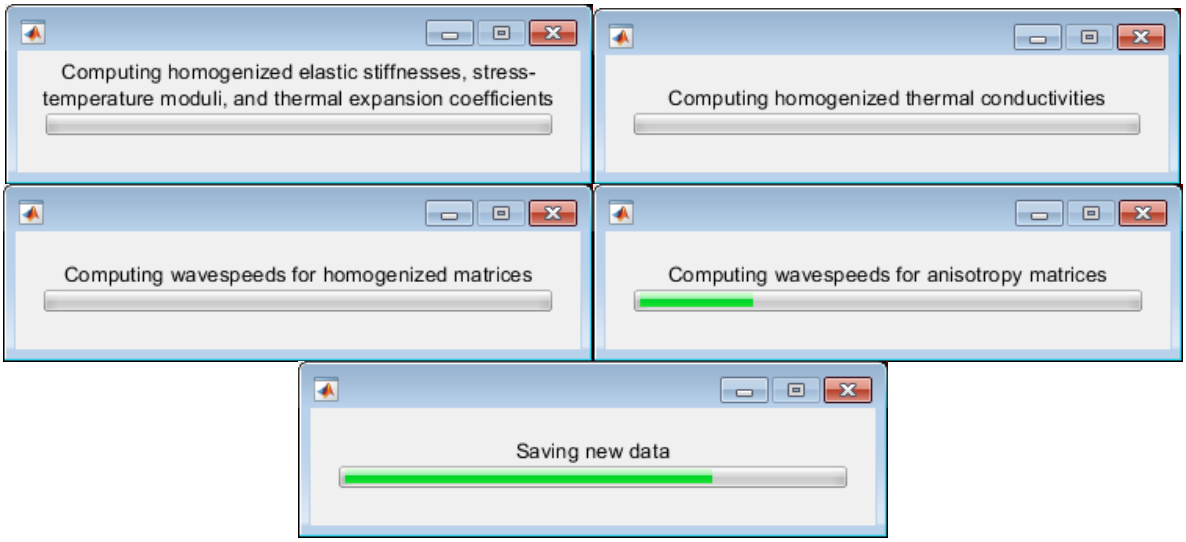

A.2.11. (Optional) Save Processed Files

You can take and save the following two files for future sensitivity test and analysis information: (a) "TestSample1_post_homog.mat" in the folder of "Auto Saves" (Fig. A18) and (b) "Analysis Info - TestSample.txt" in the folder of "Saved Analyses" (Fig. A19). You may want to move them to a folder (e.g., "12Apr2018_TestSample1_1") created automatically in "Saved Analyses" during analysis. To see the text file of "Analysis Info" in a well-organized display, open it through MATLAB, not just double-click it in the windows folder.

Figure A18. Automatically saved processed files.

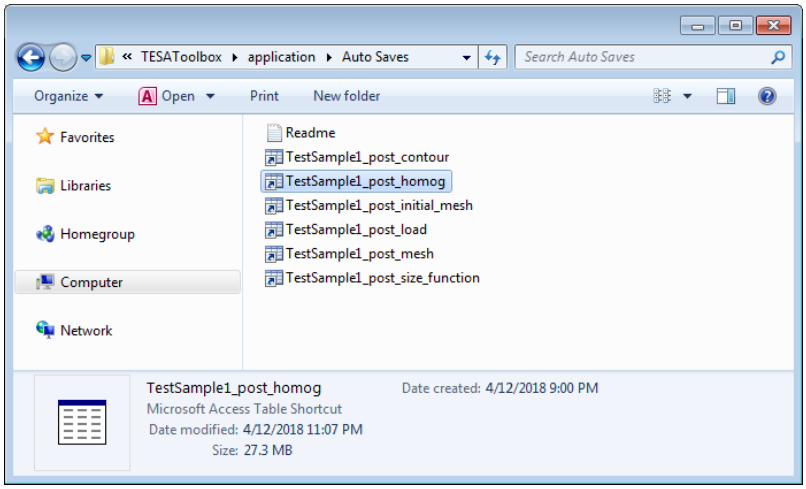

Figure A19. Automatically saved analysis information file.

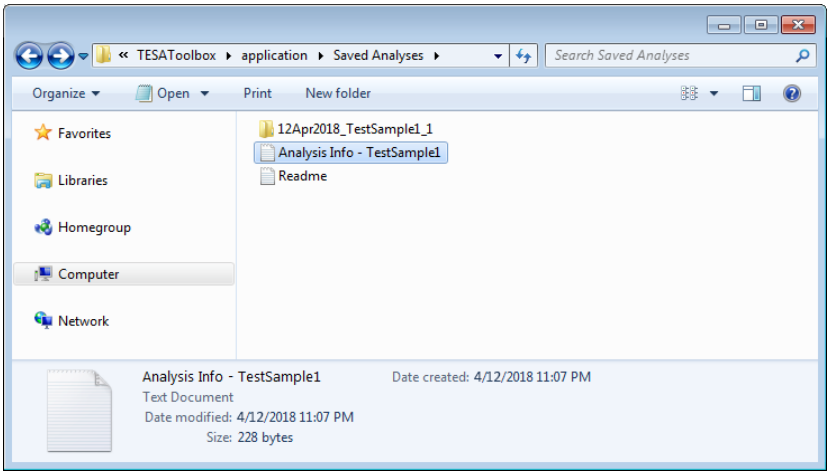

During analysis, a new folder (e.g., "12Apr2018_TestSample1_1") in the "Saved Analyses" folder is created, in which you can see all the homogenization results and the used property files after the analysis is finished (Fig. A20).

Figure A20. A new folder and files created during the analysis under the "Saved Analyses" folder.

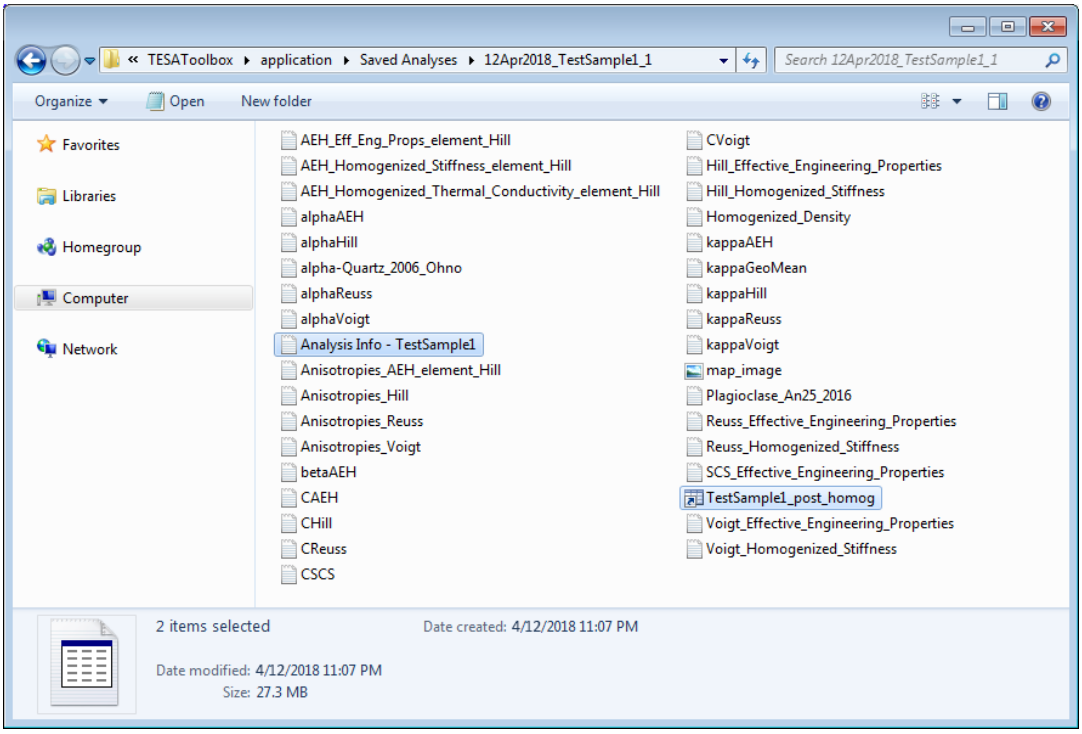

And also in the "Effective Stiffnesses and Anisotropies" folder, a new folder (e.g., "12Apr2018_23h_7m_TestSample1") is created, in which all the homogenization results are saved.

Figure A21. A new folder created during the analysis under the "Effective Stiffnesses and Anisotropies" folder.

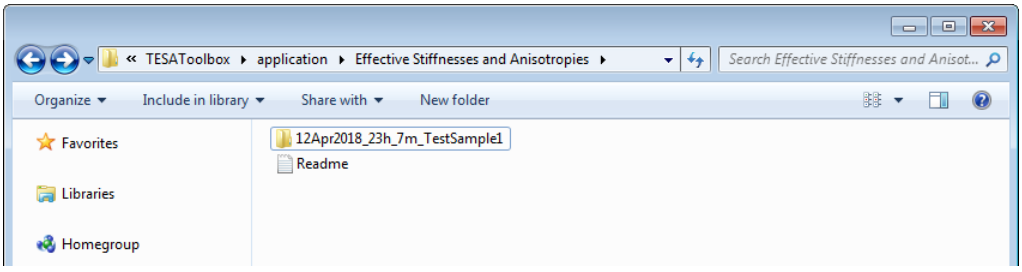

A.3. Stress/Strain Analysis

After homogenization analysis using AEH, select "Macrofield Type" ("Stress" here), and enter values in "Macrofield Components". For example, -270MPa (-270e6) hydrostatic confining pressure (negative for compression) and 0° temperature change (no temperature change in this example) (Fig. A22). If you have 'thermal expansion coefficients' for the phases in their property files, put a value of temperature change you desire. Note that to the macrofield stress tensor is related to the reference frame of TESA Toolbox ("1" is to the right; "2" is to the top).

Figure A22. Macrofield options for stress/strain analysis.

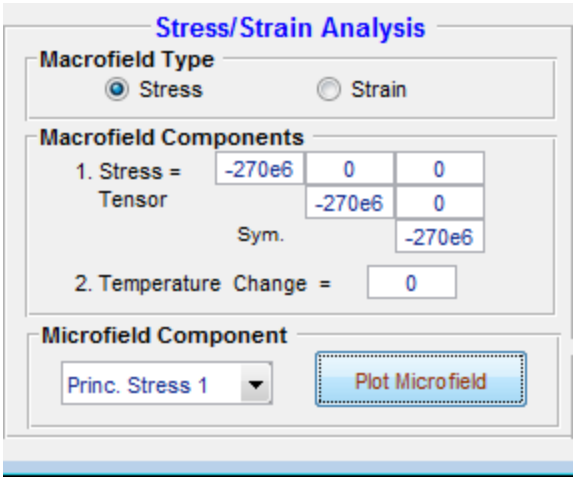

You can plot 23 components (Stress 11 ~ Volumetric Strain) in TESA Toolbox. Select an item you want to plot in “Microfield Components” and then “Plot Microfield” (Fig. A23).

Figure A23. Microfield components. Here, ‘Princ. Stress 1’ (maximum principal stress) is selected.

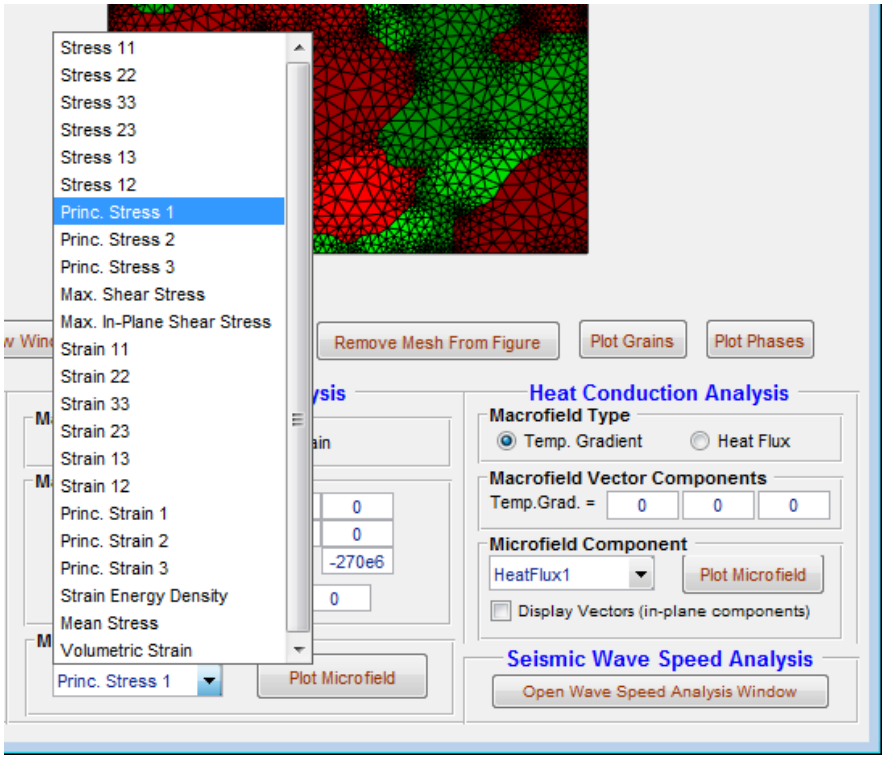

After clicking “Plot Microfield”, the following progress bars will be displayed (Fig. A24).

Figure A24. Progress bars related to stress/strain analysis.

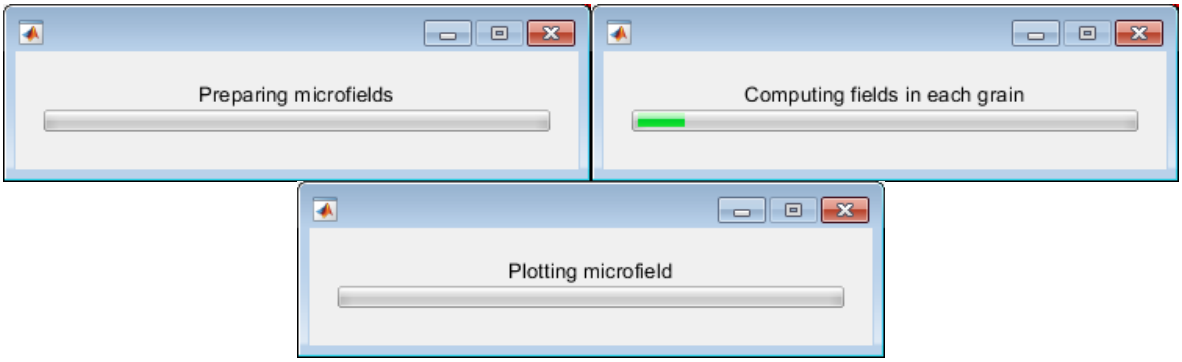

Now, the toolbox will be shown as below (Fig. A25).

Figure A25. TESA Toolbox after plotting microfield. In the plot, the min and max values (here in pascals) below the resulting plot are from the min and max values of the interpolated fields at the nodal points (interpolated from the quadrature point values). The quadrature points (four points) are located within each element.

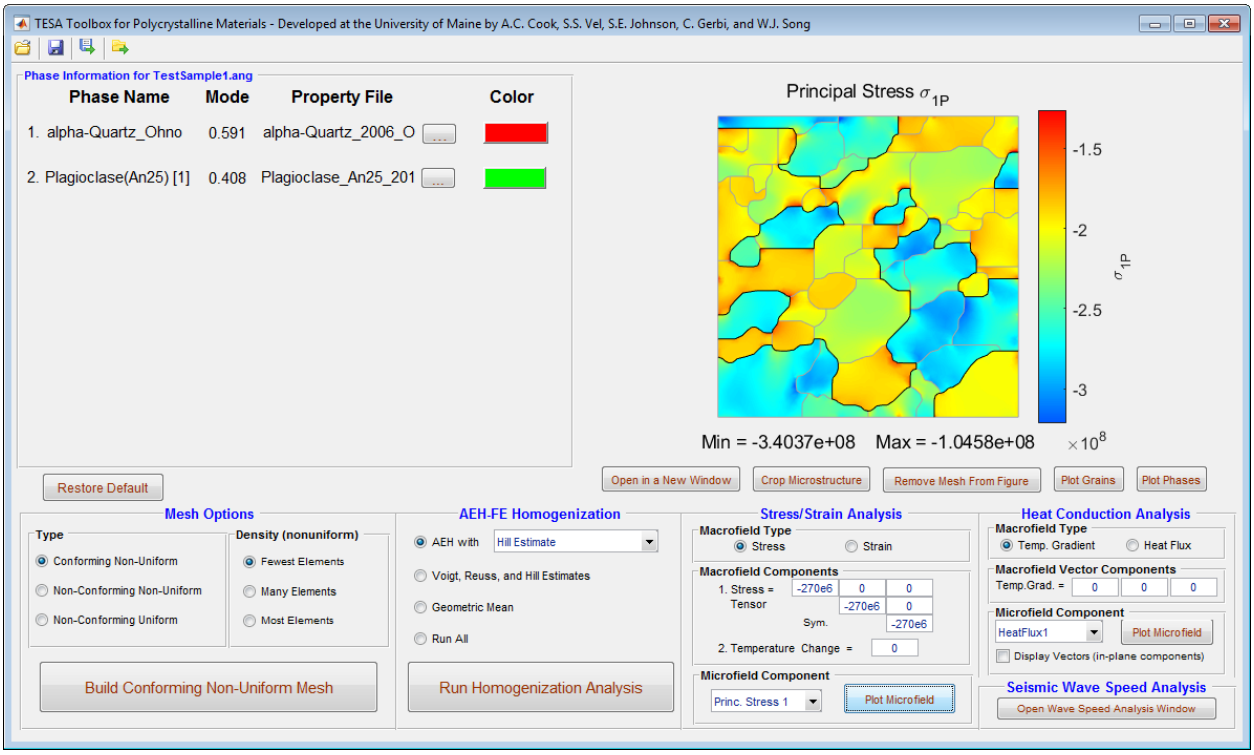

To save the current plot, “Open in a New Window” (Fig. A26). And then save the plot as MATLAB figure (.fig) for later modification in MATLAB. You can also export it as bitmap formats.

Figure A26. Opening in a new window to save the current plot.

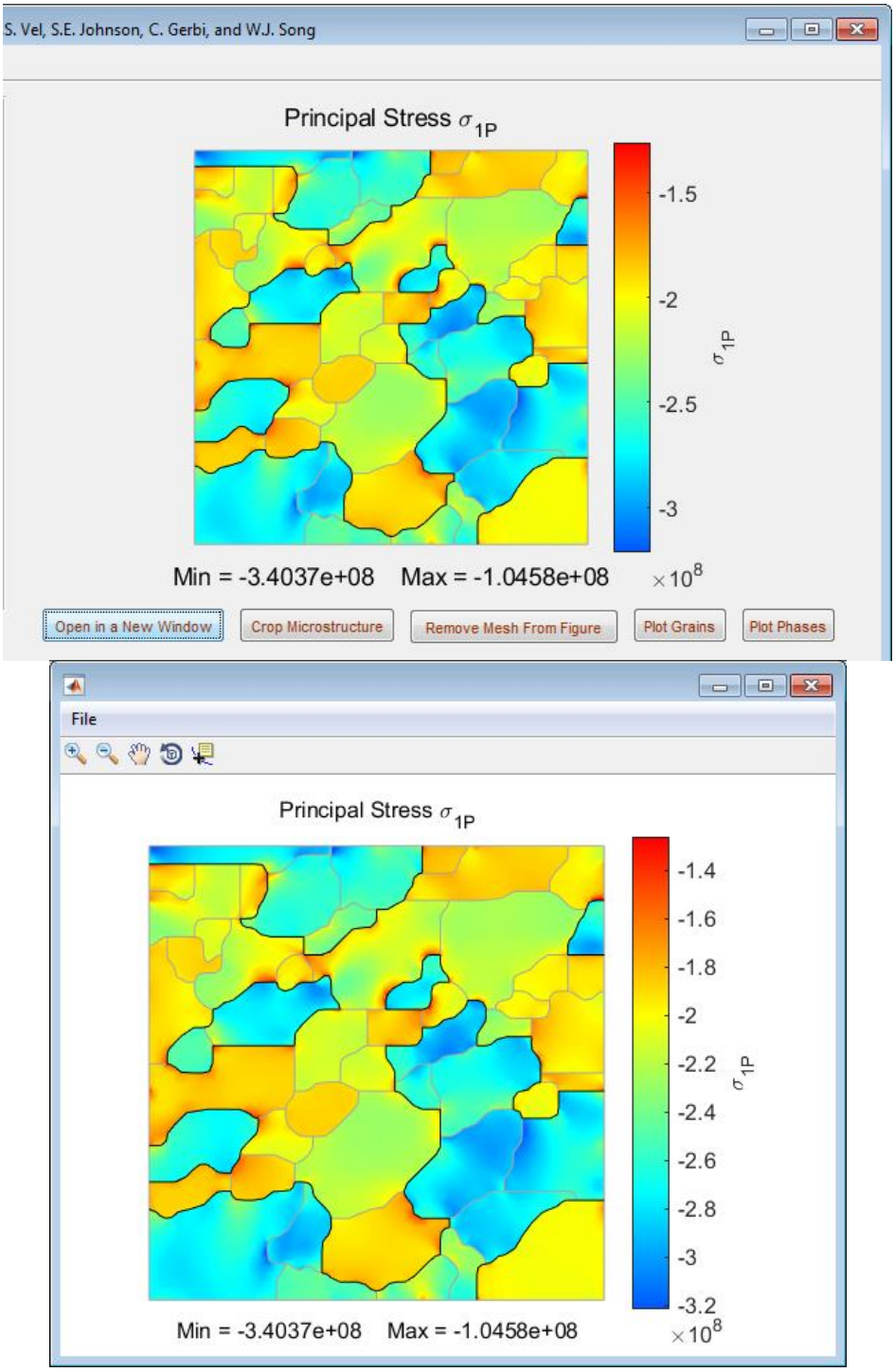

You can also plot meshed grains by clicking “Plot Grains”, which can be saved after “Open in a New Window” (Fig. A27). But, note that you cannot go back to the microfield plot (for this, you need to “Plot Microfield” again; thus make sure to save the microfield plot after microfield analysis).

Figure A27. TESA Toolbox after plotting grains.

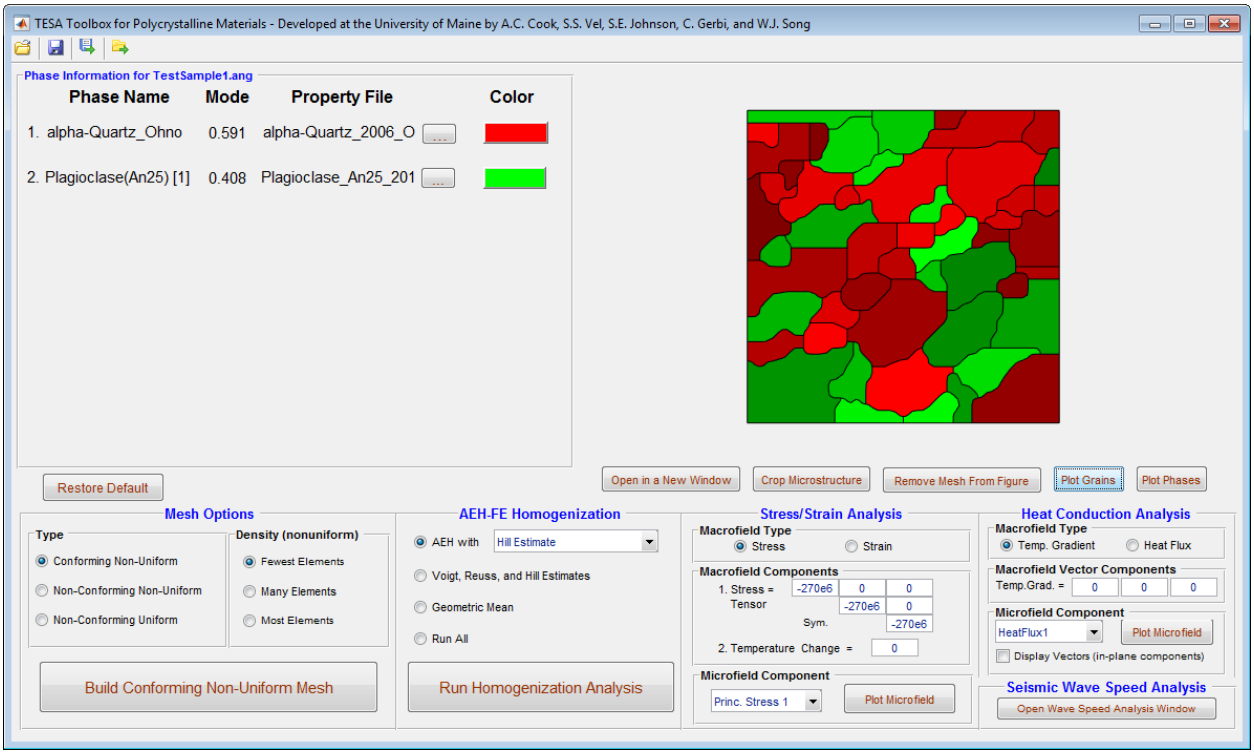

After you finish Stress/Strain Analysis, “Save Current Analysis” for future additional analyses by clicking the second icon from left in TESA Toolbox (Fig. A28). When saving, add the information of the “Macrofield Components” to file name. For example, “TestSample1_T=Zero-270MPaHydro.mat” (Fig. A29).

Figure A28. Save icon (the second from left) in the top left corner of TESA Toolbox.

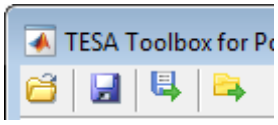

Figure A29. An example of file name when saving the final analysis file.

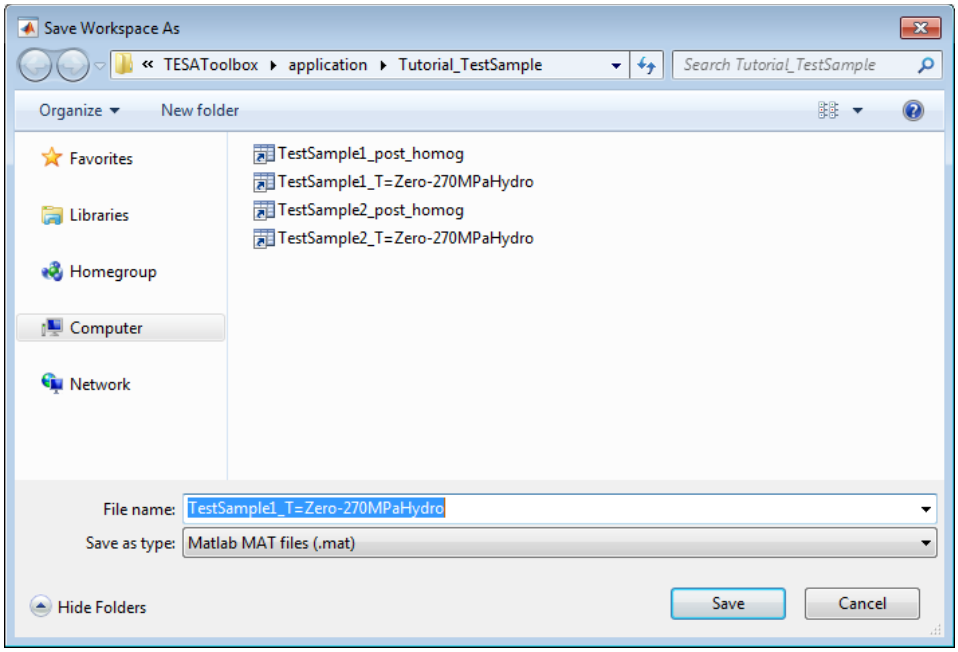

BIOGRAPHY OF THE AUTHOR

Won Joon Song was born in Hamyang, South Korea. He was raised in Jinju, South Korea and graduated from Jinju Dongmyung High School. He attended the Korea University, Seoul, South Korea, and graduated in 2004 with a Bachelor's degree in Earth and Environmental Sciences. He entered the Geology graduate program at the Korea University in 2005 and received a Master of Science degree in 2008. Won Joon Song is a candidate for the Doctor of Philosophy degree in Earth and Climate Sciences from the University of Maine in August 2018.